Title
Multifunctional mesoporous silica nanoparticles for drug and large molecule delivery

Author
Wang, Ruining

Publication Date
2020

Peer reviewed|Thesis/dissertation

UNIVERSITY OF CALIFORNIA

Los Angeles

Multifunctional mesoporous silica nanoparticles for drug and large molecule delivery

A dissertation submitted in partial satisfaction of

the requirement for the degree Doctor of

Philosophy in Materials Science and Engineering

by

Ruining Wang

2020

ABSTRACT OF THE DISSERTATION

Multifunctional mesoporous silica nanoparticles for drug and large molecule delivery

by

Ruining Wang

Doctor of Philosophy in Materials Science and Engineering

University of California, Los Angeles, 2020

Professor Bruce Dunn, Chair

This thesis involves synthesis, derivatization and biomedical applications of mesoporous silica nanoparticles (MSNs) based delivery systems. Chapter 1 introduces the background of MSNs including the advantages of MSNs, modification on MSNs for multifunctionality; formation mechanism, a typical synthesis condition for MCM-41 and following characterizaitons. In chapter 2 & 3, the synthesis and application of target moiety functionalized MSNs for gene therapy *in vitro* and *in vivo* are introduced. Chapters 4, & 5 introduce the relevant studies of utilizing MSN based delivery system for the treatment of infectious disease, from a pharmacokinetic study of moxifloxacin delivered by MSNs via different routes, to the enhanced efficacy of

MSN based treatment by materials optimizations via inhalation administration route. Chapter 6 discusses the study of a general synthesis method for pore enlargement in various types of MSNs. In Chapter 7, the design and preparation of a thin film consist of ultra large pore-sized mesoporous silica spheres and polymer template macropores is illustrated. Overall, these chapters demonstrate the successful engineering of mesoporous silica nanoparticles and materials optimization and their enhanced performance in biological applications from *in vivo* tumor shrinkage by gene delivery to antibiotics delivery for enhanced bacterial killing efficacy in mouse model.

The dissertation of Ruining Wang is approved.

Jeffrey I. Zink

Mark Goorsky

Bruce S. Dunn, Committee Chair

University of California, Los Angeles

2020

Table of Contents

ACKNOWLEDGEMENTS

It wouldn't be such an enjoyable though challenging journey for me to complete my doctoral degree if without the help from so many great individuals. I would like to express my sincere gratitude to those of you that helped me going through this import part of my life.

Firstly, I would like to deeply acknowledge my advisor, Professor Jeffrey I. Zink. I would like to thank him for offering me the opportunity to learn and study in a world-class lab at UCLA. He has mentored and prepared me with the scientific methodology and critical thinking ability to approach all kinds of difficulties, kindly guided me through various research projects that lead to fruitful results. In his group, I was very fortunate to collaborate with excellent researchers with various scientific backgrounds and be part of exciting projects. Professor Zink is a well-respected scholar who constantly shares his knowledge and vision through insightful discussions, but moreover he is such a considerate mentor who cares about the future of his students. I am so grateful to have him as my Ph.D. advisor. I would also like to thank Professor Bruce S. Dunn for being my advisor in the department of Materials Science and Engineering. I want to thank Professor Dwight Streit and Professor Mark Goorsky for serving on my dissertation committee. Their advice and suggestions have benefited me enormously.

Next I would like to thank my colleagues and friends in the Zink group. I would like to acknowledge Dr. Zilu Li and Dr. Angela Hwang for their great help from when I first joined the group and ever since then. Thanks to Dr. Bastian Ruehle, Dr. Philippe Saint-Cricq for your knowledgeable guidance, thanks to Dr. Wen-Yen Huang for those memorable

discussions and inspiring ideas, to Professor Liping Ruan for guiding me with your organic synthesis expertise. I would also like to express my great gratitude to my fellow colleges and friends in our group, Dr. Wei Chen, Dr. ChiAn (Annie) Cheng, Dr. Sheba Plamthottam, Dr. Chia-Jung Yu, Dr. Jonas Croissant, Dr. Jonathan Brosmer, Dr. Navnita Kumar, Dr. Yao Cai, Dr. Zhao Li, Fang-Chu Lin, Tian Deng, Jaime Fidel Ruiz-Robles. It has been a great pleasure and enjoyable time working with you all.

I would like to acknowledge my collaborators, without whom, a great portion of my research projects would not be as meaningful as they are now. I want to thank Dr. Glackin and her research group in City of Hope. It is the passion that I saw from her to bring healing to those who suffered cancer strongly inspired me. I would also like to thank Dr. Shahin from the Glackin group for her great contribution in the siRNA delivery project. I want to thank Professor Marcus Horwitz, and Dr. Daniel Clemens, Dr. Bai-Yu Lee and Dr. Michael V. Tullius in his group for the tremendous amount of help and insightful advice. I always enjoyed the group seminars and insightful discussions and I have learned so much from them on the infectious disease and biomedical areas. I would like to thank Professor Kent Pinkerton from UC Davis and his student Ariel Parker for collaborating on the silica inhalation projects. I want to thank Dr. Hessel for offering me the opportunity to work on the silica based gas sorbent project. I would also like to thank Dr. Chong Hyun Chang, and Professor Andre Nel for their help on sharing essential research instruments and the kindly guidance.

I would like to thank my friends outside the labs. I want to thank Chao Li, Zhongbo Yan, Pei Zhang and Chezheng Cao for being such great classmates and dear friends. I would like to thank Enbo Zhu, Rigen Mu, Yunfan Gu, Yue Zhao for all the happiness and joy

that we shared. A great thank you to Siyuan Wang, for being there with me through the ups and downs. The list just won't stop here, and your friendships would always be a great treasure and unforgettable memory for me.

Last but not least, I would like to thank my parents for being supportive to me all the time. It's really a blessing for me to having you and I could not express enough of my love to them.

VITA

2008-2012	B.S. Materials Science and Engineering
	Beihang University
	Beijing, China
2015-2018	Teaching Assistant
	Department of Chemistry and Biochemistry
	University of California, Los Angeles
2016-2019	Graduate Student Researcher
	Zink Lab
	University of California, Los Angeles

Chapter 1

Introduction to mesoporous silica nanoparticles for multifunctional delivery applications

1.1 Introduction

Background

Since the successful synthesis of MCM-41 family in 1992[1], mesoporous silica nanoparticles (MSN) have been intensively studied. Various unique features of them include, like large surface area, ordered and accessible pore channels, structural stability and relatively biocompatibility and facile surface functionalization.[2,3] With the help of those properties, MSNs have shown great potential in biomedical applications, particularly serving as carriers for the delivery of small molecule drugs, macromolecular therapeutics and/or even DNA/RNA for gene therapy.[4,5] The extra protection and potential multi-functionality of the MSNs offer much improved feasibility of new drugs for the treatment of diseases like viral infection and cancer. In addition, with certain surface modification or the use of well-designed nanovalves for pore blocking, the release of the cargo molecule can be controlled; navigation of the carrier to specific target cells/organisms is realized; longer circulation time in body but a suppressed toxicity and side effect of the therapeutic agents is also anticipated.[6,7]

Additionally, the incorporation of other inorganic components could bring MSNs with various functionalities. Core-shell geometry is often applied, where the inorganic nanoparticle core offers extra properties, and silica mesoporous shell provides the aforementioned advantages as cargo carrier. For example, CdSe/ZnS, CdTe/CdS quantum dot systems have been demonstrated as promising core components for *in vivo* fluorescent bio-imaging.[8,9] Au nanoparticles could also be utilized for their well-known

plasmon resonance effect. Light that a suitable wavelength is illuminated on the AuNP@MSN composite to induce internal heating, which opens up the thermal sensitive nanovalve and release of cargo molecules.[10] However, penetration depth of light into body becomes a severe issue for the development of light-triggered release system. Wavelength in the infrared region is considered favorable for its long penetration distance, yet the energy of which is often not enough to activate the nanovalve to release drugs. Oscillating magnetic field, on the other hand, will not suffer from the penetration problem, thus can be utilized as a non-invasive external stimulus. Magnetic nanocrystals within the oscillating field will generate heat for the operation of thermal sensitive nanovalves. Moreover, magnetic iron oxide nanocrystals would potentially be utilized to navigate the carrier for targeting purpose, or serve as MRI agent for imaging.[11]

Another way of introducing multifunctionality into the MSNs based delivery systems is to modify either the inner pore surface or outer surface by electrostatic force or chemical conjugation of various types of functional moieties. For example, poly ethylene glycol (PEG) is often coated on the surface of MSNs to enhance the circulation time of particles in body.[12] The surface charge property can be varied by certain modification to enhance loading efficiency or stabilize particles in solvent. For example, functional groups like amine and phosphonate can be attached on either inner or outer surface of the MSNs by co-condensation of (3-Aminopropyl) triethoxysilane (APTES)/ 3-trihydroxysilylpropylmethylphosphonate (HTMP) during the reaction, or by post grafting those small molecules with MSNs reflux in toluene. Surface modification can be performed without the extraction of surfactant so that only outer surface is modified. By using nanovalve to block the pore openings, the release of drugs can be realized in a

controllable fashion. As illustrated in Figure 1.1., scheme in graph (A) shows the process of utilizing the surface silanol group (Si-OH) and silanol chemistry to put on functional groups, and shown in graph (B) are some examples of commonly used silanes with functional groups or stalks with nano valves on them.

Mesoporous Silica Nanoparticles and formation mechanisms

Nano-sized mesoporous silica was first synthesized and reported by the groups of Cai[13] and Ostafin[14]. Since then, MSNs with various morphologies, dimensions, pore sizes and pore structures have been synthesized and investigated systematically.[15] The mechanism of the basic synthesis strategy applied can be briefly illustrated in Figure 1.2. To generally describe the formation process:[16,17] (I) Cetyltrimethylammonium bromide (CTAB) is used as the surfactant, which form micelle in aqueous solution. Positively charged hydrophilic head groups are facing outward, while the long hydrophobic alkyl chains tangle inward away from the aqueous environment. The shape of the micelle can be semi-quantitatively described by the packing parameter $P= V_0/ (a_e X l_0)$. In this equation, V_0 is the surfactant tail volume, a_e is the equilibrium area per molecule at the aggregate interface and l_0 is the tail length (shown in Figure 1.2.). Those values are all effective size in water, thus they will be affected by each other, and synthesis conditions like temperature, viscosity of the solution and concentration of surfactant. When the concentration of surfactant exceeds the critical micelle concentration (CMC), surfactants quickly assemble into micelle in a cooperative way to reduce the Gibbs free energy of the system. (II) Ordered inorganic-organic hexagonal structure formed upon addition of silica source tetraethyl orthosilicate (TEOS). This was proved by small angle X-ray scattering (SAXS).[18] (SAXS enables the study of particle correlations at the mesoscopic scale,

where an abrupt change of electron density occurs at the interface between the silica network and the void pore space.) The hydrolysis and condensation of TEOS in the presence of base catalyst happens along with the self-assembling of micelles into nanoparticles.

$$\text{Hydrolysis: } OH^- + Si(OR)_4 \rightarrow Si(OR)_3OH + RO^-$$

$$\text{Condensation: } SiO^- + Si(OH)_4 \rightarrow Si{-}O{-}Si + OH^-$$

(III) Finally, the surfactant can be removed by ion exchange with acid or calcination.

Besides the commonly implied hexagonal packing of micelles in the case of MCM-41, other mesophase structures have been revealed with the help of SAXS technique. Firouzi et al.[16] came up with a phase diagram of silica mesophases as illustrated in Figure.1.2. In their work, the ordered stacking of micelles was investigated for synthesis with different ratios between surfactant, silica source and base catalyst. As a result, different stacked structures (hexagonal, cubic and lamellar) were observed. Later on, Monnier[17] and Stuky[18] raised the mechanism of “charge density matching”, where a lamellar phase was first formed in the solution. Then, as the negatively charged silicate began to condense, the positive charge density reduced, and they began to wrap around the surfactant, forming hexagonal mesostructure. This process indicated the reaction would be heavily influenced by the pH of the solution together with the condensation rate of the silicate.

As mentioned above, MSNs with various morphologies and pore structures can be obtained by the adjustment of the synthesis conditions, including types of base, the pH of the solution, the molar ratio between the reactants as well as Temperature, viscosity and other parameters of the system.

A typical synthesis route of MCM-41 and following characterizations

A typical lab protocol for the synthesis of MCM-41 and following characterizations is introduced in this section. 50mg cetyltrimethylammonium bromide (CTAB, Aldrich, 95%) was dissolved in 25 mL water with 150 μL NaOH (2.0 M), the solution of which was heated to 80°C under rapid stirring. After 30 minutes at this temperature, 270 μL tetraethylorthosilicate (TEOS, Aldrich, 98%) was added dropwisely. The solution slowly turned to transparent blue, indicating the nucleation and growth of silica nanoparticles. Reaction was kept at 80°C for 2 hours, then the solution was cooled down to room temperature, and the nanoparticles were collected by centrifugation at 7800 rpm. The pellet from centrifugation was redispersed and washed with ethanol for three times, and dispersed in ethanol for further use.

Approximately 50mg of MCM-41 can be collected from this synthesis, which gives a yield of 62% wt. After synthesis, surfactant (CTAB) can be removed by acid extraction or calcination at over 500°C. However, calcination may introduce aggregation of nanoparticles, thus extraction with HCl or NH_4NO_3 was applied in this work. The nanoparticles were redispersed in ethanol with the presence of acid and refluxed for 6-12 hours. Ion exchange occurred between the protons in solution with the positively charged CTA^+, thus extrapolating the surfactant leaving behind mesoporous silica nanoparticles. The amount of acid used here was overdosed to ensure a complete removal of the CTAB for its cytotoxicity. The disappearance of the C-H peaks in IR around 2900 cm^{-1} indicated the removal of CTAB surfactant, as illustrated in Figure 1.3.

The overall and magnified TEM images for the morphology of the nanoparticles are shown in Figure 1.4. An average particle size around 120 nm was observed from the low-magnification image. The 2D hexagonal packing of the mesostructure can be clearly seen

in the zoom-in picture. The inter-particle bridging effect was attributed to a fast condensation rate of the silica, and can be characterized by dynamic light scattering (DLS) shown in Table 1.1. When light is scattered by the particle in certain solvent, a distribution of the particle hydrodynamic diameter can be revealed. Typically, a low concentration of particle suspension was used (~100 ug/mL) to reduce particle collision electrostatic interactions in the solvent. Ideally, the hydrodynamic diameter of the nanoparticles should be less than 100-200 nm, otherwise they would be quickly repelled from the circulation system.[7] This synthesis method was considered as a typical synthesis route for the preparation of MCM-41 nanoparticles before further modification in the later chapters. Other characterization methods besides TEM, FTIR, DLS on the MSNs could be zeta potential measurement, nitrogen gas adsorption/ desorption, thermogravimetric analysis, etc.

1.2 Tables and figures

Run	Effective Diameter (nm)	Polydispersity
1	121.4	0.144
2	113.9	0.133
3	118.5	0.152

Table 1.1 DLS measurement results

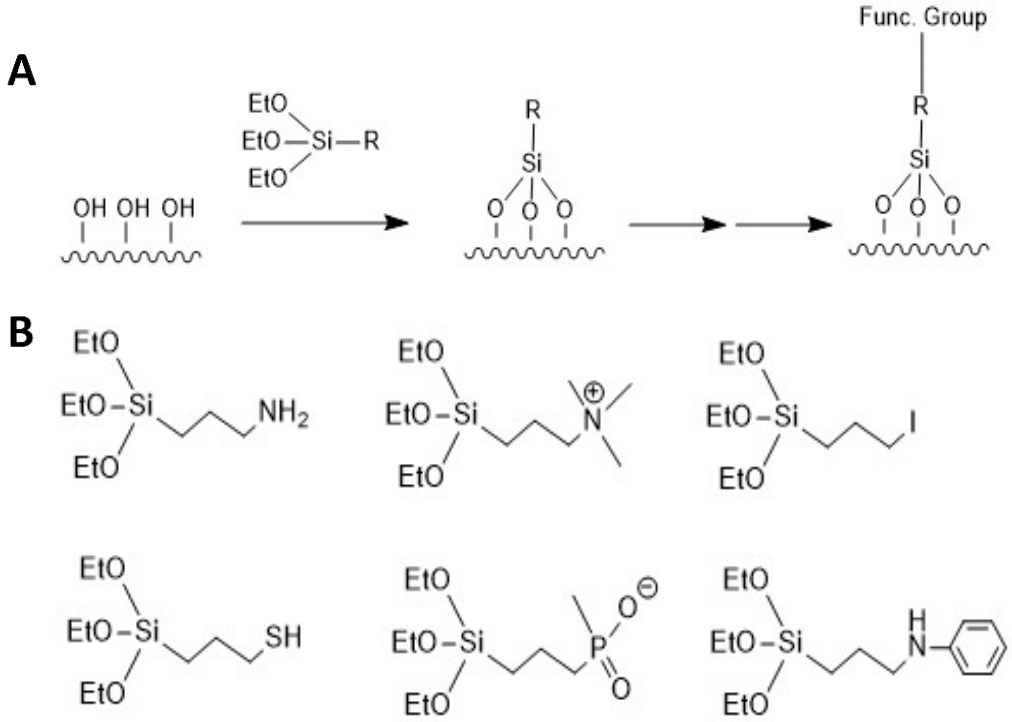

Figure 1.1. Scheme of surface modification on MSNs. (A) Process of surface chemistry on silica silanol groups. (B) Commonly used silanes with functional groups.

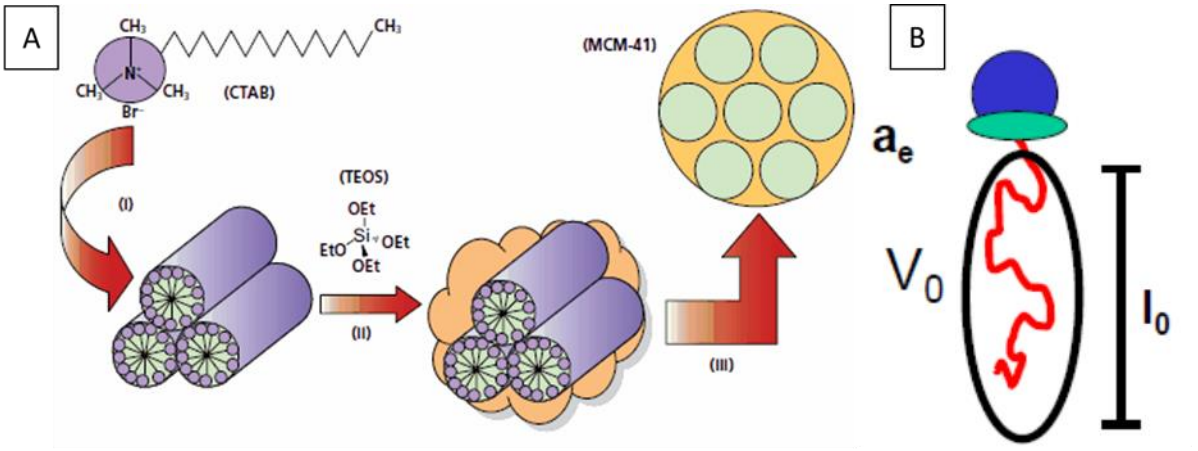

Figure 1.2. Schematic of (A) the classical mesoporous silica (MCM-41) synthesis route, (B) A typical scheme of surfactant.[15]

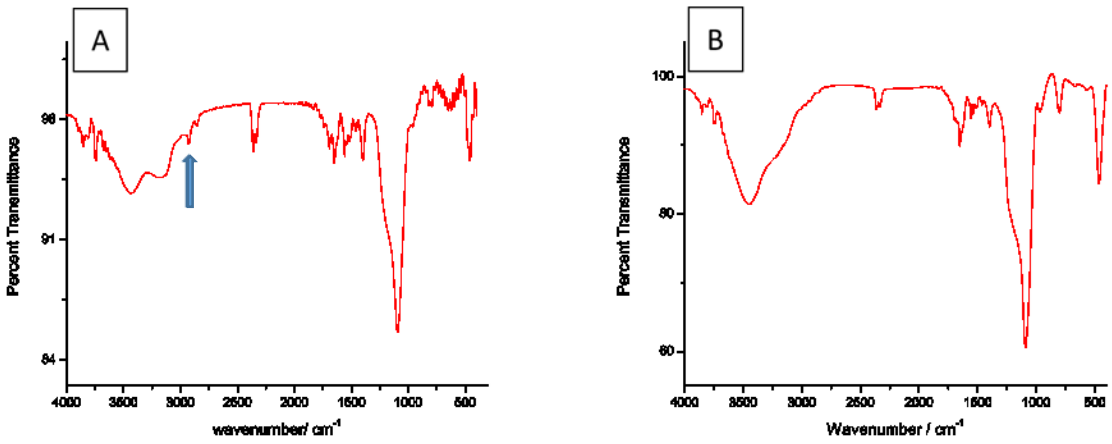

Figure 1.3. FTIR of MSNs before (A) and after (B) surfactant removal

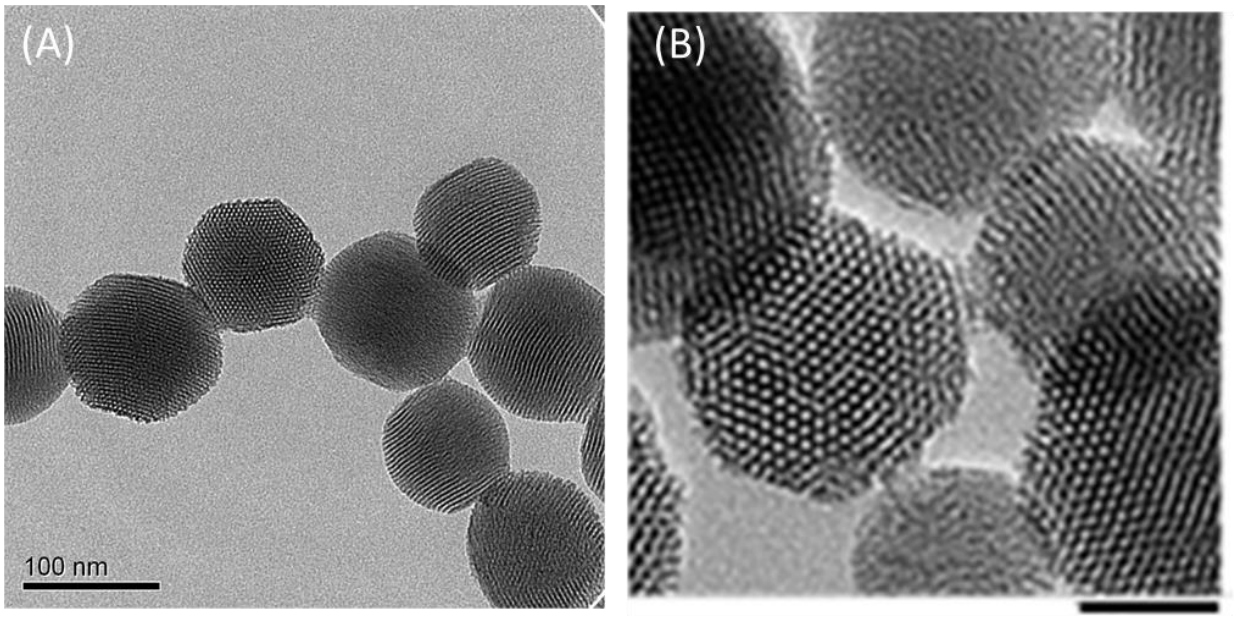

Figure 1.4. TEM images of MCM-41. Scale bar in the left image (A) is 100 nm, scale bar in the right image (B) is 40 nm.

1.3 References

1. Kresge, C. T., Leonowicz, M. E., Roth, W. J., Vartuli, J. C. & Beck, J. S. Ordered mesoporous molecular sieves synthesized by a liquid-crystal template mechanism. *Nature* **359**, 710–712 (1992).
2. Li, Z., Barnes, J. C., Bosoy, A., Stoddart, J. F. & Zink, J. I. Mesoporous silica nanoparticles in biomedical applications. *Chem. Soc. Rev.* **41**, 2590–2605 (2012).
3. Kumar, N. *et al.* Chapter Three - Stimuli-Responsive Nanomachines and Caps for Drug Delivery. in *Mesoporous Silica-based Nanomaterials and Biomedical Applications, Part A* (ed. Tamanoi, F. B. T.-T. E.) vol. 43 31–65 (Academic Press, 2018).
4. Dorsett, Y. & Tuschl, T. siRNAs: applications in functional genomics and potential as therapeutics. *Nat. Rev. Drug Discov.* **3**, 318–329 (2004).
5. Chen, A. M. *et al.* Co-delivery of Doxorubicin and Bcl-2 siRNA by mesoporous silica nanoparticles enhances the efficacy of chemotherapy in multidrug-resistant cancer cells. *Small* **5**, 2673–2677 (2009).
6. Cheng, C.-A., Deng, T., Lin, F.-C., Cai, Y. & Zink, J. I. Supramolecular nanomachines as stimuli-responsive gatekeepers on mesoporous silica nanoparticles for antibiotic and cancer drug delivery. *Theranostics* **9**, 3341 (2019).
7. Sarker, D. K. *Pharmaceutical emulsions: a drug developer's toolbag*. (John Wiley & Sons, 2013).
8. He, X., Wang, K. & Cheng, Z. *In vivo* near-infrared fluorescence imaging of cancer with nanoparticle-based probes. *Wiley Interdiscip. Rev. Nanomedicine*

Nanobiotechnology **2**, 349–366 (2010).

9. Gaponik, N. & Rogach, A. L. Thiol-capped CdTe nanocrystals: Progress and perspectives of the related research fields. *Phys. Chem. Chem. Phys.* **12**, 8685–8693 (2010).
10. Bansal, A. & Zhang, Y. Photocontrolled Nanoparticle Delivery Systems for Biomedical Applications. *Acc. Chem. Res.* **47**, 3052–3060 (2014).
11. Veiseh, O., Gunn, J. W. & Zhang, M. Design and fabrication of magnetic nanoparticles for targeted drug delivery and imaging. *Adv. Drug Deliv. Rev.* **62**, 284–304 (2010).
12. Xia, T. *et al.* Polyethyleneimine Coating Enhances the Cellular Uptake of Mesoporous Silica Nanoparticles and Allows Safe Delivery of siRNA and DNA Constructs. *ACS Nano* **3**, 3273–3286 (2009).
13. Cai, Q. *et al.* Dilute Solution Routes to Various Controllable Morphologies of MCM-41 Silica with a Basic Medium. *Chem. Mater.* **13**, 258–263 (2001).
14. Nooney, R. I., Thirunavukkarasu, D., Chen, Y., Josephs, R. & Ostafin, A. E. Synthesis of Nanoscale Mesoporous Silica Spheres with Controlled Particle Size. *Chem. Mater.* **14**, 4721–4728 (2002).
15. Fierke, B. M. A. *et al.* From Form to Function : Molding Porous Materials in Three Dimensions by Colloidal Crystal Templating Preparing the Colloidal Crystal Template. 2–5 (2008).
16. Firouzi, A. *et al.* Cooperative organization of inorganic-surfactant and biomimetic assemblies. *Science (80-.).* **267**, 1138 LP – 1143 (1995).
17. Monnier, A. *et al.* Cooperative Formation of Inorganic-Organic Interfaces in the

Synthesis of Silicate Mesostructures. *Science (80-.).* **261**, 1299 LP – 1303 (1993).

18. Stucky, G. D. *et al.* Molecular and Atomic Arrays in Nano- and Mesoporous Materials Synthesis. *Mol. Cryst. Liq. Cryst. Sci. Technol. Sect. A. Mol. Cryst. Liq. Cryst.* **240**, 187–200 (1994).

Chapter 2

Mesoporous silica nanoparticles as vehicles for delivering siRNA to ovarian cancer cells

This chapter is based on work done with collaborators Sophia A. Shahin, et. al. at Beckman Research Institute, City of Hope for biological assays and mouse model tests. A manuscript is prepared for submission and review.

2.1 Abstract

In this chapter, a novel type of mesoporous silica nanoparticles based gene delivery system is described. Hyaluronic acid was chosen as a targeting moiety and was chemically conjugated to the MSNs. By targeting the overexpressed CD-44 on targeted cell lines, the transfection efficiency of PEI@MSNs was greatly enhanced for the delivery of siTWIST and subsequent gene therapy. Combined with bioassays, confocal microscopy and flow cytometry, an optimized ratio between the HA moiety and the PEI layer on the MSNs was determined. Physicochemical properties of the as prepared HA-PEI@MSNs were investigated by TEM, DLS, Zeta potential, TGA, FTIR and N_2 adsorption/desorption. Moreover, this novel nanoparticle delivery system was proved effective in a preliminary mice model study for sensitizing multidrug resistance tumor model when combined with chemotherapy.

2.2 Introduction

The downregulation of gene expression using small interfering RNA (siRNA) has become a promising strategy for cancer therapy and related medical applications.[1–3] However, the delivery of siRNA for clinical use remains challenging. For instance, siRNAs are rapidly degraded by nucleases in biological fluids and will not cross cell membrane by itself, let alone selectivity to targeted tissues.[4] Various types of gene vectors have been extensively studied over the last decade that can be divided into two general categories of viral vectors and non-viral vectors.[5–9] Viral vectors are known for their high transfection efficiency for the delivery of nucleic acid into targeted host cells,[5,7] yet the clinical

application is limited due to the strong immunogenicity and other potential adverse effects. Therefore, various of non-viral vectors for gene delivery are proposed, including lipids[10], polymer complex[6,11], and inorganic nanoparticles[12–14]. Each of those non-viral transfection agents had its own advantages and limitations. In general, the overall goal of an optimized transfection agent is to achieve high transfection efficiency *in vivo* to specific cells and tissues of interest, therefore diminishing unfavorable side effects on off-target healthy tissues.[15]

Positively charged polymer polyethylenimine (PEI) and its various derivatives and formed nanoparticles are heavily studied and utilized in the last decade for the delivery of negatively charged genes.[16–18] Polyethylenimine, either in its linear form or branched form, is complexed directly with the gene of interest or is complexed with other functional chemical group or copolymer, forming uniform sized nanoparticles of 50 nm to 200 nm in physiological conditions as delivery vehicles.[17] Generally speaking, the transfection efficiency increases with higher molecular weight of the PEI used in the system, yet the cytotoxicity increases as higher positive charge density of the delivery system would permeabilize cellular or nuclear membranes or bind cytoplasmic proteins.[19] Moreover, the presence of free PEI residue would introduce additional cytotoxicity, yet some study has shown the necessity of free PEI in the polyethylenimine delivery system to obtain high transfection efficiency.[20] On the other hand, mesoporous silica nanoparticles (MSNs) have been widely investigated as delivery vehicles with large surface area for drug molecules accommodation.[21] MSNs are utilized in several cases for gene delivery because of their excellent biocompatibility and further chemical modification with ease for multifunctionality incorporation.[22–24] Previously, we have reported a hybrid materials

based delivery system, combining inorganic MSNs and organic PEI polymer, for the delivery of a specific small interference RNA (siRNA) for gene therapy.[22] siTWIST, as the gene of interest for delivery, is responsible for down regulating the expression of TWIST1, leading to the suppression of epithelial–mesenchymal transition (EMT) process and multidrug resistance in ovarian cancer and ultimately reduce tumor burden and metastatic diseases.[25,26] We have demonstrated that with PEI coating on MSNs surface and siTWIST loaded within the PEI layer (siTWIST-PEI@MSNs), the siTWIST was successfully delivered and regulating the expression of siTWIST1 *in vitro* and *in vivo*. Combined with chemotherapy of cisplatin treatment in a sequential manner, tumor burden was effectively reduced in a mice model.[27]

With the idea of further enhance the transfection efficiency of this PEI@MSNs delivery system, we combined a well-known targeting moiety of glycosaminoglycan, hyaluronic acid (HA), via chemical conjugation to the PEI layer. The HA moiety will target the cluster of differentiation 44 (CD44) that is overexpressed in cancer stem cells (CSC) and various ovarian types of cancer cells, which would facilitate the uptake of the proposed delivery system and potentially suppress the metastasis development.[28–32] We engineered and optimized this novel type of delivery vehicle by fine tuning the composition and ratio of targeting HA moiety and PEI layer component. The different compositions of nanoparticles were subjected to confocal microscopy, western blot analysis and Sulphorhodamine B Cell Survival Assays, finding the ideal ratio with the optimal transfection efficiency *in vitro*. Based on these results, we finally estimated the siTWIST knockdown efficiency of both metastatic and chemoresistant phenotype in a highly metastatic ovarian cancer model *in vivo*.

2.3 Experimental

Materials

Cetyltrimethylammonium bromide (CTAB, 95%), tetraorthoethyl-silicate (TEOS, 98%), 3-(trihydro-xysilyl)propyl methylphosphonate (HTMP, 42% in H_2O), (3-Aminopropyl)triethoxysilane (APTES, 99%), N-hydroxysulfosuccinimidesodium salt (sulfo-NHS, 98%), MES monohydrate (MES-Buffer, 99%), Hyaluronic acid sodium salt from Streptococcus equi (HA, 1.5-1.8 × 10E6 Da) and toluene (99.8%) were purchased from Sigma. polyethylenimine, branched, M.W. 1,800 (PEI) (99%) was purchased from Alfa Aesar. DyLight™ 680 NHS-Ester was purchased from Thermo Fischer.

Synthesis of PEI@MSNs

Polyethylenimine (PEI) coated MSNs were prepared according to a previously reported method.[19] In brief, cetyltrimethylammonium bromide (CTAB, 0.7 mmol) were mixed with NaOH (2M, 1.7 mmol) in deionized water (120 mL). The solution was kept at 80 °C for an hour when tetraethylorthosilicate (TEOS, 5.4 mmol) was added dropwisely. After 30 minutes, 3-(trihydroxysilyl) propyl methylphosphonate (HTMP, 0.5 mmol) was added to the mixture dropwisely. The reaction temperature was maintained at 80 °C for 2 hours after which the solution was cooled to room temperature and the as synthesized MSNs were collected by centrifugation and washed thrice with water and ethanol. CTAB was removed from the MSNs by suspending the MSNs (200 mg) in ethanol (80 mL) with the addition of concentrated HCl (10 mL) and reflux for 1 hour twice. The particles were washed with ethanol after each extraction step and finally dispersed in ethanol for further

surface coating. Finally, low molecular weight branched PEI (1.8K) was electrostatically attached to the MSNs by mixing MSNs (10 mg) with PEI ethanol solution (2.5 mg in 1mL) by a rotating mixer twice. The as-prepared particles (denoted as PEI@MSNs) were then washed several times with ethanol/ DI water to remove un-bonded PEI, dispersed in 1X PBS for further modification.

Fluorescently labeled MSNs were prepared by, first mixing (3-aminopropyl) triethoxysilane (APTES, 0.2 mmol) with TEOS (4.5 mmol) then dropwisely adding in the sol-gel reaction. After the removal of CTAB, re-disperse MSNs in DMF, then added in DyLight 680 NHS-Ester (500 µL) that reacted with the amine groups mainly at the inner pores. After dye labeling, the particles were washed and processed as described previously for PEI coating.

Hyaluronic acid attachment

Hyaluronic acid (HA) was covalently conjugated to the amine groups in the PEI layer. In a typical experiment, hyaluronic acid (HA, 10 mg) were first dissolved in MES buffer (5 mL) and stirred overnight to ensure hydration of the carboxylate group. Later, 10 mg EDC and 5 mg NHS were added to the HA solution and stirred for 2 hours at room temperature to activate the carboxylate group in the HA. In the meantime, the PEI@MSNs (50 mg) were dispersed in 10 mL fresh 0.1X PBS under vigorous stirring. After EDC-NHS activation, 3.5 mg equivalent amount of HA in MES solution was slowly added into the PEI@MSNs suspension and stirred for another 8 hours. The as-synthesized particles were collected by centrifugation and washed thoroughly with DI water and finally stored in 1X PBS for siRNA binding.

Characterization of MSNs

The morphology of the as-synthesized MSNs, PEI@MSNs and HA-PEI@MSNs were analyzed with a T12 Quick CryoEM (FEI). The size and distribution and zeta potential of MSNs were measured by ZetaSizer Nano (Malvern Instruments Ltd., Worcestershire, U.K.) by suspending particles in DI water with a concentration of 50-100 μg/mL. Fourier transform infrared spectroscopy (FTIR) was operated by a JASCO FT/IR-420 spectrometer. Thermogravimetric analysis (TGA) was operated by a Perkin-Elmer Pyris Diamond TG/DTA under air at a speed of 200 $mLmin^{-1}$. Nitrogen adsorption-desorption isotherms were performed on an Autosorb-iQ (Quantachrome Instruments) with the temperature of 77 K. The pore size were calculated by a NLDFT model.

PEI@MSNs suspension and stirred for another 8 hours. The as-synthesized particles

Cell culture

F2 cell lines were grown in RPMI 1640 (10% fetal bovine serum and 1% penicillin/streptomycin) (Genesee Scientific) in a tissue culture incubator at 37°C, 5% CO2, and 90% humidity. Cells were passaged every 2-4 days using 0.25% trypsin (Genesee Scientific). Where indicated, cells were transfected with Lipofectamine 2000 (Thermo Fisher). F2 cells are cisplatin resistant cells taken from primary patient tissue with high grade serous ovarian cancer and were a gift from Dr. Gil Mor at Yale University.

Flow cytometry and Intracellular localization imaging by confocal microscopy

Flow cytometry was performed using a LSR (Bec- ton Dickinson, Mountain View, CA). F2 cells were seeded into a 3.5 cm glass bottom tissue culture dish. Following attachment

(24 hours), old medium was replaced with 2 mL fresh medium. Next, MSN-HA-siQ (labeled with AlexaFluor® 647) was added to the cells at final concentration of 17.5 ng/μL (MSN) and 5 nM (siQ) and incubated for an additional 48 hours. Cells were then labeled with mCherry (Thermo Fisher Scientific). Lysosomes was labeled with LysoTracker (Thermo Fisher Scientific). Confocal images were obtained using the Zeiss LSM700 Confocal Microscope (Zeiss AG).

Western blot analysis of twist expression

According to our previous reported procedure[33], following Lipofectamine 2000 or MSN-HA delivery of siRNA, cells were pelleted and lysed in RIPA buffer (50 mM Tris HCL, 1% NP-40, 0.1% SDS, 150 nM NaCl, 1 mM EDTA and 0.5% sodium deoxycholate). Protein concentration was determined by BCA assay (Thermo Fisher). Following SDS-PAGE, protein was transferred to Amersham PVDF membrane (Genesee Scientific) using a BioRad Trans-Blot SD semi-dry transfer unit. After washing, blots were then blocked in milk for one hour at room temperature or overnight at 4°C. Incubation with primary antibody took place for one hour at room temperature or overnight at 4°C, Antibodies were diluted in 5% milk, with 0.1-0.2% Tween-20. Antibodies used were TWIST 2c1a (Santa Cruz Biotechnology, Dallas, TX) at 1:250-1:500 dilutions, β-Actin, A1978 (Sigma Aldrich, St. Louis, MO) at 1:2500-1:5000 dilutions; and Horseradish Peroxidase (HRP) conjugated anti-mouse secondary antibodies. For westerns, the Syngene Pxi4 digital blot imager and Michigan Diagnostics FemtoGlow chemilumescent substrate were used.

SRB assay

According to our previous reported procedure[33], F2 cells were plated in 6 well plates and allowed to adhere overnight. The following day, cells were transfected with siQ, siTWIST using MSN-HAs. After 48-72 hours, cells were transferred to 96 well plates at 5,000 cells per well and allowed to adhere overnight. The following day cells were treated with cisplatin at a series of concentrations (cells not treated with cisplatin served as controls). After 72 hours, cells were fixed in 10% trichloroacetic acid for 1 hour at 4°C, washed with water, and dried. Cells were stained in 0.4% sulphorhodamine B (SRB) in 1% acetic acid for 15 minutes at room temperature and then washed 3-4 times with 1% acetic acid until no further color was present in the wash. Any stray SRB on the walls of the wells was removed, and stained cells were dried for 10 minutes. SRB was solubilized in 10 mM Tris base and color intensity was quantified by absorbance at 570 nm. Each condition was normalized to its own untreated control.

In vivo study

The animal studies conducted in these experiments were done in accordance with the protocol approved by the Institutional Animal Care and Use Committee at the City of Hope Beckman Research Institute. High quality humane care for all animal subjects was implemented for this study. A total of 20 female NOD.Cg-PrkdcscidIl2rgtm1Wjl/SzJ (NSG) mice (The Jackson Laboratory, Bar Harbor, ME) were used. Ten-week-old mice were administered an IP of 2.5 x 106 F2 mCherry labeled primary ovarian cancer cells in 200 µL of RPMI media. For all studies, mice were placed into six groups: control, untreated, MSN-HA-siQ, MSN-HA-siTWIST, CISPLATIN, and MSN-HA-siTWIST + cisplatin. Mice received 105 µL of 500 ng/µL MSN complexed with 15 µL of 10 µM siRNA per week, with one full dose (n=8 and n=4, respectively). This is equivalent to 2.5 mg MSN/week. Weekly

3 mg/kg IP cisplatin injections were given starting two weeks after initial inoculation of tumor cells to ensure all mice received same amount of chemotherapy. Lastly, animals were euthanized via CO_2 asphyxiation followed by necropsy.

Bioluminescent imaging of mice (using Xenogen IVIS 100 biophotonic imaging system, STTARR) commenced seven days after injection of tumor cells in order to ensure engraftment, and continued once a week for four weeks. Mice were given a 100 µL IP injection of 20 mg/mL D-Luciferin (PerkinElmer, Waltham, MA). Ten minutes after the D-luciferin injection, mice were anesthetized with isoflurane (2%-5%) and placed in the biophotonic imager, and images were taken within two minutes. An alfalfa-free version of the regular rodent diet (alfalfa-free CA-1) was administered to the siQ mice to prevent autofluorescence from the regular diet.

2.4 Result and discussion

Synthesis and characterization of HA-PEI@MSN

Polyethylenimine (PEI) coated on MSNs for the delivery of siRNA has been tested to efficiently knockdown Twist expression in breast cancer cell and ovarian cancer cell.[34] Herein, hyaluronic acid (HA) was chosen as a targeting agent for CD44 receptors that overexpressed on ovarian cancer cells. The amount of HA conjugated to MSNs was carefully investigated. In principle, as the carboxylate group from HA would be deprotonated in physiological conditions and possess negative charge, increasing amount of HA conjugated would potentially hinder the capability of PEI to absorb siRNA. Therefore, different amount of HA was employed to optimize the transfection efficiency.

The HA-PEI@MSN particles were synthesized as depicted in Figure 2.1. (A). Briefly, negatively charged phosphonate groups were modified to the outer surface of MSNs during the sol-gel synthesis process, which will serve as anchor to electrostatically absorb PEI polymer. After coating MSNs with PEI, the excess amine ($-NH_2$) in the PEI were utilized to react with carboxyl (-COOH) of hyaluronic acid through EDC-NHS coupling reaction to form amide bond (-CO-NH-). Different weight ratios between HA and PEI@MSN were tested for the synthesis, where the final products were denoted as HAx-PEI@MSN (x mg HA per 10 mg of MSNs). As shown from the TEM images in Figure. 2.1. (B), the morphology of the particles was not significantly changed after the coating of PEI or the attachment of HA, while the pore channels became less obvious with further surface modification, indicating the coating at mainly the outer surface as expected.

The sequential addition of PEI and HA polymer to the MSNs was monitored by zeta potential measurement. Phosphonate functionalized MSNs (MSN-phos) possessed a negative zeta potential of -35 mV. After PEI coating, the surface charge became positive in PBS buffer. (Figure 2.2. (A)) different amount of HA addition (from 0.1 mg to 1.0 mg per 10 mg PE@MSNs) would yield a serial change in zeta potential from +17 mV to -18 mV. The change in zeta potential indicated the successful attachment of PEI and HA polymer onto the MSNs. As expected, with increasing amount of HA used for the conjugation, the zeta potential of particles in PBS became highly negatively charged, thus might lose the ability to bind siRNA through electrostatic interaction. In addition, the hydrodynamic radius of the as-synthesized HAx-PEI@MSNs were measured by dynamic light scattering (DLS) as shown in Figure 2.2. (A). With an addition over 2 mg HA, the final particle suspension was too viscous to be measured thus DLS not shown.

The specific surface area and pore size of the particles were measured by a nitrogen adsorption/desorption experiment. As shown in Figure 2.2. (C), the specific surface area was 1158.6 m^2/g for phosphonated MSNs. The surface area decreased to 534.9 m^2/g for PEI@MSN and further decreased to 146.3m^2/g after the conjugation of HA. The result was expected as sequential polymer coating on the outer surface would block the access of N_2 gas molecules to the interior mesoporous thus decreasing the specific surface area. The pore size of the particles also varies with the sequential surface modification from 3.0 nm to 2.2 nm, which agreed with the TEM images, indicating some of the conjugation occurred at the pore openings.

In vitro cellular uptake study

To evaluate the transfection efficiency of HA-PEI@MSN as gene delivery vehicle, we use confocal microscopy to visualize the uptake of siRNA/MSNs complex. AlexaFluor-647 dye labeled siQ (control siRNA that has similar molecular structure with siTWIST but not bio-functional) was used as a model gene. The binding process of siRNA with MSNs was performed according to our previous study.[27] The HA-PEI@MSNs were labeled with Dylight-680 as described in the experimental section. F2 cell line was chosen for its high drug resistance and over expression of CD44 receptors. Flow cytometry study was performed using nanoparticles with/without HA. After incubating nanoparticles with cells for 1-hour, 2 hours, and 4 hours, cell culture was washed and monitored with flow cytometry for Dylight-680 signal. From Figure 2.3. (A), the HA-PEI@MSNs were readily uptaken by F2 cells after 1-hour of incubation and maximized at 4 hours. Comparing to PEI@MSNs (with no HA), there was an obvious difference at 4 hours after incubating, showing the enhanced targeting effect of hyaluronic acid. In addition, as shown in Figure

2.3. (B), the SiQ AlexaFluor-647 alone was not present in the cell when used without the nanoparticles. Co-localization of AlexFluor-647(siQ) and Dylight-680(HA-PEI@MSN) in the late endosomes and lysosomes of the cells (Figure 2.4.) indicates the successful uptake of siQ/HA-PEI@MSNs complex into the F2 cells. Moreover, as depicted in Figure 2.5., *in vitro* uptake of HA-PEI@MSNs into F2 cells were analyzed using TEM at different incubation time of 1-hour, 2-hour and 4-hour. From the 1st hour after incubation, MSNs were observed in the cytoplasm of cells transfected.

Western blot analysis of Twist expression in 4T1 cell and F2 cell lines

4T1 triple negative breast cancer cell line was chosen to evaluate the knockdown efficacy of HA-PEI@MSN/siRNA complex. As discussed in the synthesis section, different amount of hyaluronic acid was applied in the conjugation reaction, yielding HA$_{0,\ 0.3,\ 0.5,\ 0.7,\ 1.0}$-PEI@MSNs. Those particles were then complexed with siTWIST and incubated with 4T1 cells. As shown in Figure 2.6. (A), the suppression of Twist was observed early at 24 hours after incubation. With the addition of HA, the knockdown of Twist in 4T1 cells could be maintained over 1 week. Based on the Western results above, MSN with no HA did not completely knock down TWIST. This was shown from the presence of light band at 24 hour and the expression increased overtime, shown from the darker band at 48 hour, 72 hour, and then 1 week. 0.5 HA-tagged MSN resulted in a similar knockdown of TWIST compared to no HA. However, TWIST expression were reduced after 1 week. 0.7 HA-tagged MSN showed the complete knockdown of TWIST as early as 24 hour and greatly reduced at 48 hour. TWIST expression started to reappear at 72 hour and 1 wk. Because of its significance in knocking down TWIST, 0.7 HA-tagged MSN will be used in our animal experiment study.

To quantify the different amount of hyaluronic acid applied and attached to the MSNs, TGA was performed on sample MSN-phos, PEI@MSN and $HA_{0.7,2.0}$-PEI@MSNs. As shown in Figure 2.2. (D), about 17%wt of PEI was electrostatically attached to MSNs, while with the addition of 0.7mg HA (to 10 mg PEI@MSN), 2%wt of HA was conjugated with a reaction efficiency of 35%.

F2 was then selected as a model resistant cell line for ovarian cancer. As shown in Figure 2.6. (B), at the first 24 hours after incubation, suppressed expression of Twist was observed. As F2 was less drug resistant comparing to 4T1 cells, the knockdown was maintained even after one week of treatment. This result showed that HA-PEI@MSNs could significantly enhance the transfection efficiency of siTWIST and knockdown the overexpression of Twist, which would potentially reduce the drug resistance in ovarian cancer cells. With this composition of HA-PEI@MSNs as the delivery vehicle, it was shown in the Sulphorhodamine B (SRB) cell survival assays (Figure 2.6. (C)) that TWIST knockdown via HA0.7-PEI@MSNs significantly sensitizes F2 cells to cisplatin, with IC_{50} reduced from ~40 to ~20 μM.

Preliminary in vivo study with HA-PEI@MSNs as transfection agent

As shown in Figure 2.7., tumor site was visualized by mCherry labeled F2 ovarian cancer cell line under bioluminescence imaging. A reduction of tumor weight and tumor burden were observed when using HA-PEI@MSNs as transfection agent combined with cisplatin as chemotherapy, showing an improved knockdown efficiency of TWIST expression comparing to groups without the presence of MSNs or with siQ as a control non-therapeutic gene. As a result, the survival study using Kaplan-Meier estimate curve

showed a lest steepness with the presence of HA-PEI@MSNs and extend the half survival time from 5 weeks of control group to 7 weeks with only cisplatin treatment to 10 weeks with HA-PEI@MSN transfecting siTWIST combined with cisplatin treatment. This preliminary *in vivo* study showed great potential for the HA-PEI@MSNs as a novel transfection agent for siTWIST.

2.5 Conclusion

In summary, we have designed and engineered a novel type of mesoporous silica nanoparticles based siRNA delivery system. With the introduction of hyaluronic acid as the targeting moiety, the transfection efficiency of PEI@MSNs was greatly enhanced for the delivery of siTWIST by enhancing the uptake of MSNs via the overexpressed CD-44 on targeted cell lines. An optimized ratio between the HA moiety and the PEI layer on the MSNs was found by combined bioassays and cell imaging techniques, showing the improved gene knockdown performance and cellular uptake. In addition, this novel nanoparticle delivery system was investigated *in vitro*, showing promising knockdown of TWIST1 expression, combined with cisplatin chemotherapy, sensitizing the drug resistant cell line to cisplatin treatment. A preliminary animal study using this new developed HA-PEI@MSNs delivery platform showed promising results to reduce the drug resistance. A full animal study to statistically prove the *in vivo* efficacy of this novel transfection agent is presented in the next chapter. In addition, other cancer models are being studied with this HA-PEI@MSNs as a promising theranostic platform.[35,36]

2.6 Figures

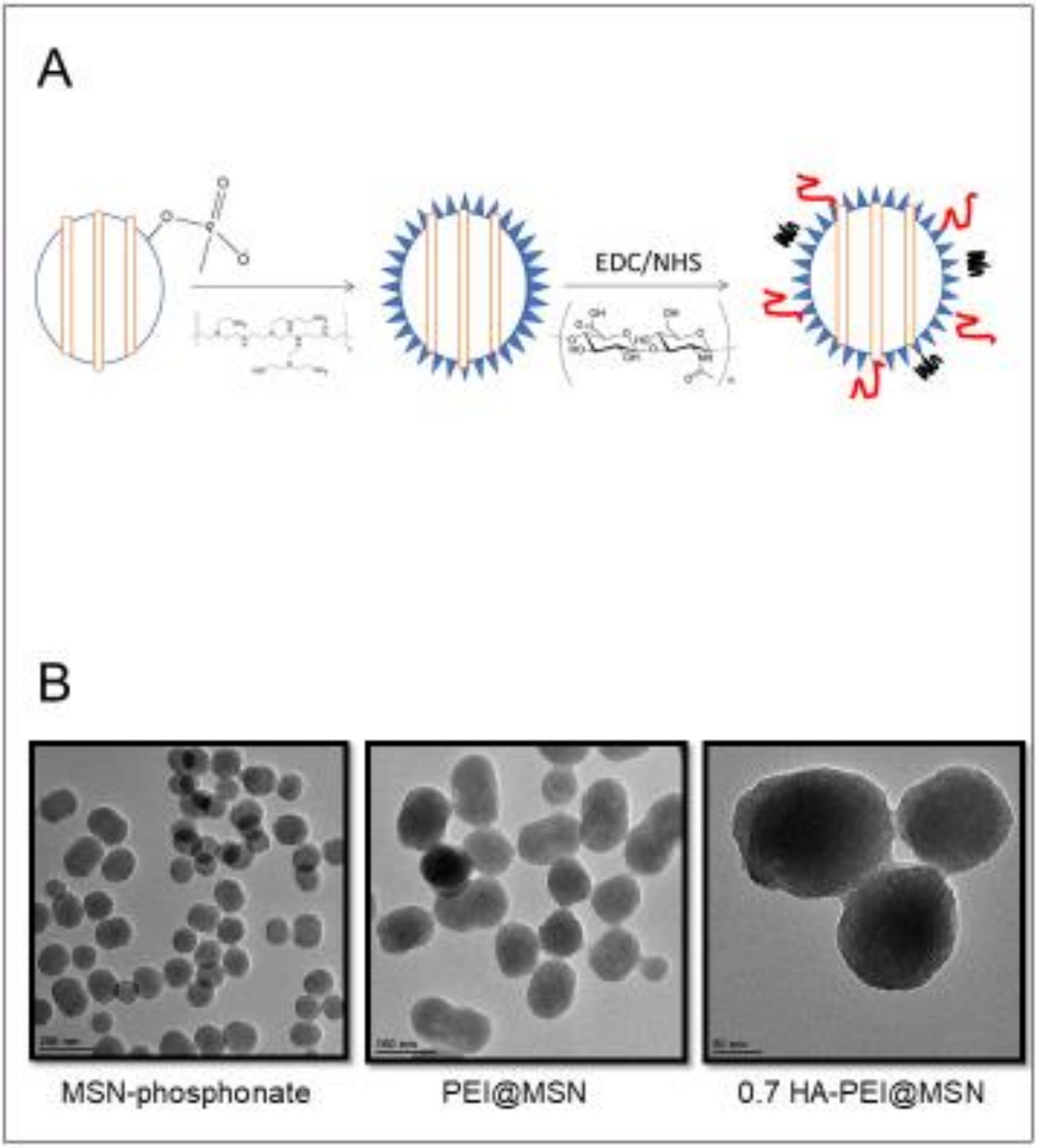

Figure 2.1. (A) Synthesis scheme from MSNs-phosphonate to PEI@MSNs to HA-PEI@MSNs. (B) TEM images of MSN-phosphonate, PEI@MSN and 0.7 HA-PEI@MSN. The scale bars are 200 nm, 100 nm and 50 nm, respectively.

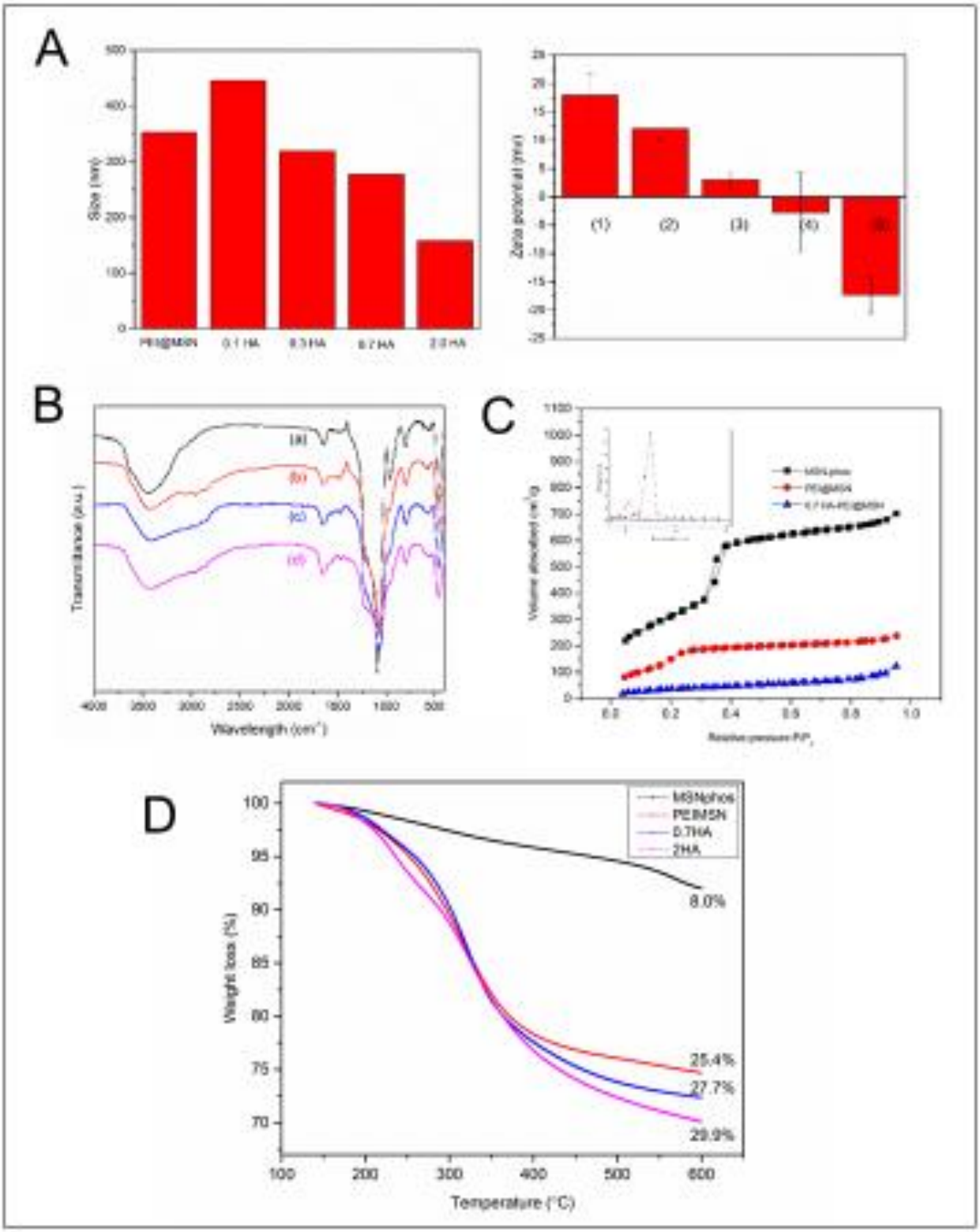
A
Size (nm)
PEI@MSN
0.1 HA
0.5 HA
0.7 HA
2.0 HA
Zeta potential (mV)
(1)
(2)
(3)
(4)
(5)
B
Transmittance (a.u.)
(a)
(b)
(c)
(d)
Wavelength (cm⁻¹)
C
MSNphos
PEI@MSN
0.7 HA-PEI@MSN
D
MSNphos
PEIMSN
0.7HA
2HA
8.0%
25.4%
27.7%
29.9%
Weight loss (%)
Temperature (°C)

Figure 2.2. physiochemical characterizations on the as-synthesized MSNs. (A) Left: DLS sizes of PEI@MSN and HA-PEI@MSN nanoparticles with different amount of HA added, measurement in DI water with 0.1 mg/mL concentration; Right: Zeta potential values of PEI@MSN and HA-PEI@MSN nanoparticles with different amount of HA added, dispersed in DI water with the same concentration. (B) FTIR spectrum of (a) MSN-phosphonate, (b) PEI@MSN, (c) 0.7 HA-PEI@MSN, (d) 2.0 HA-PEI@MSN. (C) N_2 adsorption-desorption isotherms and pore size analysis of MSN-phosphonate, PEI@MSN and 0.7 HA-PEI@MSN. (D) TGA curves of MSN-phosphonate, PEI@MSN, 0.7 HA-PEI@MSN, and 2.0 HA-PEI@MSN.

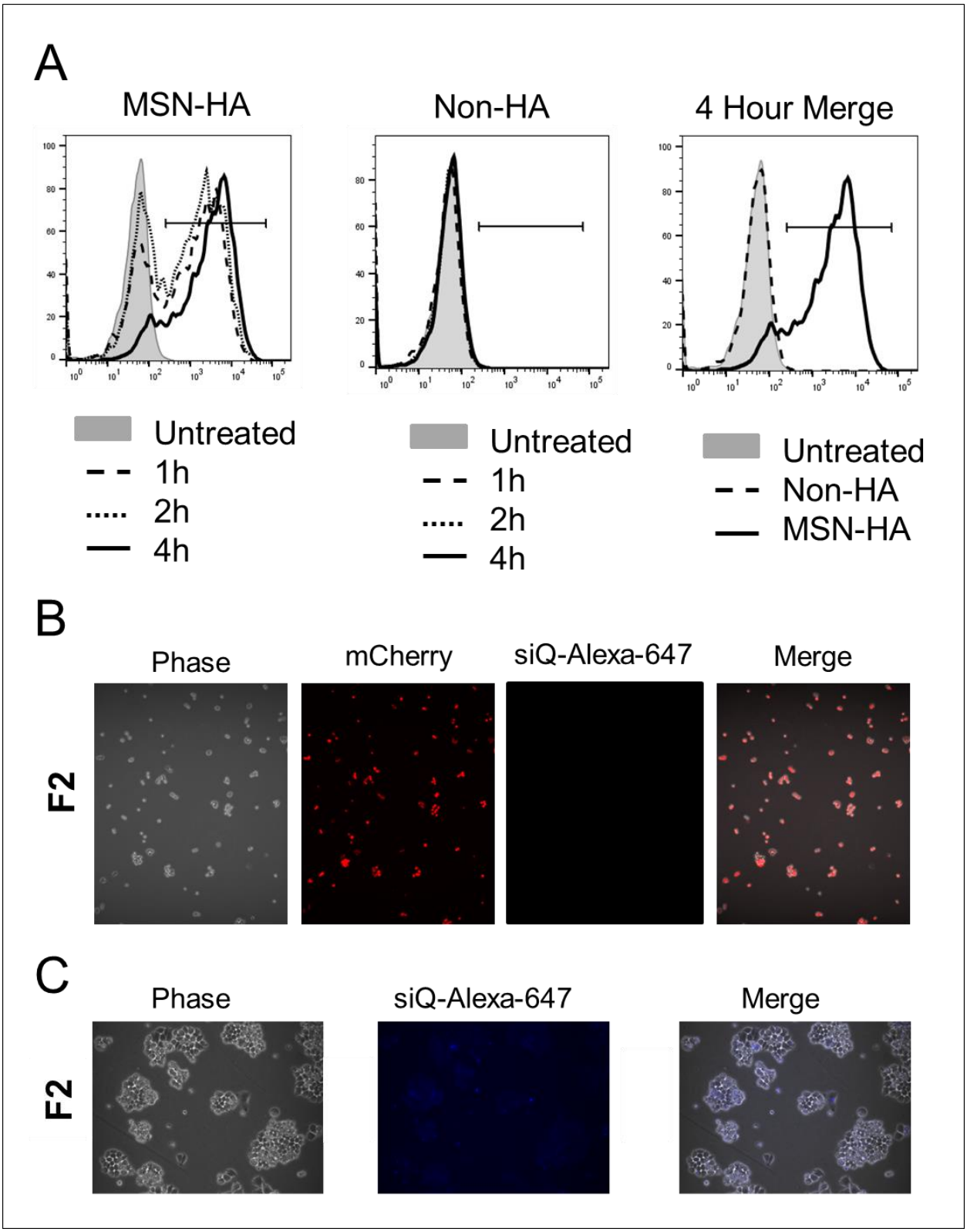
A
MSN-HA
Non-HA
4 Hour Merge
Untreated
1h
2h
4h
Untreated
1h
2h
4h
Untreated
Non-HA
MSN-HA
B
Phase
mCherry
siQ-Alexa-647
Merge
F2
C
Phase
siQ-Alexa-647
Merge
F2

Figure 2.3. Measurement of cellular uptake. (A) Flow cytometry analysis to monitor the binding of DyLight 680 doped nanoparticles (with or without HA functionalization) with F2 cells (target cells) at different incubation time. (B) Confocal laser scanning microscopy investigation of the target ability and co-localization of control siRNA (siQ labeled with Alexa-647) delivered with HA-MSNs to F2 cells whole cell labeled with mCherry. (C) Confocal laser scanning microscopy of siQ delivery without presence of HA-MSNs.

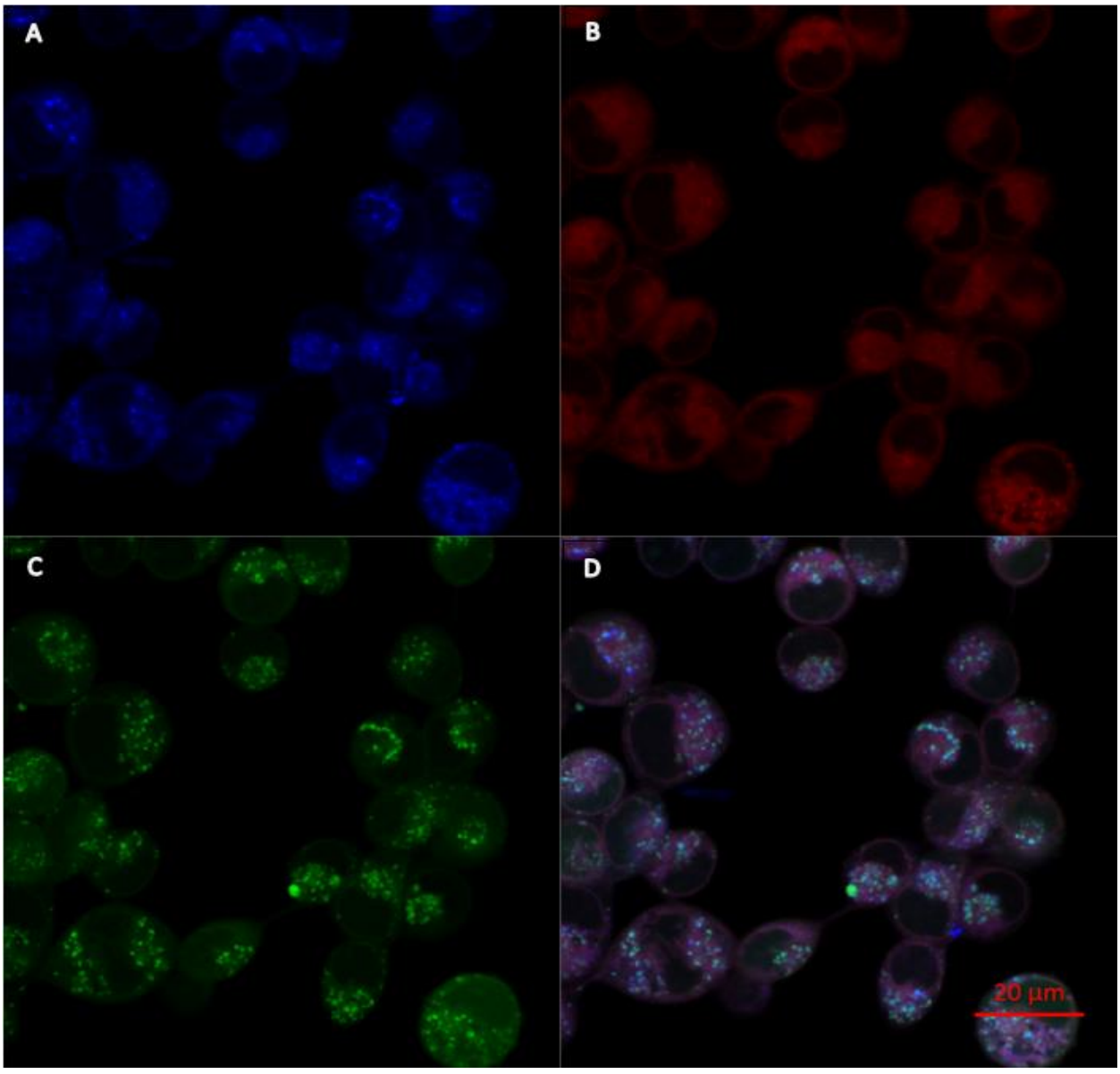
A
B
C
D
20 µm

Figure 2.4. Confocal microscopy demonstrates MSN-HA delivery of si419H into F2 cells. (A) HA tagged MSN-siQ complex distribution inside the cells after 24 hr. (B) LysoTracker probe labelling the lysosomes inside the cells. (C) 4T1P eGFP ffluc cells. (D) Overlay of the pictures, showing that MSN-siQ complexes were taken up by the cells and resided in lysosomes.

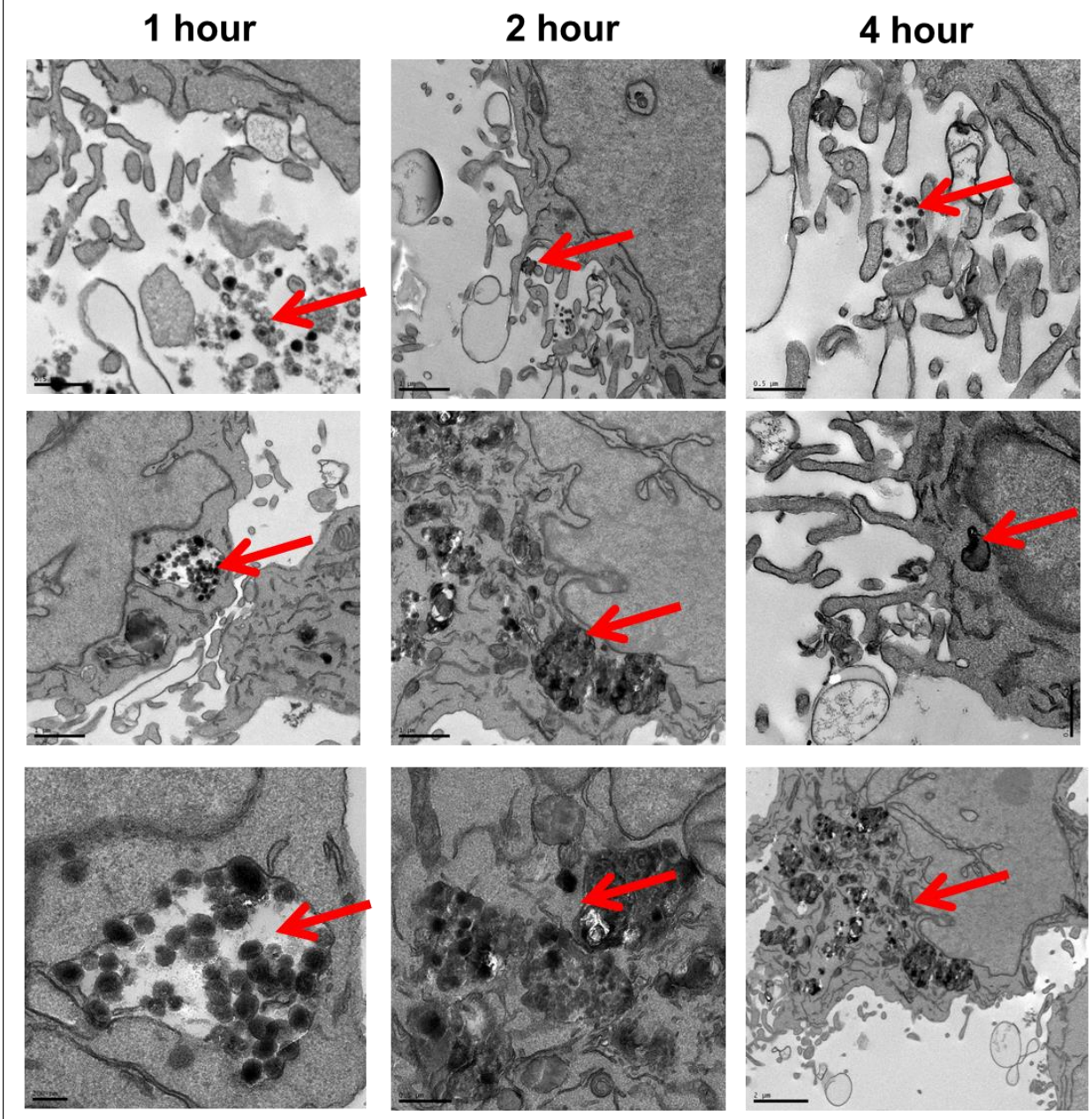
1 hour
2 hour
4 hour

Figure 2.5. TEM images of F2 cells cellular uptake of HA-MSNs after different incubation time period of 1-hour, 2-hour and 4-hour. HA-MSNs were pointed at by red arrows in the images.

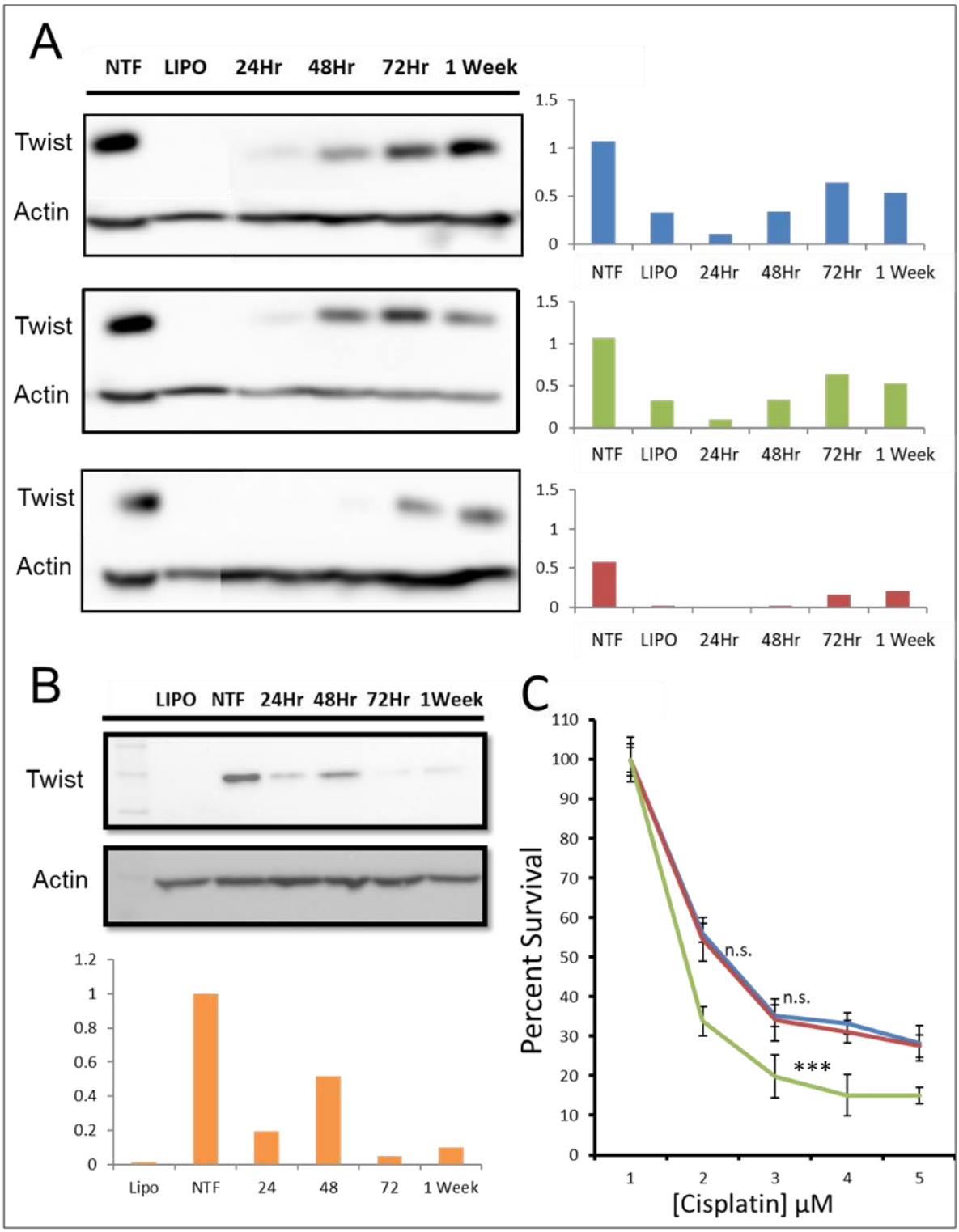
A
NTF LIPO 24Hr 48Hr 72Hr 1 Week
Twist
Actin
1.5
1
0.5
0
NTF LIPO 24Hr 48Hr 72Hr 1 Week
Twist
Actin
1.5
1
0.5
0
NTF LIPO 24Hr 48Hr 72Hr 1 Week
Twist
Actin
1.5
1
0.5
0
NTF LIPO 24Hr 48Hr 72Hr 1 Week
B
LIPO NTF 24Hr 48Hr 72Hr 1Week
Twist
Actin
1.2
1
0.8
0.6
0.4
0.2
0
Lipo NTF 24 48 72 1 Week
C
Percent Survival
110
100
90
80
70
60
50
40
30
20
10
0
n.s.
n.s.
***
1 2 3 4 5
[Cisplatin] µM

Figure 2.6. (A) Western blot results showing the si419H TWIST knockdown in drug resistant cell line 4T1P eGFP fluc, delivered by PEI@MSNs with no HA (blue), by $HA_{0.5}$-PEI@MSNs (Green) and by $HA_{0.7}$-PEI@MSNs (Red). (B) si419H TWIST knockdown in cell line F2 with $HA_{0.7}$-PEI@MSNs. (C) SRB cell survival assay reveals that TWIST knockdown via $HA_{0.7}$-PEI@MSNs significantly sensitizes F2 cells to cisplatin ($P = 0.0054$), IC_{50} is reduced from ~40 μM to ~20 μM. (Statistical significance was determined by two-way repeated measures ANOVA with Tukey's multiple comparison test. *, $P < 0.05$; **, $P < 0.01$; ***, $P < 0.001$; ****, $P < 0.0001$.)

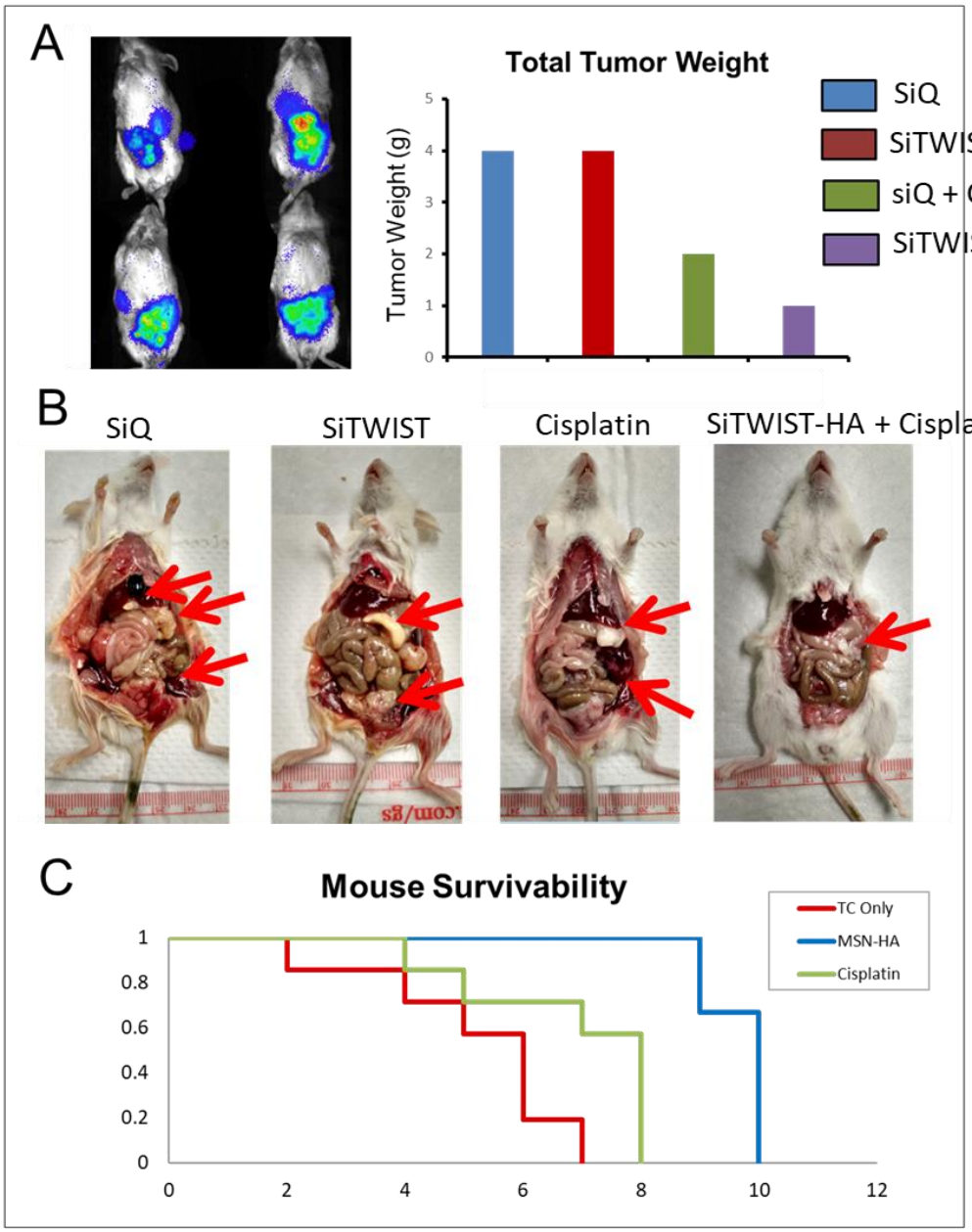
A
Total Tumor Weight
Tumor Weight (g)
0
1
2
3
4
5
SiQ
SiTWIST
siQ + Cisplatin
SiTWIST-HA + Cisplatin
B
SiQ
SiTWIST
Cisplatin
SiTWIST-HA + Cisplatin
C
Mouse Survivability
TC Only
MSN-HA
Cisplatin
0
0.2
0.4
0.6
0.8
1
0
2
4
6
8
10
12

Figure 2.7. (A) Bioluminescence imaging visualizing F2 tumors (untreated mice not shown). Tumors treated with cisplatin has smaller tumor weight than siTWIST or siQ only control mice, while those treated with siTWIST-HA@MSNs plus cisplatin exhibit a further decrease of tumor weight. (B) Mice treated with siQ have similar tumor burden with TWIST knockdown mice. Cisplatin combined with siTWIST-HA@MSNs treatment eliminated much of the tumor mass as compared to cisplatin alone. Arrows indicate tumor foci. (C) Kaplan Meier Curve showing the survival rate of mice with treatment of TC only, cisplatin only and siTWIST-HA@MSNs. (number of mice in experimental group: TC only, cisplatin n=8; siTWIST-HA n=4)

2.7 References

1. Aagaard, L. & Rossi, J. J. RNAi therapeutics: principles, prospects and challenges. *Adv. Drug Deliv. Rev.* **59**, 75–86 (2007).
2. Lima, R. T., Martins, L. M., Guimaraes, J. E., Sambade, C. & Vasconcelos, M. H. Specific downregulation of bcl-2 and xIAP by RNAi enhances the effects of chemotherapeutic agents in MCF-7 human breast cancer cells. *Cancer Gene Ther.* **11**, 309–316 (2004).
3. Takeshita, F. *et al.* Systemic delivery of synthetic microRNA-16 inhibits the growth of metastatic prostate tumors via downregulation of multiple cell-cycle genes. *Mol. Ther.* **18**, 181–187 (2010).
4. Soutschek, J. *et al.* Therapeutic silencing of an endogenous gene by systemic administration of modified siRNAs. *Nature* **432**, 173–178 (2004).
5. Stewart, S. A. *et al.* Lentivirus-delivered stable gene silencing by RNAi in primary cells. *Rna* **9**, 493–501 (2003).
6. Gary, D. J., Puri, N. & Won, Y.-Y. Polymer-based siRNA delivery: perspectives on the fundamental and phenomenological distinctions from polymer-based DNA delivery. *J. Control. Release* **121**, 64–73 (2007).
7. Whitehead, K. A., Langer, R. & Anderson, D. G. Knocking down barriers: advances in siRNA delivery. *Nat. Rev. Drug Discov.* **8**, 129–138 (2009).
8. Verma, I. Somia., N.(1997). *Gene Ther. Probl. Prospect. Nat.* **389**, 239–242.
9. Merdan, T., Kopeček, J. & Kissel, T. Prospects for cationic polymers in gene and oligonucleotide therapy against cancer. *Adv. Drug Deliv. Rev.* **54**, 715–758

(2002).

10. Li, W. & Szoka, F. C. Lipid-based nanoparticles for nucleic acid delivery. *Pharm. Res.* **24**, 438–449 (2007).

11. Wang, J., Feng, S.-S., Wang, S. & Chen, Z. Evaluation of cationic nanoparticles of biodegradable copolymers as siRNA delivery system for hepatitis B treatment. *Int. J. Pharm.* **400**, 194–200 (2010).

12. Singh, N., Agrawal, A., Leung, A. K. L., Sharp, P. A. & Bhatia, S. N. Effect of nanoparticle conjugation on gene silencing by RNA interference. *J. Am. Chem. Soc.* **132**, 8241–8243 (2010).

13. Zhang, W. *et al.* Inhibiting metastasis of breast cancer cells *in vitro* using gold nanorod-siRNA delivery system. *Nanoscale* **3**, 3923–3932 (2011).

14. Lee, J. *et al.* All-in-one target-cell-specific magnetic nanoparticles for simultaneous molecular imaging and siRNA delivery. *Angew. Chemie Int. Ed.* **48**, 4174–4179 (2009).

15. Philipp, A., Zhao, X., Tarcha, P., Wagner, E. & Zintchenko, A. Hydrophobically modified oligoethylenimines as highly efficient transfection agents for siRNA delivery. *Bioconjug. Chem.* **20**, 2055–2061 (2009).

16. Urban-Klein, B., Werth, S., Abuharbeid, S., Czubayko, F. & Aigner, A. RNAi-mediated gene-targeting through systemic application of polyethylenimine (PEI)-complexed siRNA *in vivo*. *Gene Ther.* **12**, 461–466 (2005).

17. Godbey, W. T., Wu, K. K. & Mikos, A. G. Tracking the intracellular path of poly (ethylenimine)/DNA complexes for gene delivery. *Proc. Natl. Acad. Sci.* **96**, 5177–5181 (1999).

18. Boussif, O. *et al.* A versatile vector for gene and oligonucleotide transfer into cells in culture and *in vivo*: polyethylenimine. *Proc. Natl. Acad. Sci.* **92**, 7297–7301 (1995).

19. Xia, T. *et al.* Polyethyleneimine Coating Enhances the Cellular Uptake of Mesoporous Silica Nanoparticles and Allows Safe Delivery of siRNA and DNA Constructs. *ACS Nano* **3**, 3273–3286 (2009).

20. Clamme, J. P., Azoulay, J. & Mély, Y. Monitoring of the formation and dissociation of polyethylenimine/DNA complexes by two photon fluorescence correlation spectroscopy. *Biophys. J.* **84**, 1960–1968 (2003).

21. Li, Z., Barnes, J. C., Bosoy, A., Stoddart, J. F. & Zink, J. I. Mesoporous silica nanoparticles in biomedical applications. *Chem. Soc. Rev.* **41**, 2590 (2012).

22. Finlay, J. *et al.* Mesoporous silica nanoparticle delivery of chemically modified siRNA against TWIST1 leads to reduced tumor burden. *Nanomedicine Nanotechnology, Biol. Med.* **11**, 1657–1666 (2015).

23. Meng, H. *et al.* Codelivery of an optimal drug/siRNA combination using mesoporous silica nanoparticles to overcome drug resistance in breast cancer *in vitro* and *in vivo*. *ACS Nano* **7**, 994–1005 (2013).

24. Xia, T. *et al.* Polyethyleneimine coating enhances the cellular uptake of mesoporous silica nanoparticles and allows safe delivery of siRNA and DNA constructs. *ACS Nano* **3**, 3273–3286 (2009).

25. Lee, J. M., Dedhar, S., Kalluri, R. & Thompson, E. W. The epithelial–mesenchymal transition: new insights in signaling, development, and disease. *J. Cell Biol.* **172**, 973–981 (2006).

26. Kalluri, R. & Weinberg, R. A. The basics of epithelial-mesenchymal transition. *J. Clin. Invest.* **119**, 1420–1428 (2009).

27. Roberts, C. M. *et al.* Nanoparticle delivery of siRNA against TWIST to reduce drug resistance and tumor growth in ovarian cancer models. *Nanomedicine Nanotechnology, Biol. Med.* **13**, 965–976 (2017).

28. Dufaÿ Wojcicki, A. *et al.* Hyaluronic acid-bearing lipoplexes: Physico-chemical characterization and *in vitro* targeting of the CD44 receptor. *J. Control. Release* **162**, 545–552 (2012).

29. Yang, X. *et al.* MDR1 siRNA loaded hyaluronic acid-based CD44 targeted nanoparticle systems circumvent paclitaxel resistance in ovarian cancer. *Sci. Rep.* **5**, 1–9 (2015).

30. Cai, Y., López-Ruiz, E., Wengel, J., Creemers, L. B. & Howard, K. A. A hyaluronic acid-based hydrogel enabling CD44-mediated chondrocyte binding and gapmer oligonucleotide release for modulation of gene expression in osteoarthritis. *J. Control. Release* **253**, 153–159 (2017).

31. Lin, W. J., Lee, W. C. & Shieh, M. J. Hyaluronic acid conjugated micelles possessing CD44 targeting potential for gene delivery. *Carbohydr. Polym.* **155**, 101–108 (2017).

32. Chen, Z. *et al.* Biomineralization inspired surface engineering of nanocarriers for pH-responsive, targeted drug delivery. *Biomaterials* **34**, 1364–1371 (2013).

33. Shahin, S. A. *et al.* Hyaluronic acid conjugated nanoparticle delivery of siRNA against TWIST reduces tumor burden and enhances sensitivity to cisplatin in ovarian cancer. *Nanomedicine Nanotechnology, Biol. Med.* **14**, 1381–1394

(2018).

34. Finlay, J. *et al.* Mesoporous silica nanoparticle delivery of chemically modified siRNA against TWIST1 leads to reduced tumor burden. *Nanomedicine Nanotechnology, Biol. Med.* **11**, 1657–1666 (2015).

35. Contreras, A. *et al.* Optimizing therapies for drug-resistant ovarian cancer stem cells using aCAM-PDX model. (2018).

36. Glackin, C. A. *et al.* Hyaluronic acid conjugated nanoparticle delivery of siTWIST reduces tumor burden and enhances chemosensitivity in ovarian cancer. (2018).

Chapter 3

Hyaluronic acid conjugated nanoparticle delivery of siRNA against TWIST reduces tumor burden and enhances sensitivity to cisplatin in ovarian cancer

This chapter is based on work done with collaborators Sophia A. Shahin, et. al. at Beckman Research Institute, City of Hope for biological assays and mouse model tests. This study is summarized and published as follow:

Shahin, S. A., Wang, R., Simargi, S. I., Contreras, A., Echavarria, L. P., Qu, L., ... & Zink, J. I. (2018). Hyaluronic acid conjugated nanoparticle delivery of siRNA against TWIST reduces tumor burden and enhances sensitivity to cisplatin in ovarian cancer. Nanomedicine: Nanotechnology, Biology and Medicine, 14(4), 1381-1394.

3.1 Abstract

TWIST protein is critical to development and is activated in many cancers. TWIST regulates epithelial-mesenchymal transition, and is linked to angiogenesis, metastasis, cancer stem cell phenotype, and drug resistance. The majority of epithelial ovarian cancer (EOC) patients with metastatic disease respond well to first-line chemotherapy but most relapse with disease that is both metastatic and drug resistant, leading to a five-year survival rate under 20%. We are investigating the role of TWIST in mediating these relapses. We demonstrate TWIST-siRNA (siTWIST) and a novel nanoparticle delivery platform to reverse chemoresistance in an EOC model. Hyaluronic-acid conjugated mesoporous silica nanoparticles (MSN-HAs) carried siTWIST into target cells and led to sustained TWIST knockdown *in vitro*. Mice treated with siTWIST-MSN-HA and cisplatin exhibited specific tumor targeting and reduction of tumor burden. This platform has potential application for overcoming clinical challenges of tumor cell targeting, metastasis and chemoresistance in ovarian and other TWIST overexpressing cancers.

3.2 Introduction

Recurrent epithelial ovarian cancer (EOC) is almost uniformly lethal. EOC is responsible for 90% of all cancers of the ovaries;[1] and about 70% of women diagnosed with EOC are already considered to be in advanced stage.[1] Despite successful initial surgery and chemotherapy, over 65% of advanced EOC will reoccur, and only 15-30% of recurrent disease will respond to chemotherapy.[2–5] To this end, tumor recurrence and metastases are primarily responsible for treatment failure in over 90% of patients with metastatic

disease.[6] Thus, recurrent metastatic disease is a major clinical challenge without effective therapy. The cancer stem cell (CSC) hypothesis explains the difficulty of treating these cancers. Rare cells within a tumor exhibit characteristics of stem cells.[7] These CSC sustain mutations that allow for expression of embryonic factors that contribute to chemoresistance and metastasis.[8,9] Currently, no EOC therapies target the CSC specifically. Until such therapies are developed, recurrent tumors will remain untreatable.

Chemoresistant CSC have been shown to be the leading cause of relapse and metastasis in many cancers.[10] Activation of several mechanisms in CSCs, including drug efflux or inactivation, signaling pathways that enhance survival, and altered DNA damage response, is known to lead to chemoresistance.[9] Moreover, EOC tumors express high levels of epithelial-mesenchymal transition (EMT) markers such as TWIST, which play a vital role in cancer metastasis (Figure 1A).[11,12] TWIST is found to upregulated in almost all metastatic cancers, including ovarian.[12–14] Furthermore, is it well known that TWIST and EMT control chemoresistance and stemness in cancer (Figure1B).[15–17] TWIST expression directly affects EMT markers by overexpressing N-cadherin and vimentin, and down-regulating E-cadherin (Figure1B).[18] Our group has shown knockdown of TWIST leads to reduced tumor growth, burden, and angiogenesis in melanoma,[19] and abridged the invasive phenotype in triple-negative breast cancer.[20] However, nuclear localization makes targeting transcription factors such as TWIST nearly impossible with small molecule drugs.[21] To bypass this problem, we emply small interfering RNAs (siRNAs). We have developed a therapeutic siRNA against TWIST (Figure 1C), and have designed a novel nanoparticle-based delivery platform to specifically target CSCs. We created a polyethylenimine (PEI) coated mesoporous silica nanoparticle (MSN) conjugated with

hyaluronic acid (MSN-HA). We have previously shown effective delivery to tumor cells using a similar modality, both *in vitro* and *in vivo* of ovarian, melanoma, and breast cancer.[19,20,22]

In this study, we aimed to build upon our previous work utilizing MSN nanoparticle therapy and introduce our novel siTWIST conjugated MSN-HA technology to a highly metastatic ovarian cancer model. We hypothesized MSN-HA-siTWIST would knock down TWIST and sensitize CSC to chemotherapeutics via HA-CSC targeting of its native ligand, CD44. Additionally, we studied the tumor-specific targeting capability of our MSN-HAs resulting in significant selectivity, with better delivery efficiency and improved antitumor therapeutic effect as compared to current delivery systems, such as viral and non-viral vectors or lipid and polymer vesicles.[10,22–25] We certify this novel MSN-HA-siTWIST drug delivery platform a promising therapy to inhibit metastasis and acquired drug resistance in cancer.

3.3 Experimental

Cell Culture

F2 and Ovcar8 cell lines were grown in RPMI 1640 (10% fetal bovine serum and 1% penicillin/streptomycin) (Genesee Scientific) in a tissue culture incubator at 37°C, 5% CO2, and 90% humidity. Cells were passaged every 2-4 days using 0.25% trypsin (Genesee Scientific). Where indicated, cells were transfected with Lipofectamine 2000 (Thermo Fisher). F2 cells are cisplatin resistant cells taken from primary patient tissue with high grade serous ovarian cancer and were a gift from Dr. Gil Mor at Yale University.

Optimization of Ovcar8 for in vivo use

For mouse experiments, Ovcar8 cells were stably transfected with CMV-p:EGFP-ffluc pHIV7 as described previously.[26] This resulted in expression of an eGFP-firefly luciferase (ffluc) fusion protein. Furthermore, to increase engraftment efficiency and homogeneity of the cell population, Ovcar8 cells were passaged through mice. Ovcar8-GFP+ffluc cells were injected intraperitoneally (IP) and allowed to form tumors. Cells were harvested after 37 days and used to establish the Ovcar8-IP line.

3.3.3 siRNA design

siRNAs against TWIST were designed based on shRNAs that were previously validated.[18,20] Sequences are: si419 guide, 5'-AAUCUUGCUCAGCUUGUCCUU-3' and si419 passenger, 5'-GGACAAGCUGAGCAAGAUU-3'. Non-targeting control siRNA (siQ) was AllStars Negative Control siRNA, labeled with AlexaFluor-647 from Qiagen. For *in vivo* studies, 2'-O-methyluracil and inverted abasic ribose chemical modifications were made to the si419 passenger strand, as illustrated in Figure 3A.[19,23]

3.3.4 MSN-HA design and delivery

MSNs were synthesized utilizing the sol-gel method as described previously.[19] First, 250mg 95% cetyltrimethylammonium bromide (CTAB) was dissolved in 120mL of water with 875µl 2M sodium hydroxide solution, at 80°C. Next, 1.2mL of 98% tetraethylorthosilicate was added. After 15 min, 300µl of 42% 3-(trihydroxysilyl) propyl methylphosphonate was added, and the resulting mixture was stirred for 2hrs. Particles were collected using centrifugation and washed with methanol. Acidic methanol was then used to remove any remaining CTAB surfactants. Zeta potential at 50 µg/mL was 43.75 mV (Aldrich, St. Louis, MO).[19] Particles were ~120 nm in diameter, with 2.5 nm pores. 1.8

kD-polyethyleneimine (PEI) was electrostatically attached to the particle surface to provide positive charge, to which negatively charged siRNA is attached. HA is covalently bonded to the amine groups in the PEI using EDC-NHS coupling reaction.[27] To complex siRNA for *in vitro* experiments, 10 µL siRNA at 10µM was mixed with 70 uL MSNs at 500 µg/mL and 20 µL water. The mixture was incubated overnight at 4°C on a roller. The following day, 100 µL of MSN-siRNA was added to each well of a 6-well plate containing 1900 µL normal medium.

Fluorescent MSNs were prepared by adding 500 µL DyLight 680 NHS-Ester that reacted with the MSN amine groups. After dye labeling, the particles were thoroughly washed and dispersed in ethanol for later surface coating.

3.3.5 Fluorescence Microscopy

To verify cell uptake of the nanoparticle-siRNA complexes, cells were imaged immediately before harvesting. Phase and fluorescent images to detect siQ-AlexaFluor-647 were done using a Nikon TE-2000S-microscope and SPOT Advanced software (Diagnostic Instruments).

3.3.6 Confocal Microscopy

Ovcar8-IP cells were seeded into a 3.5 cm glass bottom tissue culture dish. Following attachment (24 hr), 2 mL of fresh medium replaced the old medium. Next, MSN-HA-siQ (labeled with AlexaFluor® 647) was added to the cells at final concentration of 17.5 ng/µL (MSN) and 5 nM (siQ) and incubated for an additional 48 hours. Cells were then treated with LysoTracker Red (Thermo Fisher Scientific). Confocal images were obtained using the Zeiss LSM700 Confocal Microscope (Zeiss AG).

Western Blotting

Following Lipofectamine 2000 or MSN-HA delivery of siRNA, cells were pelleted and lysed in RIPA buffer. Protein concentration was determined by BCA assay (Thermo Fisher). Following SDS-PAGE, protein was transferred to Amersham PVDF membrane (Genesee Scientific) using a BioRad Trans-Blot SD semi-dry transfer unit. Blots were then blocked in milk for one hour at room temperature or overnight at 4°C. Incubation with primary antibody took place for one hour at room temperature or overnight at 4°C, Antibodies were diluted in 5% milk, with 0.1-0.2% Tween-20. Antibodies used were TWIST 2c1a (Santa Cruz Biotechnology, Dallas, TX) at 1:250-1:500 dilution, β-Actin, A1978 (Sigma Aldrich) at 1:2500-1:5000 dilution; and Horseradish Peroxidase (HRP) conjugated anti-mouse secondary antibodies. For westerns, the Syngene Pxi4 digital blot imager and Michigan Diagnostics FemtoGlow chemilumescent substrate were used.

Sulphorhodamine B Cell Survival Assays

Ovcar8-IP cells were plated in 6 well plates and allowed to adhere overnight. The following day, cells were transfected with siQ or MSN-HA-si419. After 48-72 hours, cells were transferred to 96 well plates at 5,000 cells per well and allowed to adhere overnight. The following day cells were treated with cisplatin at a series of concentrations (cells not treated with cisplatin served as controls). After 72 hours, cells were fixed in 10% trichloroacetic acid for 1 hour at 4°C, washed with water, and dried. Cells were stained in 0.4% sulphorhodamine B (SRB) in 1% acetic acid for 15 minutes at room temperature and then washed 3-4 times with 1% acetic acid until no further color was present in the wash. Any stray SRB on the walls of the wells was removed, and stained cells were dried

for 10 minutes. SRB was solubilized in 10 mM Tris base and color intensity was quantified by absorbance at 570 nm. Each condition was normalized to its own untreated control.

Animal Studies

The animal studies conducted in these experiments were done in accordance with the protocol approved by the Institutional Animal Care and Use Committee at the City of Hope Beckman Research Institute. High quality humane care for all animal subjects was implemented for this study. A total of 60 female NOD.Cg-PrkdcscidIl2rgtm1Wjl/SzJ (NSG) mice (The Jackson Laboratory, Bar Harbor, ME) were used. Ten-week-old mice were administered an IP of 2.5 x 106 Ovcar8-IP cells in 200 µl of RPMI media. For all studies, mice were placed into five groups: MSN-HA-siQ, MSN-HA-siTWIST, CISPLATIN, MSN-siTWIST + cisplatin, and MSN-HA-siTWIST + cisplatin (n=8 or n=12). Previous reports show no cellular uptake without MSNs,[19] thus a siRNA-only group was not added to this study. Bioluminescent imaging of mice (using Xenogen IVIS 100 biophotonic imaging system, STTARR) commenced seven days after injection of tumor cells in order to ensure engraftment, and continued once a week for four weeks. Mice were given a 100 µL IP injection of 20 mg/mL D-Luciferin (PerkinElmer, Waltham, MA). Ten minutes after the D-luciferin injection, mice were anesthetized with isoflurane (2%-5%) and placed in the biophotonic imager, and images were taken within two minutes. An alfalfa-free version of the regular rodent diet (alfalfa-free CA-1) was administered to the siQ mice to prevent autofluorescence from the regular diet. Intravenous (IV) versus intraperitoneal (IP) injections of MSN-HA-siRNA were conducted one week after the inoculation of Ovcar8-IP cells and done once or twice per week for a total of seven weeks. Mice received 105µl of 500ng/µl MSN complexed with 15µl of 10µM siRNA per week, with one full dose (n=8

and n=12, respectively). This is equivalent to 2.5mg MSN/week. Weekly 3mg/kg IP cisplatin injections were given starting two weeks after initial inoculation of tumor cells to ensure all mice received same amount of chemotherapy. Lastly, animals were euthanized via CO_2 asphyxiation followed by necropsy. Both primary tumors and disseminated masses were dissected from adjacent tissue and weighed. Mice were imaged for biodistribution studies. Tumors, spleen, kidney, uterus and liver were imaged ex vivo to detect the location of both the Ovcar8-IP cells and MSN-HA. Efficacy data is presented from mice dosed once per week with MSN-HA-siRNA.

Pathology

Hematoxylin and eosin (H&E) and CD44 staining was conducted on tumor samples obtained at necropsy and were processed in The Pathology Core Laboratory at the City of Hope Department of Pathology and Laboratory Medicine.

Quantitative PCR

Total cellular RNA was isolated using the RNeasy Plus kit (Qiagen). An equal amount of RNA for all conditions was used as a template for cDNA synthesis using the iScript cDNA Synthesis kit with provided random primers (Bio-Rad, Hercules, CA). Quantitative RT-PCR (qPCR) was performed in triplicate using 500 ng/well cDNA and Maxima SYBR Green Master Mix (Thermo Fisher Scientific) in 25 µL reactions. Cycling was conducted in a Bio-Rad iQ5 thermal cycler for 40 cycles (95°C, 15 s; 57°C, 60 s; 79°C, 30 s) followed by melt curve analysis. Data were analyzed using Bio-Rad iQ5 software (2−ΔΔCt method, normalized to β-Actin).

Statistics

All *in vivo* data was analyzed using one-way ANOVA with correction for multiple comparisons, comparing all groups to CISPLATIN treatment group. Additionally, an unpaired t-test with Welch's correction was used to compare tumor number and weight between cisplatin alone and the combination cisplatin + si419H treatment groups. All analyses were done using Prism 6 software: * $p < .05$, ** $p < .01$, *** $p < .001$, **** $p < .0001$

3.4 Results and discussion

MSN-HA delivered siRNA knocks down TWIST *in vitro* in an ovarian cancer model

Our previous work demonstrated the efficacy of our siRNA targeting TWIST (si419 sequence in Figure 1C).[19,20,22] Thus, we utilized Lipofectamine 2000 transfection to examine the effect of si419 in Ovcar8-IP-eGFP cells. TWIST expression was knockdown over 90% within 24 hours and completely inhibited as soon as 72 hours (Figure 1D). Once our si419 was validated, we built upon our recent success with MSNs and introduced MSN-HAs as a delivery vehicle, due to the fact that without a carrier, no siRNA enters target cells (Figure 1E). The MSN-HA specifically targets CSCs through its native ligand CD44.[25,28,29] Much work has focused on attempting to target CD44 in an attempt to improve drug delivery to only malignant tissue and reduce off-target affects. The PEI is electrostatically attached to the MSN surface to provide positive charge, to which negatively charged siRNA is subsequently attached. Hyaluronic acid is covalently bond to the amine groups in the PEI using EDC-NHS coupling reaction and seen using TEM (Figure 2A, B and Supplementary Figure 1).[27] In order to verify that MSN-HAs successfully delivered siRNA into target cells, we conjugated MSN-HAs with AlexaFluor-

647 tagged siQ control siRNA. Microscopy revealed increased cell uptake of labeled siRNA in Ovcar8-IP-eGFP cells (Figure 2C). Our previous studies show 0.000082 mgs of the original 0.0001mgs siRNA delivered remain on the MSN in culture.[23] Furthermore, MSN-HA complexed with siTWIST (MSN-HA-siTWIST) successfully knocked down TWIST within 24 hours post transfection, and successfully uptake into cells as soon as an hour (Figure 2D, Supplementary Figure 2).

Optimization of siTWIST sequence for in vivo therapy evaluation

In order to improve siRNA uptake *in vivo*, it was reformed to bypass the issues of nuclease degradation and immune activation by siRNAs. We achieved this by chemically modifying the si419 passenger strand to create si419 hybrid siRNA (si419H, Figure 3A). In order to promote nuclease resistance of the siRNA duplex, 2'-O-methyl and inverted abasic ribose (iaB) modifications were added.[30,31] iaB avoids the loading of the passenger strand into RISC, which then improves the potency of siRNA by safeguarding which duplexes bind to TWIST mRNA, leading to efficient knockdown and successful silencing of TWIST.[30]

MSN-HAs efficiently deliver siRNA and knockdown TWIST leading to chemosensitivity of ovarian cancer cells

Confocal microscopy demonstrated that treatment of MSN-HA to Ovcar8-IP-eGFP cells resulted in siQ co-localizing in the late endosomes and lysosomes of the cells, as evidenced by LysoTracker dye overlay (Figure 3B). Specifically, this is the perinuclear space of the cell, which was expected and have previously revealed.[19,20,22] Transfection of MSN-HA-siTWIST in both Ovcar8-IP-eGFP and F2 cells caused robust knockdown of TWIST as soon as 24 hours (Figure 3D). Furthermore, sulphorhodamine B (SRB) based

cell survival assays revealed sensitization of both ovarian cancer cell lines to standard chemotherapy, cisplatin, following MSN-HA-mediated TWIST (MSN-HA-siTWIST) knockdown (Figure 3C, data only shown for Ovcar8-IP-eGFP cells). Cisplatin resistant cells were significantly sensitized to the drug, with approximately one log difference in IC50 (~60 to ~5 μM).

Ovarian tumor growth is significantly inhibited by MSN-HA-siTWIST and chemo combination therapy

Mice were treated weekly for seven weeks with MSN-HA-siQ, MSN-HA-siTWIST, CISPLATIN alone, MSN-siTWIST + cisplatin, or MSN-HA-siTWIST + cisplatin. After seven weeks of therapy, mice in the negative control (siQ) group established significant tumors which metastasized as illustrated by bioluminescent photon flux measurements (Figure 4). The mice in the siTWIST treatment group produced relatively smaller tumors, with a 40% drop in bioluminescent signal after seven weeks of therapy in comparison to the siQ controls. The chemotherapy only treatment mouse group (CISPLATIN only) was left with 60% less tumor than the siQ control. MSN-siTWIST with cisplatin, without HA, provided similar results to our previous studies,[32] reducing tumor volume an additional 20% compared to cisplatin alone; whereas the MSN-HA-siTWIST with cisplatin chemotherapy treatment group (MSN-HA-siTWIST + cisplatin) exhibited the most promising outcome, with almost 90% decrease in tumor burden as compared to the siQ control and measured by bioluminescence (Figure 4).

The intraperitoneal cavity of mice from the MSN-HA-siTWIST + cisplatin group was substantially healthier when compared to MSN-HA-siQ control mice (Figure 6A).

Moreover, MSN-HA-siQ control mice developed great amounts of tumor, metastasis, and ascites as compared to MSN-HA-siTWIST + cisplatin group (Figure 5 A-C) which showed no large dispersed lesions. It is important to note that cisplatin + MSN-siTWIST hindered cancer growth by almost 50%, cumulatively, (Figure 5, A-C), as shown previously.[32] However, MSN-HA-siTWIST + cisplatin combination therapy inhibited tumor growth to an even more significant degree, with almost a 75% drop in number of tumor in comparison to CISPLATIN alone and 90% compared to controls (Figure 5, A-C). A similar trend was seen for proportion of mice developing ascites and metastasis (Figure 5 B-C). Administration of the therapy, IP vs. IV did not appear to affect the positive outcome of reduced tumor burden (Figure 5D).

MSN-HA-siTWIST combination therapy demonstrated EMT inhibition in ovarian tumors

*C*ollected tumors were analyzed for the relative mRNA quantities of TWIST, Vimentin, N-Cadherin, and E-Cadherin (EMT markers). There was a significant reduction in the amount of TWIST, Vimentin, and N-Cadherin in the MSN-HA-siTWIST cisplatin combination therapy treated mice when compared to the control mice (MSN-HA-siQ) (Figure 6, B-D). The average relative reduction of TWIST and N-Cadherin for MSN-HA-siTWIST + cisplatin mice was less than that of those treated with MSN-siTWIST + cisplatin (no HA) ($P = 0.001$), though no significant difference was observed for Vimentin or E-Cadherin. Thus, these data suggest inhibition of EMT is promising through the delivery of TWIST siRNA utilizing MSN-HA as a delivery vehicle.

MSN-HAs only accumulate at tumor sites with no evidence of off targeting effects

In order to determine if our novel MSN-HAs specifically localized at CSC tumor sites *in vivo*, we performed fluorescent imaging of siQ treated mice at necropsy. Ovcar8-IP-eGFP cells successfully produced primary tumors (ovaries) and at metastatic sites (Figure 7 B, D and F). Moreover, MSN-HAs carrying siRNA only penetrated and accumulated inside these primary tumors and metastatic sites (Figure 7 C and F), and not in any other peritoneal tissue (Figure 8) or organ examined. Most importantly, tumor uptake of MSN-HAs was significantly greater than that of MSNs without HA (Figure 7 B and C) in the primary tumor site (ovary). This data validates the increased targeting effect HA provides to the tumor sites. Moreover, overlay of GFP (tumor) and DYLIGHT (MSN-HA) fluorescent filters further confirms MSN-HAs only accumulate at tumor sites with no evidence off targeting signal (Figure 7F, 8A-C). Lastly, CD44 antibody staining confirms MSN-HA to CD44 CSC specific targeting (Figure 8D).

DISCUSSION

Our data elucidate a mechanism of CSC regulation in EOC via MSN-HA-siTWIST chemo-combination therapy, and proposes treatment strategies that specifically target CSCs to arrest recurrent metastatic disease. We have developed a treatment strategy that specifically targets CSCs to halt recurrent metastatic disease. Currently, no EOC therapies target CSCs specifically. These cancer-related events include cancer invasion, metastasis, and resistance to apoptotic signals, including chemotherapy. The process of EMT allows epithelial cancer cells to undergo a phenotypic switch that confers upon these otherwise polarized and immobile cells the capacity to become migratory and highly invasive mesenchymal cells.[33] Thus in cancer, EMT is a pre-requisite for metastasis.[34] In addition to the metastatic process, research in EMT has focused in two additional areas:

1) the correlation between stemness and EMT;[35–38] 2) the association between EMT and the development of drug resistance.[39–42] This work provides increasing evidence suggesting a relationship between EMT, stemness, and drug resistance and there is a need to understand how these processes correlate and how chemotherapy may accelerate these changes. The outcome of this work may provide important insight into these biological processes.

Among numerous drug delivery systems, such as viral and non-viral vector, or lipid and polymer vesicles, nanoparticles are a preferred method of choice due to their vast applications in medicine. MSNs are proven effective delivery vehicles of DNA vectors and siRNA therapeutics. Viral and non-viral vectors have been investigated for gene silencing;[10] however, numerous studies have shown that viral vectors are associated with concerns of systemic toxicity and immunogenicity, even when locally injected into the tumor site.[10,43] Non-viral vectors are considered safer, however MSNs have large surface area, tunable pore sizes, and encapsulate molecules such as drugs.[10,25,28,29,43] Lastly, silica has high electron contrast compared to polymers which facilitate TEM analysis and enables quantification of the loading efficiency of siRNA.[10,24,25,43]

To our knowledge, this is the first example of silencing TWIST utilizing a novel MSN-HA delivery system in ovarian cancer models. Here we show the efficacy of chemically-modified-siRNA for *in vivo* use against TWIST in EOC models. Moreover, we demonstrate substantial TWIST knockdown utilizing MSN-HA-siTWIST *in vitro*. TWIST has been shown to be significantly associated with metastasis, EMT, drug resistance, and poor prognosis,[12,44–47] thus making it an optimal target for ovarian cancer therapy. We and others have shown that the effective knockdown of TWIST leads to a decrease in motility,

followed by an increase in chemotherapy sensitivity in ovarian cancer.[22,32,47] The delivery of our siRNA by MSN-HA was shown to have a profound effect on both TWIST silencing and chemoresistance in the EOC model (Figure 3 C-D). These data add to the growing evidence that TWIST is a clinically significant therapeutic target for the treatment of EOC and other solid tumors.

MSN-siTWIST alone demonstrated sufficient delivery of siRNA cargo into ovarian cancer cells *in vitro* and led to substantial knockdown of TWIST and chemosensitivity *in vivo* (Figures 4 and 5) as compared to previous studies.[22] However, the substantial improvement of ovarian tumor chemosensitivity, reduction in tumor burden and profound CSC tumor localization made by the MSN-HA-siTWIST *in vivo* cannot be ignored (Figure 5 and 7). Thus, this work validates si419H's increased efficacy both *in vitro* and *in vivo* via the utilization of MSN-HA-siTWIST. Moreover, fluorescence microscopy demonstrated proper localization of MSN-HAs in the lysosomes of Ovcar8-IP-eGFP cells (Figure 3B), and provided efficacious silencing of TWIST within 24 hours and complete absence of expression within one week (Figure 3D), leading to significant chemosensitivity (Figure 3C) *in vitro*. These findings strongly support our assertion that TWIST is an important therapeutic target in ovarian cancer.

3.5 Conclusion

The great benefit of our system is safety and high specificity. The MSN-HA + siRNA only localize to tumor sites and not to other tissues or organs, and do so at a significantly greater rate than MSNs without HA. We have demonstrated that that PEI coating on the nanoparticle facilitates MSN uptake into tumor cells.[48] We suggest the possibility that

tumor associated macrophages are moderately responsible for the MSN-HA tumor targeting and efficacy we have seen here and previously, however further research is needed to determine this stance. By conducting treatments both IV and IP, we were able to conclude no significant difference in effective therapy outcome (Figure 5D); thus, supporting the IP route of administration in current human trials and its model for effective TWIST targeting. TWIST is an embryonic protien and is silenced in adult tissues, limiting on-target, off-tumor effects of the siRNA strategy, making IP injection of MSN-HA-siTWIST an advantageous therapy. Furthermore, this work supports previous research that MSNs are safe and non-toxic at the concentrations utilized in this experiment.[19,49,50] Examination of most intraperitoneal organs at necropsy (uterus, heart, lung, spleen, liver, or kidney) revealed no harm to the specimens, as supported and reviewed by a certified veterinary pathologist. However, more work needs to be done on the possible side effects caused by the siRNA, if any.

The future for these MSN-HAs is bright due to their significantly improved tumor targeting and uptake compared to MSN alone, and their mesoporous nature as likened to other metal based nanoparticles, such as gold or carbon. Additional work will exploit the MSN pore structure by examining the potential to create nanovalves on the MSNs themselves that could potentially encompass an open/close function so anticancer drugs can be stored in the pores. Other work has shown the possibility for chemo drugs to be released when MSNs encounter a low pH or an external provocation such as an oscillating magnetic field.[51–56]

Overall, this project serves to demonstrate that MSN-HAs can also be modified with targeting moieties such as hyaluronic acid (HA). Since HA is a native ligand for CD44,

which is overexpressed and correlates with worse prognosis in EOC,[57,58] we showed here enhanced uptake into tumors, especially in primary tumors, which in previous work showed limited siRNA uptake *in vivo*.[22] Thus, an MSN-HA-siRNA approach can deliver a substantial advantage in an EOC model, and paves the way for future developments of IP therapy delivery for ovarian cancer. Future work will continue to build upon our previous work in order to study multifunctional MSNs, combining chemo drug delivery, in various cancer models.

3.6 Figures

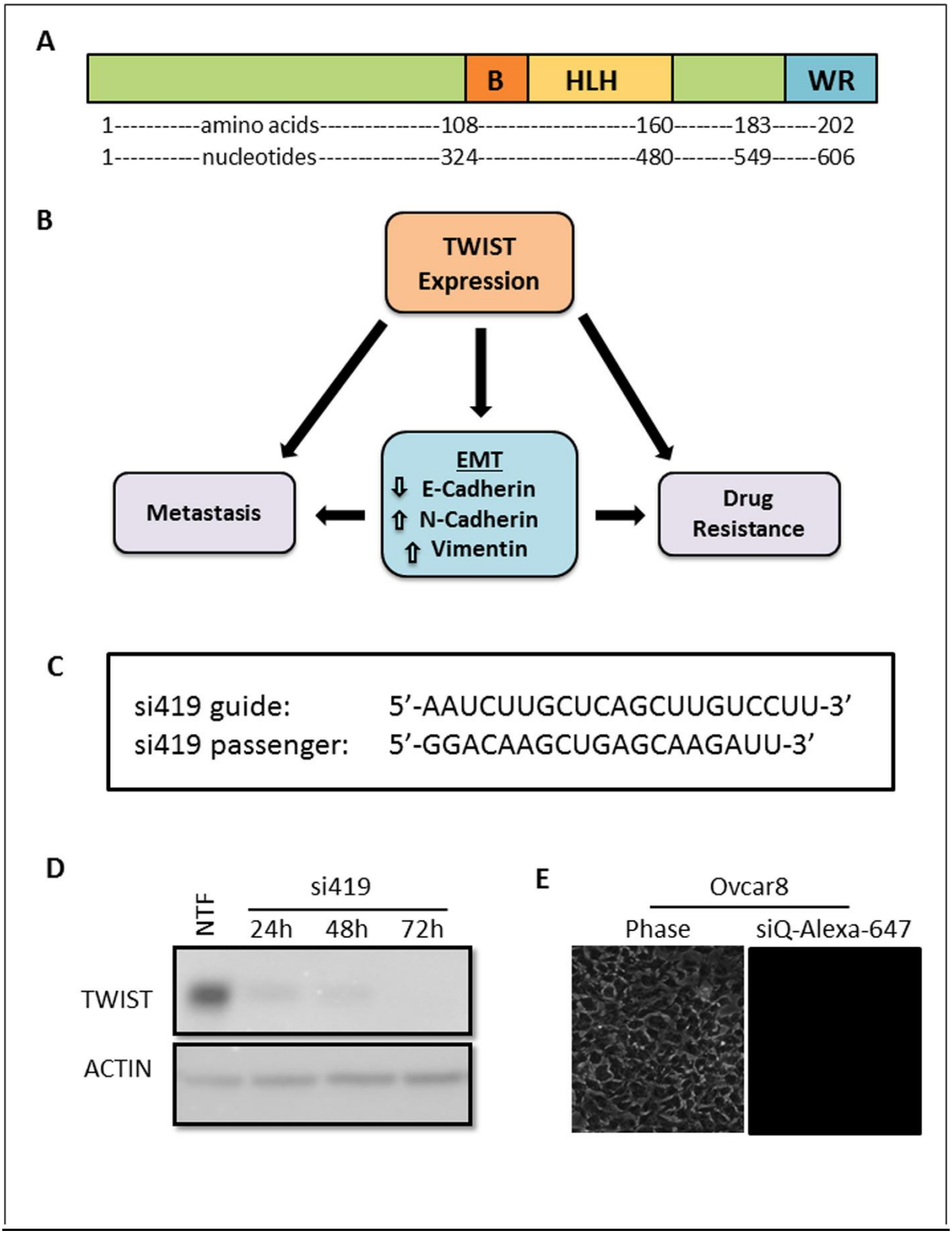
A
B
HLH
WR
1----------amino acids----------108----------160-------183-----202
1----------nucleotides----------324----------480-------549-----606
TWIST Expression
EMT
⇩ E-Cadherin
⇧ N-Cadherin
⇧ Vimentin
Metastasis
Drug Resistance
C
si419 guide: 5'-AAUCUUGCUCAGCUUGUCCUU-3'
si419 passenger: 5'-GGACAAGCUGAGCAAGAUU-3'
D
si419
NTF
24h
48h
72h
TWIST
ACTIN
E
Ovcar8
Phase
siQ-Alexa-647

Figure 1. A. TWIST schematic showing the basic DNA binding domain, helix-loop-helix dimerization motif, and C-terminal protein-binding WR domain. **B.** Reactivation of TWIST in cancers induces an epithelial to mesenchymal transition (EMT), which has been shown to lead to metastasis and acquired drug resistance. **C.** Sequences of TWIST siRNA (si419) targeting the coding region of TWIST mRNA. **D.** Validation of siRNA. Lipofectamine 2000 was used to transfect Ovcar8 cells with si419. Western blot reveals robust TWIST knockdown over three days post transfection. Non-transfection (NTF) is shown as a positive control for knockdown. **E.** Without a carrier, no siRNA enters target cells.

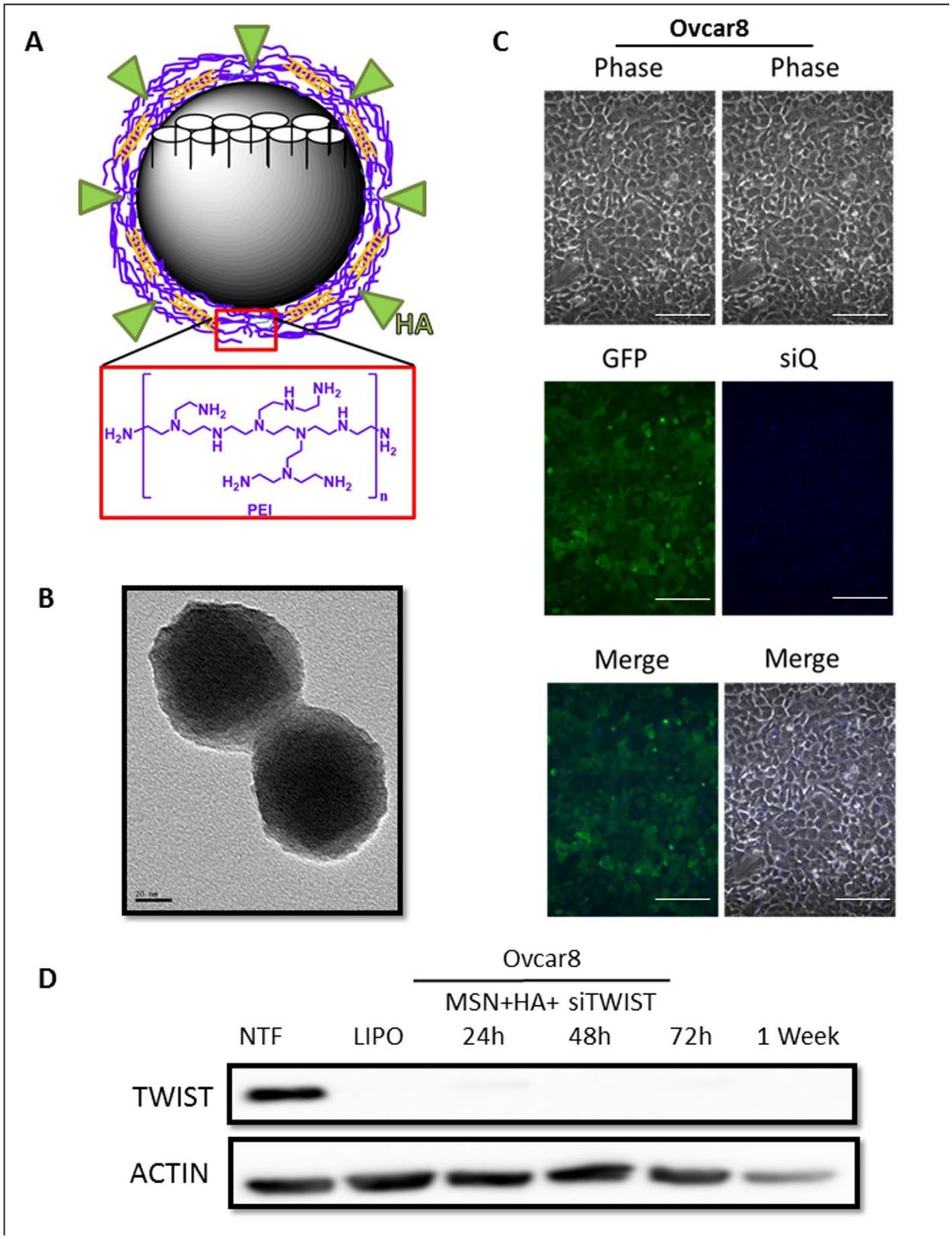
A
HA
PEI
B
C
Ovcar8
Phase
Phase
GFP
siQ
Merge
Merge
D
Ovcar8
MSN+HA+ siTWIST
NTF
LIPO
24h
48h
72h
1 Week
TWIST
ACTIN

Figure 2. A. Schematic of an MSN-HA with pore structure (white). MSN-HAs used in these studies have a PEI coating (purple layer) which allow for a balance of charge interactions to chemically bind siRNA (orange) and hyaluronic acid (HA) (green). Monomer structure for PEI is shown below (red box). **B.** Transmission electron micrograph of MSN-HAs. Particles are of uniform diameter, ~120 nm. **C.** Ovcar8-IP eGFP ffluc cells efficiently take up MSN-HAs loaded with siQ-AlexaFluor-647. Scale bar, 100 µm. **D.** si419 loaded onto MSN-HAs produce highly efficient TWIST knockdown as early as 24 hours and lasting one week post transfection. NTF and Lipofectamine were used as negative and positive controls, respectively.

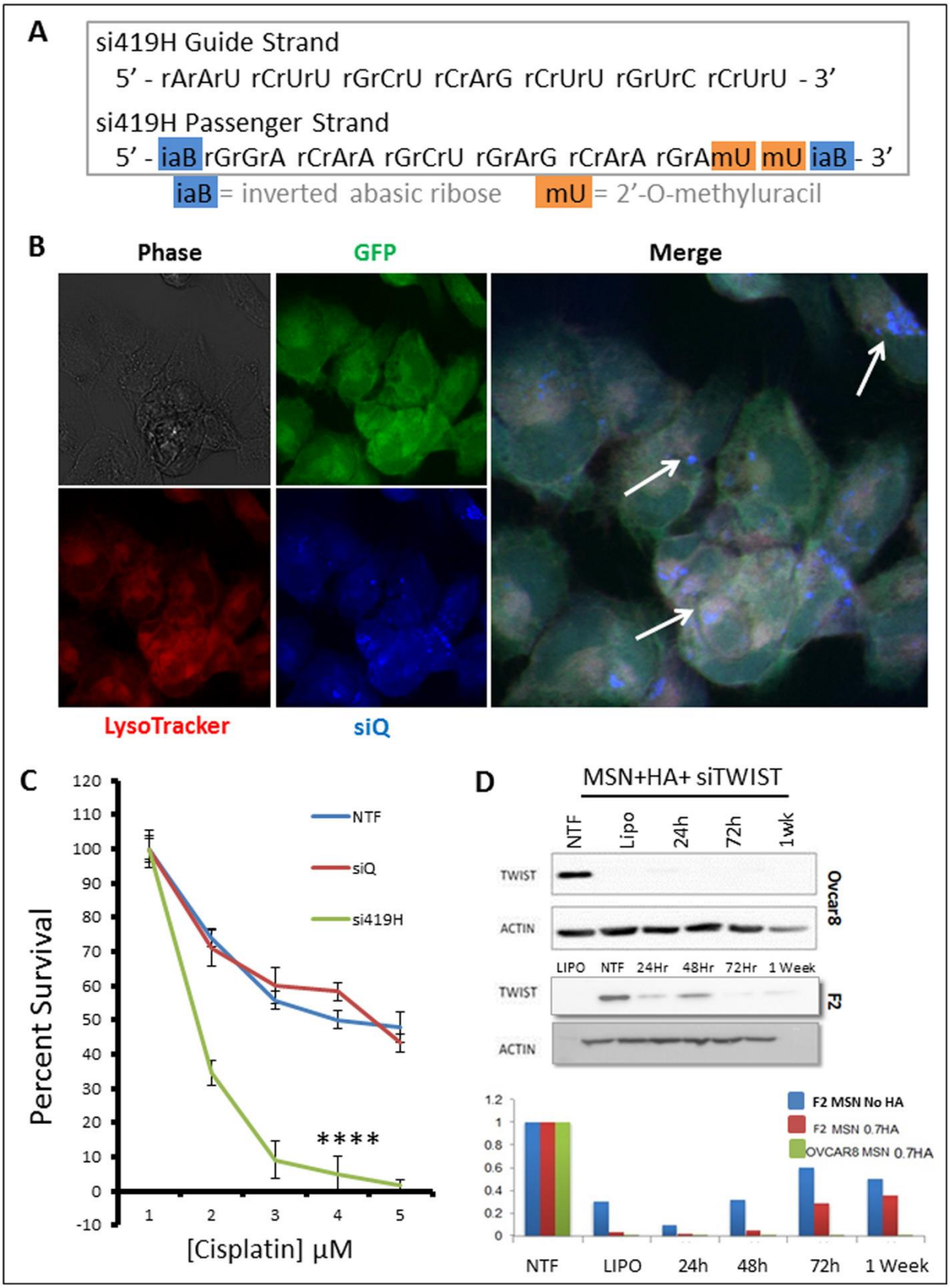
A
si419H Guide Strand
5' - rArArU rCrUrU rGrCrU rCrArG rCrUrU rGrUrC rCrUrU - 3'
si419H Passenger Strand
5' - iaB rGrGrA rCrArA rGrCrU rGrArG rCrArA rGrAmU mU iaB - 3'
iaB = inverted abasic ribose
mU = 2'-O-methyluracil
B
Phase
GFP
Merge
LysoTracker
siQ
C
Percent Survival
[Cisplatin] µM
NTF
siQ
si419H
****
D
MSN+HA+ siTWIST
NTF
Lipo
24h
72h
1wk
TWIST
ACTIN
Ovcar8
LIPO
NTF
24Hr
48Hr
72Hr
1 Week
TWIST
ACTIN
F2
F2 MSN No HA
F2 MSN 0.7HA
OVCAR8 MSN 0.7HA
NTF
LIPO
24h
48h
72h
1 Week

Figure 3. A. In preparation for *in vivo* studies, si419 was chemically modified to include 2'-O-methyluracil and inverted abasic ribose caps on the passenger strand. This siRNA is termed si419H. **B.** Confocal microscopy demonstrates MSN-HA delivery of si419H into Ovcar8-IP cells. siQ-AlexaFluor-647 (blue) colocalizes with lysosomes and late endosomes, as stained by LysoTracker (red), reflecting proper endosomal trafficking of MSN-HAs to allow siRNA release. **C.** SRB cell survival assay reveals that TWIST knockdown via MSN-HAs significantly sensitizes Ovcar8-IP cells to cisplatin (*P*=.00018). **D.** Western blot confirms that si419H knocks down TWIST in Ovcar8-IP cells and F2 cells. Knockdown is still effective one week post treatment. Comparison of MSNs alone vs MSN-HAs reveals greater knockdown efficacy when using MSN-HAs (0.7 gr HA per 10 mg MSN-PEI).

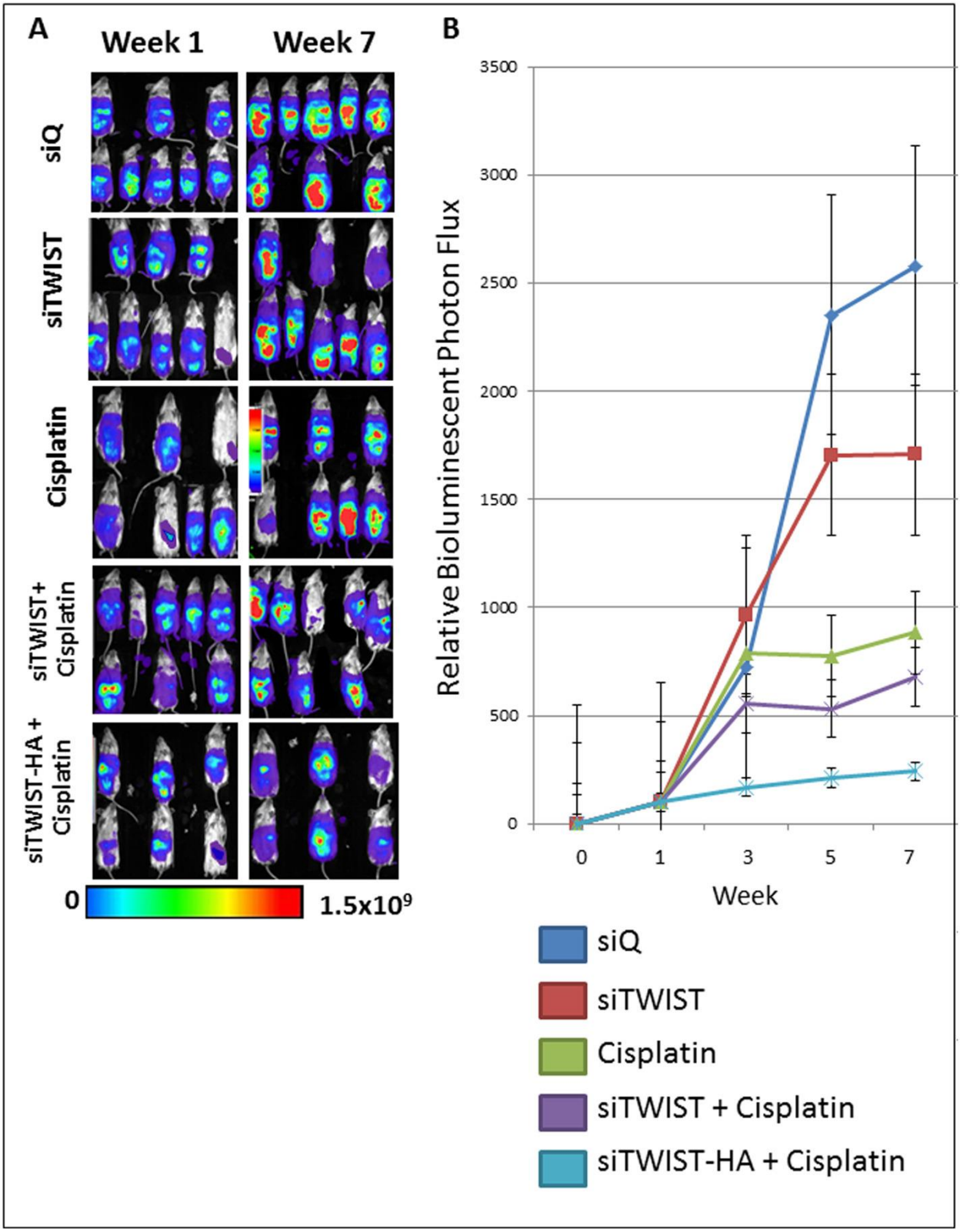
A
Week 1
Week 7
siQ
siTWIST
Cisplatin
siTWIST+ Cisplatin
siTWIST-HA + Cisplatin
0
1.5x10⁹
B
Relative Bioluminescent Photon Flux
3500
3000
2500
2000
1500
1000
500
0
0
1
3
5
7
Week
siQ
siTWIST
Cisplatin
siTWIST + Cisplatin
siTWIST-HA + Cisplatin

Figure 4. A. Bioluminescence imaging of Ovcar8-IP tumors. Tumors treated with cisplatin emit noticeably weaker signal than siTWIST or siQ only control mice, while those treated with siTWIST-MSNs plus cisplatin exhibit a further loss of signal. siTWIST-MSN-HAs plus cisplatin exhibit a greatest loss of signal. **B**. Quantification of bioluminescence for all seven weeks of treatment as depicted in A for weeks 1 and 7. Units for luminescence are photons/sec/cm2/steradian.

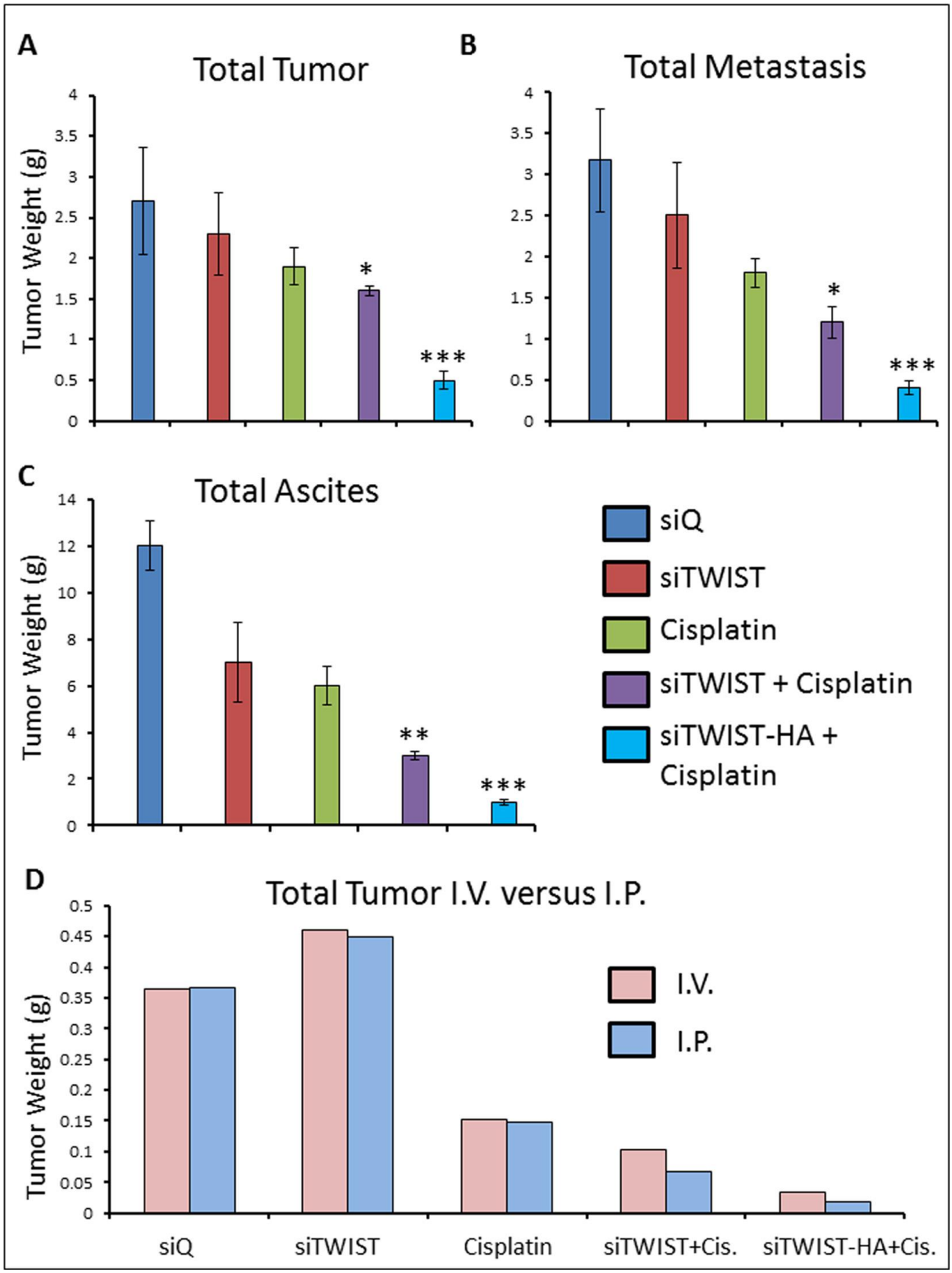
A
Total Tumor
Tumor Weight (g)
4
3.5
3
2.5
2
1.5
1
0.5
0
*
***
B
Total Metastasis
4
3.5
3
2.5
2
1.5
1
0.5
0
*
***
C
Total Ascites
Tumor Weight (g)
14
12
10
8
6
4
2
0
**
***
siQ
siTWIST
Cisplatin
siTWIST + Cisplatin
siTWIST-HA + Cisplatin
D
Total Tumor I.V. versus I.P.
Tumor Weight (g)
0.5
0.45
0.4
0.35
0.3
0.25
0.2
0.15
0.1
0.05
0
I.V.
I.P.
siQ
siTWIST
Cisplatin
siTWIST+Cis.
siTWIST-HA+Cis.

Figure 5. A. Quantification of total tumor observed in mice. Combination of cisplatin with siTWIST-MSNs reduced tumor burden 20% in comparison to cisplatin alone (*P* =0.1880); while combination of cisplatin with siTWIST-MSN-HA reduced this 75% (*P* =0.0012). **B**. Quantification of total metastasis observed. Cisplatin, with or without TWIST knockdown, produced a drop in tumor metastasis compared to controls (siQ and siTWIST). Addition of siTWIST led to a significant decrease (*P*=0.0084) when compared to cisplatin alone; while combination of cisplatin with siTWIST-MSN-HA reduced this even more (*P* =0.0011). **C**. Quantification of total ascites collected. Cisplatin, with or without TWIST knockdown, produced a drop in ascites comparing to siQ control. Addition of siTWIST led to a significant decrease (*P*=0.0072) when compared to cisplatin alone; while combination of cisplatin with siTWIST-MSN-HA reduced this even more (*P* =0.002). **D**. Quantification of total tumor in grams observed in mice that received therapy via intravenous (IV) versus intraperitoneal (I.P) injection. Results for both delivery vehicles are comparable.

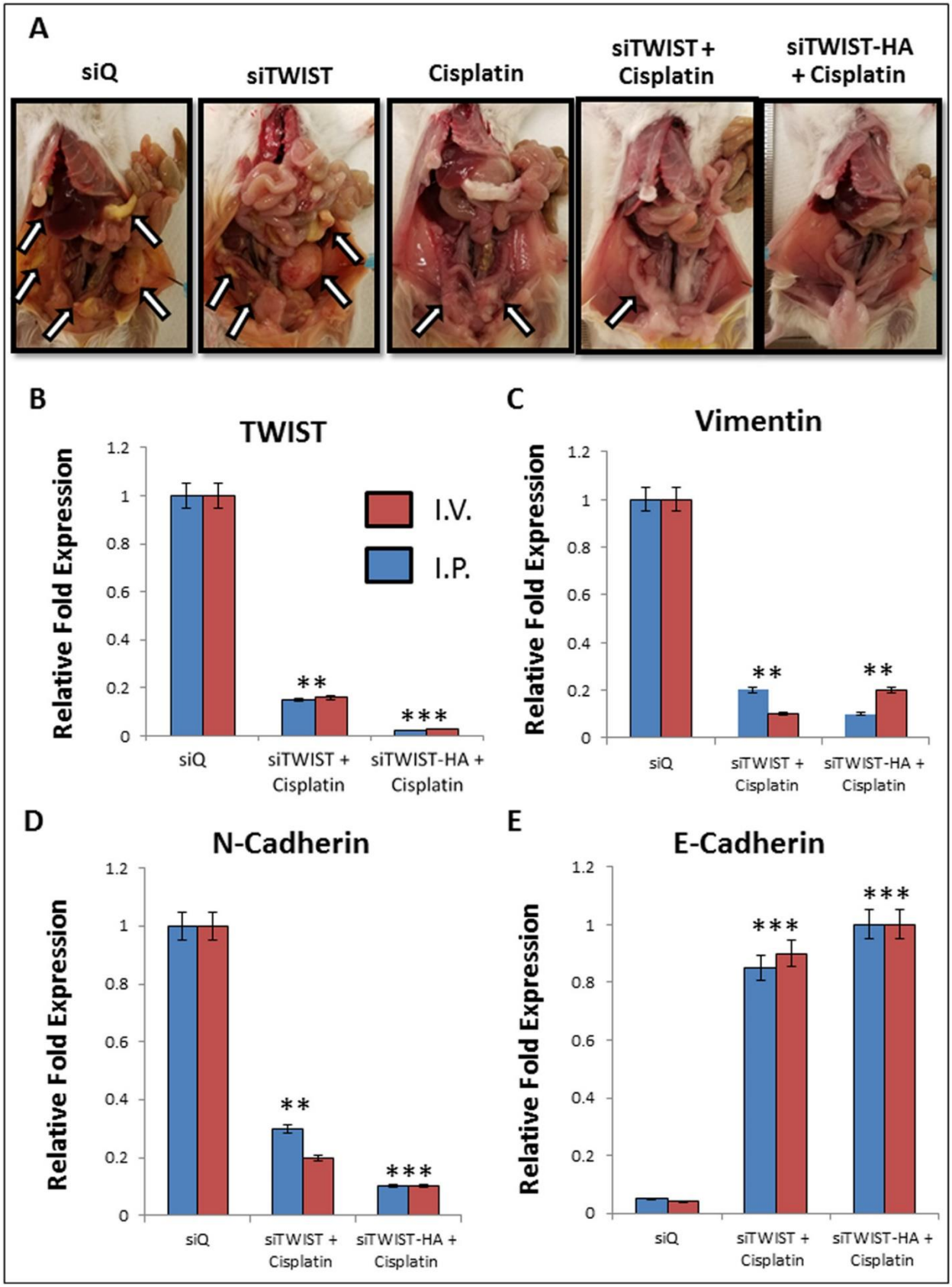
A
siQ
siTWIST
Cisplatin
siTWIST + Cisplatin
siTWIST-HA + Cisplatin
B
TWIST
Relative Fold Expression
I.V.
I.P.
**
***
siQ
siTWIST + Cisplatin
siTWIST-HA + Cisplatin
C
Vimentin
Relative Fold Expression
**
**
siQ
siTWIST + Cisplatin
siTWIST-HA + Cisplatin
D
N-Cadherin
Relative Fold Expression
**
***
siQ
siTWIST + Cisplatin
siTWIST-HA + Cisplatin
E
E-Cadherin
Relative Fold Expression
***
***
siQ
siTWIST + Cisplatin
siTWIST-HA + Cisplatin

Figure 6. A. Mice treated with siQ only have greater tumor burden than TWIST knockdown mice. Cisplatin and siTWIST treatment eliminated much of the tumor mass as compared to cisplatin alone, but a combination of cisplatin and siTWIST-MSN-HA knockdown yielded the cleanest peritoneal cavity at the conclusion of the experiment. Arrows indicate tumor foci. One representative image shown per group (siQ, siTWIST and cisplatin n=8; siTWIST and siTWIST-HA n=12). **B.–E.** qPCR results from tumors collected at necropsy. Tumors exhibit loss of TWIST1 (B) and its target genes Vimentin (C) and N-Cadherin (D). In each case, slighty greater knockdown is observed for siTWIST-MSN-HA than siTWIST-MSN alone. E-Cadherin conversely is increased with loss of TWIST (E).

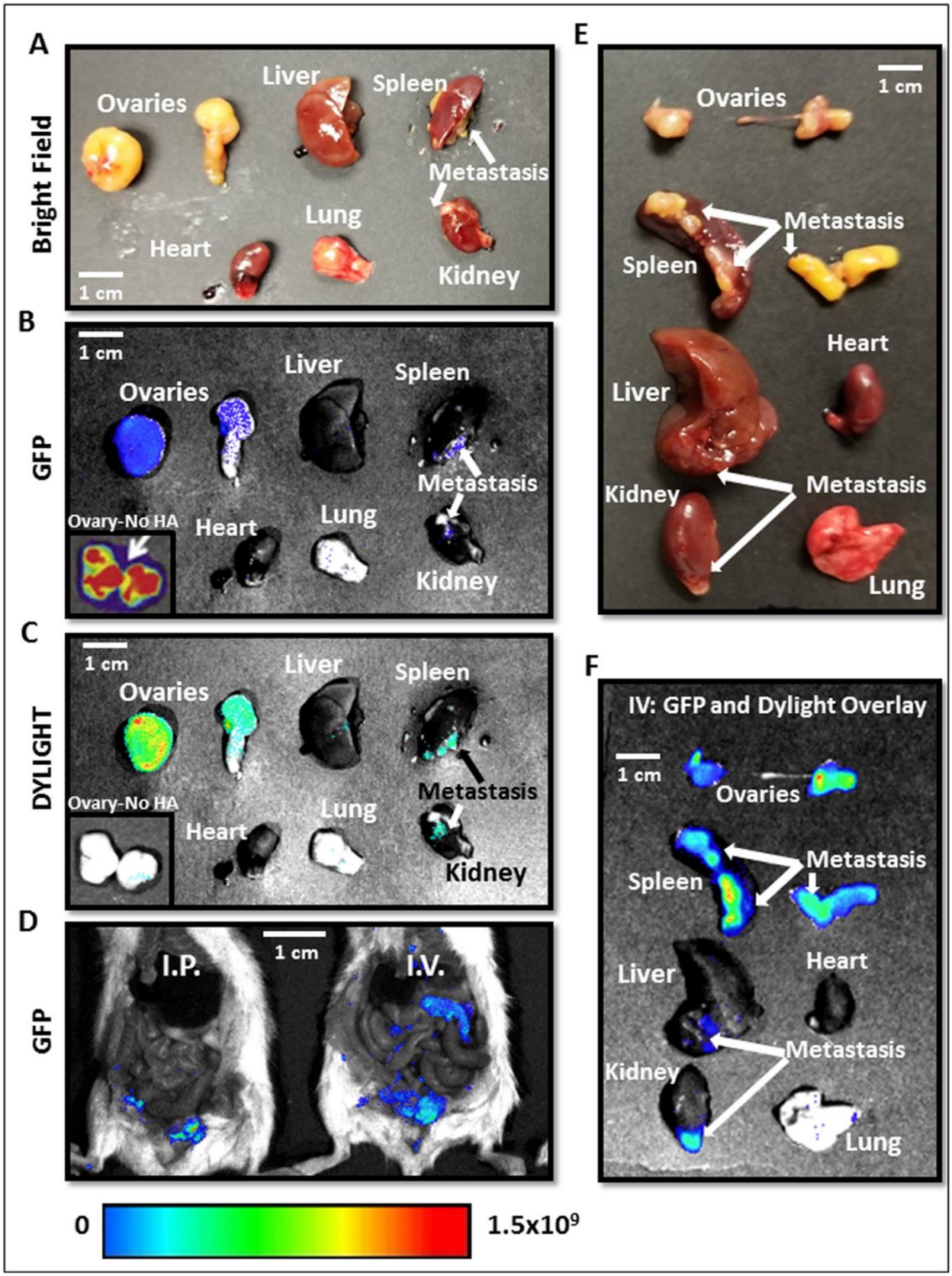
A
Bright Field
Ovaries
Liver
Spleen
Metastasis
Lung
Heart
Kidney
1 cm
B
GFP
1 cm
Ovaries
Liver
Spleen
Metastasis
Ovary-No HA
Heart
Lung
Kidney
C
DYLIGHT
1 cm
Ovaries
Liver
Spleen
Metastasis
Ovary-No HA
Heart
Lung
Kidney
D
GFP
I.P.
1 cm
I.V.
0
1.5x10⁹
E
1 cm
Ovaries
Metastasis
Spleen
Heart
Liver
Kidney
Metastasis
Lung
F
IV: GFP and Dylight Overlay
1 cm
Ovaries
Metastasis
Spleen
Liver
Heart
Metastasis
Kidney
Lung

Figure 7. A.-D. Necropsy images of mice and organs treated with MSN-HA Dylight 680 on consecutive days reveal highly specific tumor localization of siTWIST-MSN-HA complexes as compared to siTWIST-MSN (No HA) alone (C). GFP fluorescence shows all Ovcar8-IP tumor cells within the abdominal cavity (B and D). **E.-F.** Imaging of individual organs reveals that negligible quantities of MSN-HAs are found in the heart, liver, kidney, spleen, or lung. GFP and Diylight fluorescence is nearly all found in disseminated tumors, including lesions on the liver, kidney and spleen surfaces, with most signal emitted from the primary tumor. Units for luminescence are photons/sec/cm^2/steradian.

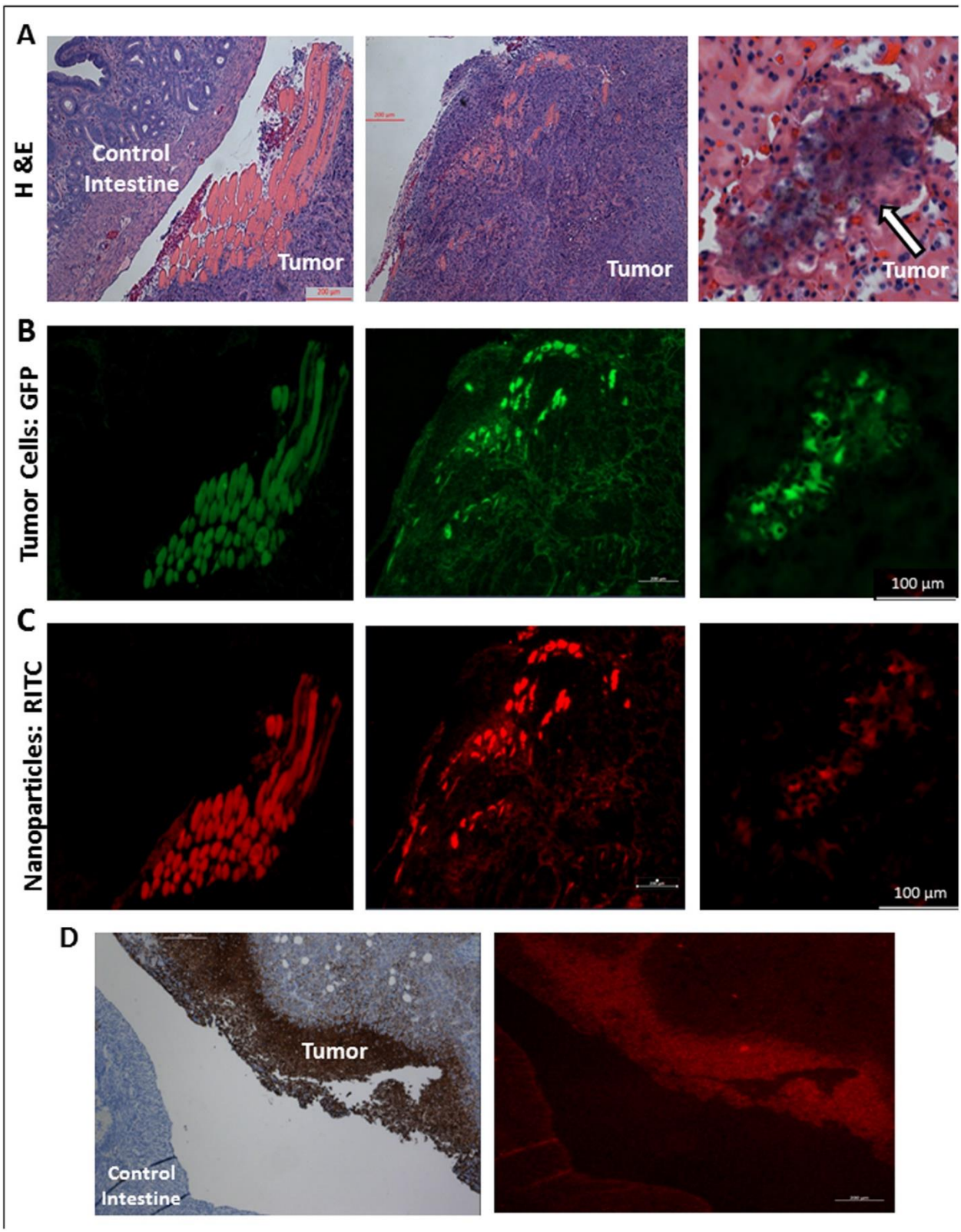
A
H &E
Control
Intestine
Tumor
Tumor
Tumor
B
Tumor Cells: GFP
100 µm
C
Nanoparticles: RITC
100 µm
D
Tumor
Control
Intestine

Figure 8. A. Mouse tumor tissue sections stained with hematoxylin and eosin (H&E) stain after necropsy reveal significant tumor burden. **B.** GFP fluorescence reveals tumor cell location. **C.** RITC fluorescence reveals highly specific nanoparticle tumor targeting; MSN-HA nanoparticles are only localized in tumor cells and not in control intestine. **D.** MSN-HA co-localizes with CD44 on the membrane of tumor.

3.7 References

1. Siegel, R. L., Miller, K. D. & Jemal, A. Cancer statistics, 2016. CA. Cancer J. Clin. 66, 7–30 (2016).
2. Markman, M. et al. Duration of Response to Second-Line, Platinum-Based Chemotherapy for Ovarian Cancer: Implications for Patient Management and Clinical Trial Design. J. Clin. Oncol. 22, 3120–3125 (2004).
3. Chang, S.-J., Hodeib, M., Chang, J. & Bristow, R. E. Survival impact of complete cytoreduction to no gross residual disease for advanced-stage ovarian cancer: A meta-analysis. Gynecol. Oncol. 130, 493–498 (2013).
4. Coleman, R. L., Monk, B. J., Sood, A. K. & Herzog, T. J. Latest research and treatment of advanced-stage epithelial ovarian cancer. Nat. Rev. Clin. Oncol. 10, 211–224 (2013).
5. Aghajanian, C. et al. Final overall survival and safety analysis of OCEANS, a phase 3 trial of chemotherapy with or without bevacizumab in patients with platinum-sensitive recurrent ovarian cancer. Gynecol. Oncol. 139, 10–16 (2015).
6. Ushijima, K. Treatment for Recurrent Ovarian Cancer—At First Relapse. J. Oncol. 2010, 497429 (2010).
7. Beck, B. & Blanpain, C. Unravelling cancer stem cell potential. Nat. Rev. Cancer 13, 727–738 (2013).
8. Daley, G. Q. Common Themes of Dedifferentiation in Somatic Cell Reprogramming and Cancer. Cold Spring Harb. Symp. Quant. Biol. 73, 171–174 (2008).

9. Abdullah, L. N. & Chow, E. K.-H. Mechanisms of chemoresistance in cancer stem cells. Clin. Transl. Med. 2, 3 (2013).

10. Cornelison, R., Llaneza, D. C. & Landen, C. N. Emerging therapeutics to overcome chemoresistance in epithelial ovarian cancer: A mini-review. Int. J. Mol. Sci. 18, 1–20 (2017).

11. Terauchi, M. et al. Possible involvement of TWIST in enhanced peritoneal metastasis of epithelial ovarian carcinoma. Clin. Exp. Metastasis 24, 329–339 (2007).

12. Yang, J. et al. Twist, a Master Regulator of Morphogenesis, Plays an Essential Role in Tumor Metastasis. Cell 117, 927–939 (2004).

13. Yin, G. et al. Constitutive proteasomal degradation of TWIST-1 in epithelial–ovarian cancer stem cells impacts differentiation and metastatic potential. Oncogene 32, 39–49 (2013).

14. Gort, E. H. et al. Methylation of the TWIST1 Promoter, TWIST1 mRNA Levels, and Immunohistochemical Expression of TWIST1 in Breast Cancer. Cancer Epidemiol. Biomarkers Prev. 17, 3325–3330 (2008).

15. Vesuna, F., Lisok, A., Kimble, B. & Raman, V. Twist Modulates Breast Cancer Stem Cells by Transcriptional Regulation of CD24 Expression. Neoplasia 11, 1318–1328 (2009).

16. Yin, G. et al. TWISTing stemness, inflammation and proliferation of epithelial ovarian cancer cells through MIR199A2/214. Oncogene 29, 3545–3553 (2010).

17. Ahmed, N., Abubaker, K., Findlay, J. & Quinn, M. Epithelial Mesenchymal Transition and Cancer Stem Cell-Like Phenotypes Facilitate Chemoresistance in

Recurrent Ovarian Cancer. Curr. Cancer Drug Targets 10, 268–278 (2010).

18. Li, S. et al. TWIST1 associates with NF-κB subunit RELA via carboxyl-terminal WR domain to promote cell autonomous invasion through IL8 production. BMC Biol. 10, 73 (2012).

19. Finlay, J. et al. Mesoporous silica nanoparticle delivery of chemically modified siRNA against TWIST1 leads to reduced tumor burden. Nanomedicine Nanotechnology, Biol. Med. 11, 1657–1666 (2015).

20. Finlay, J. et al. RNA-Based TWIST1 Inhibition via Dendrimer Complex to Reduce Breast Cancer Cell Metastasis. Biomed Res. Int. 2015, 382745 (2015).

21. Bobbin, M. L. & Rossi, J. J. RNA Interference (RNAi)-Based Therapeutics: Delivering on the Promise? Annu. Rev. Pharmacol. Toxicol. 56, 103–122 (2016).

22. Roberts, C. M. et al. Nanoparticle delivery of siRNA against TWIST to reduce drug resistance and tumor growth in ovarian cancer models. Nanomedicine Nanotechnology, Biol. Med. 13, 965–976 (2017).

23. Hom, C. et al. Mesoporous Silica Nanoparticles Facilitate Delivery of siRNA to Shutdown Signaling Pathways in Mammalian Cells. Small 6, 1185–1190 (2010).

24. Hoppenot, C., Eckert, M. A., Tienda, S. M. & Lengyel, E. Who are the long-term survivors of high grade serous ovarian cancer? Gynecol. Oncol. 148, 204–212 (2018).

25. Li, B., Li, Q., Mo, J. & Dai, H. Drug-Loaded Polymeric Nanoparticles for Cancer Stem Cell Targeting. Front. Pharmacol. 8, 51 (2017).

26. Brown, C. E. et al. Recognition and Killing of Brain Tumor Stem-Like Initiating Cells by CD8+ Cytolytic T Cells. Cancer Res. 69, 8886–8893 (2009).

27. Meng, H. et al. Use of Size and a Copolymer Design Feature To Improve the Biodistribution and the Enhanced Permeability and Retention Effect of Doxorubicin-Loaded Mesoporous Silica Nanoparticles in a Murine Xenograft Tumor Model. ACS Nano 5, 4131–4144 (2011).
28. Qin, W., Huang, G., Chen, Z. & Zhang, Y. Nanomaterials in Targeting Cancer Stem Cells for Cancer Therapy. Front. Pharmacol. 8, 1 (2017).
29. Mattheolabakis, G., Milane, L., Singh, A. & Amiji, M. M. Hyaluronic acid targeting of CD44 for cancer therapy: From receptor biology to nanomedicine. J. Drug Target. 23, 605–618 (2015).
30. Behlke, M. A. Chemical modification of siRNAs for *in vivo* use. Oligonucleotides 18, 305–319 (2008).
31. Czauderna, F. et al. Structural variations and stabilising modifications of synthetic siRNAs in mammalian cells. Nucleic Acids Res. 31, 2705–2716 (2003).
32. Roberts, C. M. et al. Disruption of TWIST1-RELA binding by mutation and competitive inhibition to validate the TWIST1 WR domain as a therapeutic target. BMC Cancer 17, 184 (2017).
33. Mani, S. A. et al. The Epithelial-Mesenchymal Transition Generates Cells with Properties of Stem Cells. Cell 133, 704–715 (2008).
34. Thiery, J. P. & Sleeman, J. P. Complex networks orchestrate epithelial–mesenchymal transitions. Nat. Rev. Mol. Cell Biol. 7, 131–142 (2006).
35. Lu, H. et al. A breast cancer stem cell niche supported by juxtacrine signalling from monocytes and macrophages. Nat. Cell Biol. 16, 1105–1117 (2014).
36. Ye, X. et al. Distinct EMT programs control normal mammary stem cells and

tumour-initiating cells. Nature 525, 256–260 (2015).

37. Ye, X. & Weinberg, R. A. Epithelial–Mesenchymal Plasticity: A Central Regulator of Cancer Progression. Trends Cell Biol. 25, 675–686 (2015).

38. Fabregat, I., Malfettone, A. & Soukupova, J. New Insights into the Crossroads between EMT and Stemness in the Context of Cancer. J. Clin. Med. 5, 37 (2016).

39. Wang, X. et al. Identification of a novel function of TWIST, a bHLH protein, in the development of acquired taxol resistance in human cancer cells. Oncogene 23, 474–482 (2004).

40. Brozovic, A. The relationship between platinum drug resistance and epithelial–mesenchymal transition. Arch. Toxicol. 91, 605–619 (2017).

41. Brozovic, A., Duran, G. E., Wang, Y. C., Francisco, E. B. & Sikic, B. I. The miR-200 family differentially regulates sensitivity to paclitaxel and carboplatin in human ovarian carcinoma OVCAR-3 and MES-OV cells. Mol. Oncol. 9, 1678–1693 (2015).

42. Stojanović, N. et al. Integrin αvβ3 expression in tongue squamous carcinoma cells Cal27 confers anticancer drug resistance through loss of pSrc(Y418). Biochim. Biophys. Acta - Mol. Cell Res. 1863, 1969–1978 (2016).

43. Marchetti, C., Ledermann, J. A. & Benedetti Panici, P. An overview of early investigational therapies for chemoresistant ovarian cancer. Expert Opin. Investig. Drugs 24, 1163–1183 (2015).

44. Helleman, J., Smid, M., Jansen, M. P. H. M., van der Burg, M. E. L. & Berns, E. M. J. J. Pathway analysis of gene lists associated with platinum-based chemotherapy resistance in ovarian cancer: The big picture. Gynecol. Oncol. 117,

170–176 (2010).

45. Yoshida, J. et al. Changes in the expression of E-cadherin repressors, Snail, Slug, SIP1, and Twist, in the development and progression of ovarian carcinoma: the important role of Snail in ovarian tumorigenesis and progression. Med. Mol. Morphol. 42, 82–91 (2009).

46. Zhu, D. J. et al. Twist1 is a potential prognostic marker for colorectal cancer and associated with chemoresistance. Am. J. Cancer Res. 5, 2000–2011 (2015).

47. Zhu, X. et al. miR-186 regulation of Twist1 and ovarian cancer sensitivity to cisplatin. Oncogene 35, 323–332 (2016).

48. Xia, T. et al. Polyethyleneimine Coating Enhances the Cellular Uptake of Mesoporous Silica Nanoparticles and Allows Safe Delivery of siRNA and DNA Constructs. ACS Nano 3, 3273–3286 (2009).

49. Ferris, D. P. et al. Synthesis of Biomolecule-Modified Mesoporous Silica Nanoparticles for Targeted Hydrophobic Drug Delivery to Cancer Cells. Small 7, 1816–1826 (2011).

50. Lu, J., Liong, M., Zink, J. I. & Tamanoi, F. Mesoporous Silica Nanoparticles as a Delivery System for Hydrophobic Anticancer Drugs. Small 3, 1341–1346 (2007).

51. Ambrogio, M. W., Thomas, C. R., Zhao, Y.-L., Zink, J. I. & Stoddart, J. F. Mechanized Silica Nanoparticles: A New Frontier in Theranostic Nanomedicine. Acc. Chem. Res. 44, 903–913 (2011).

52. Deng, Z. J. et al. Layer-by-Layer Nanoparticles for Systemic Codelivery of an Anticancer Drug and siRNA for Potential Triple-Negative Breast Cancer Treatment. ACS Nano 7, 9571–9584 (2013).

53. Dong, J., Xue, M. & Zink, J. I. Functioning of nanovalves on polymer coated mesoporous silica Nanoparticles. Nanoscale 5, 10300 (2013).

54. Lu, J., Li, Z., Zink, J. I. & Tamanoi, F. *In vivo* tumor suppression efficacy of mesoporous silica nanoparticles-based drug-delivery system: enhanced efficacy by folate modification. Nanomedicine Nanotechnology, Biol. Med. 8, 212–220 (2012).

55. Tarn, D., Xue, M. & Zink, J. I. pH-Responsive Dual Cargo Delivery from Mesoporous Silica Nanoparticles with a Metal-Latched Nanogate. Inorg. Chem. 52, 2044–2049 (2013).

56. Thomas, C. R. et al. Noninvasive Remote-Controlled Release of Drug Molecules *in Vitro* Using Magnetic Actuation of Mechanized Nanoparticles. J. Am. Chem. Soc. 132, 10623–10625 (2010).

57. Elzarkaa, A. A. et al. Clinical relevance of CD44 surface expression in advanced stage serous epithelial ovarian cancer: a prospective study. J. Cancer Res. Clin. Oncol. 142, 949–958 (2016).

58. Kayastha, S. et al. Expression of the hyaluronan receptor, CD44s, in epithelial ovarian cancer is an independent predictor of survival. Clin. Cancer Res. 5, 1073–1076 (1999).

Chapter 4

Nanoparticle formulation of Moxifloxacin and intramuscular route of delivery improve antibiotic pharmacokinetics and treatment of pneumonic tularemia in a mouse model

This chapter is based on work done with collaborators Daniel L. Clemens and Bai-Yu Lee, et. al. at Division of Infectious Diseases, UCLA for bio-assays and mouse model tests. This study is summarized and published as follow:

Clemens, D. L., Lee, B. Y., Plamthottam, S., Tullius, M. V., Wang, R., Yu, C. J., ... & Horwitz, M. A. (2018). Nanoparticle Formulation of Moxifloxacin and Intramuscular Route of Delivery Improve Antibiotic Pharmacokinetics and Treatment of Pneumonic Tularemia in a Mouse Model. ACS infectious diseases, 5(2), 281-291.

4.1 Abstract

Francisella tularensis causes a serious and often fatal infection, tularemia. We compared the efficacy of moxifloxacin formulated as free drug vs. disulfide snap-top mesoporous silica nanoparticles (MSNs) in a mouse model of pneumonic tularemia. We found that MSN-formulated moxifloxacin was more effective than free drug and that the intramuscular and subcutaneous routes were markedly more effective than the intravenous route. Measurement of tissue silica levels and fluorescent flow cytometry assessment of colocalization of MSNs with infected cells revealed that the enhanced efficacy of MSNs and the intramuscular route of delivery was not due to better delivery of MSNs to infected tissues or cells. However, moxifloxacin blood levels demonstrated that the nanoparticle formulation and intramuscular route provided the longest half-life and longest time above the minimal inhibitory concentration. Thus, improved pharmacokinetics are responsible for the greater efficacy of nanoparticle formulation and intramuscular delivery compared with free drug and intravenous delivery.

4.2 Introduction

Mesoporous silica nanoparticles (MSNs) are an attractive drug delivery platform for several reasons, including an extremely large internal surface area that allows high drug loading and a surface that can be readily modified for targeting of specific cells and controlled drug release in response to environmental cues.[1,2] For example, we have devised MSNs functionalized with disulfide snap-tops that release their drug cargo intracellularly in response to the intracellular redox potential.[3,4] We have previously shown

that intravenous (i.v.) administration of moxifloxacin (MXF) via disulfide snap-top redox-operated MSNs (MSN-SS-MXF) is much more effective for treatment of pneumonic tularemia in mice than an equivalent amount of free drug[3] (i.e. non-MSN encapsulated drug). However, the basis for the enhanced efficacy was not determined. Nanoparticle (NP)-delivered antibiotics have been proposed to have numerous advantages over free drugs, including shielding the drug from excretion and metabolism, improved pharmacokinetics,[5] and specific targeting of macrophages in the lung and reticuloendothelial system, which are important host cells for intracellular pathogens, such as *Francisella* tularensis[3,6] and *Mycobacterium* tuberculosis.[7] The relative contribution of various factors to the enhanced efficacy of MSN-delivered drug vs. free drug is often unclear.

A study in *Mycobacterium marinum* infected zebrafish embryos demonstrated that poly(lactic-co-glycolic acid) (PLGA) NPs administered i.v. are taken up by macrophages that traffic into *M. marinum* containing granulomas,[8] consistent with the concept that a NP platform can enhance drug delivery to infected cells and tissues. However, the study did not examine whether i.v. administration of the PLGA-delivered drug was more effective than other routes, e.g. the subcutaneous (s.c.) or intramuscular (i.m.) route, where trafficking of NP-containing drug to the site of infection might be less effective.

Here we determined the efficacy of MSN-SS-MXF delivered i.v., s.c., or i.m. against lethal respiratory infection with *F. tularensis* subsp. *holarctica* Live Vaccine Strain (LVS) in mice. We show that equivalent amounts of MXF exhibit the following order of efficacy for treatment of pneumonic tularemia in a mouse model: i.m. MSN-SS-MXF > i.v. MSN-SS-MXF > i.m. free MXF > i.v. free MXF. We conducted additional studies to determine

whether the improved efficacy of the MSN formulation and the i.m. route of administration was attributable to improved delivery to infected cells or to improved pharmacokinetics. While i.m. administered MSN-SS-MXF was the most effective, we found few or no MSNs in the lungs of mice following i.m. administration, indicating that, for this NP platform, enhanced trafficking of MSN-SS-MXF to the site of infection is not responsible for the markedly enhanced efficacy of the i.m. route. On the other hand, the nanoparticle formulation yields a longer half-life than free drug and i.m. administration yields an even further prolongation of the half-life. In our model of pneumonic tularemia, time above the minimal inhibitory concentration (t>MIC) is the best predictor of MXF efficacy, and accordingly, i.m. administration of the nanoparticle formulation of MXF was superior to all other routes and to free MXF.

4.3 Experimental

Bacteria

F. tularensis LVS was acquired from the Centers for Disease Control and Prevention (Atlanta, GA). Frozen stocks of LVS and LVS expressing green fluorescent protein (LVS-GFP) were prepared from cultures on GC II agar with hemoglobin and IsoVitaleX enrichment (BD BBL) and pre-titered for use directly in animal experiments. *F. tularensis* subsp. *novicida* (*F. novicida*) was cultivated at 37°C with aeration in trypticase soy broth (BD BBL) supplemented with 0.2% cysteine (TSBC) for use in the bioassay for MXF.

MSN-SS-MXF and DyLight 650-labeled MSN

MSN-SS-MXF were prepared as previously described.[3] Briefly, cetyltrimethylammonium bromide (CTAB, 0.7 mmol) was mixed with NaOH (2 M, 1.7 mmol) in deionized water (120 mL). The solution was maintained at 80°C during dropwise addition of tetraethylorthosilicate (TEOS, 5.4 mmol). After 15 minutes, 3-(trihydroxysilyl) propyl methylphosphonate (HTMP, 0.5 mmol) was added to the mixture. The reaction temperature was maintained at 80°C for an additional 2 hours after which the MSNs were collected by centrifugation and washed three times with water and ethanol. The MSNs were modified with thiol groups by dispersing the MSNs and (3-mercaptopropyl) trimethoxysilane in dry toluene and refluxing under nitrogen atmosphere. CTAB was removed by suspending the MSNs (200 mg) in ethanol (80 mL) with the addition of concentrated HCl (10 mL) and refluxing for 1 hour, twice. The adamantane moiety was conjugated to the MSNs through formation of a disulfide bond. Typically, 1-adamantanethiol (17 mg, 0.1 mmole) and thiol group modified MSNs (100 mg) were mixed and suspended in anhydrous toluene (10 mL). The oxidizing reagent thiolcyanogen was prepared separately by dispersing lead thiocyanate (800 mg) in 10 mL chloroform and titrating with bromine (200 µl) dissolved in chloroform (10 mL). The resultant mixture was filtered to obtain thiolcyanogen, which was slowly added to the MSN mixture at 4°C under nitrogen atmosphere. The adamantane-modified MSNs (MSN-SS-Ada) were washed thoroughly with toluene, ethanol and deionized water. MXF was loaded by suspending MSN-SS-Ada (10 mg) in 1 mL of 40 mM MXF in PBS and rotating overnight. β-cyclodextrin (40 mg) was then added to the solution as capping agent and the solution rotated for an additional 6 hours. The loaded MSNs (MSN-SS-MXF) were washed thoroughly prior to use.

Dylight 650-labeled MSNs were prepared by first mixing (3-aminopropyl) triethoxysilane (APTES, 0.2 mmol) with TEOS (4.5 mmol) and then adding the solution dropwise to the basic CTAB solution. After removal of CTAB, MSNs were suspended in DMF, and DyLight 650 NHS-Ester (500 µl) was added to allow covalent coupling to the amine groups grafted within the MSNs. After dye labeling, the particles were washed and processed as described above for disulfide snap-top modification.

Physicochemical characterization of the MSN

Transmission electron microscopy (TEM) images of MSN were obtained using a JEM1200-EX (JEOL) instrument (JEOL USA, Inc., Peabody, MA). Particle size and zeta potential were measured by ZetaSizer Nano (Malvern Instruments Ltd, Worcestershire, UK) with 50 µg/mL MSN dispersed in de-ionized water.

Measurement of MSN-SS-MXF release capacity

We used a modification of our previously described *F. novicida* bioassay[3] to determine the maximum amount of MXF released from particles. MXF released from MSN-SS-MXF in PBS or DMSO or acidified DMSO with and without 2-mercaptoethanol was measured by determining inhibition of *F. novicida* growth in TSBC.

Mouse model of pneumonic tularemia

Female BALB/c mice, age 8-9 weeks (Envigo), were acclimated for one week prior to infection with 4000 CFU (~6 x LD_{50}) of *F. tularensis* LVS i.n. Two mice were euthanized after infection (day 0) for determination of initial organ burden of *F. tularensis*. One day later (day 1), 3 additional mice were euthanized to determine the level of *F. tularensis*

immediately before the start of treatment. Mice were treated with one of three doses of free MXF in PBS (3 mice/group for each dose) or one of two doses of MSN-SS-MXF (4 mice/group) i.v., s.c., or i.m. every other day (day 1, 3, and 5 for a total of three treatments). Sham-treated mice (3 mice/group) received an equal volume of PBS i.v. every other day on the same schedule. The mice were euthanized one day (day 6) after their third treatment, the organs harvested (lung, liver, and spleen), and the number of CFU determined by plating serial dilutions of organ homogenates on GCII chocolate agar plates containing sulfamethoxazole (40 μg/mL), trimethoprim (8 μg/mL), and erythromycin (50 μg/mL) to prevent growth of contaminants. Bacterial colonies were counted after incubation at 37°C for 4 days. All animal studies were approved by and conducted according to the procedures set forth by the UCLA Animal Research Committee (ARC # 1998-140).

Biodistribution of MSN-SS-MXF

BALB/c mice were fed a low silica diet and water throughout the experiment to optimize measurement of silica in organs. The mice were infected with *F. tularensis* LVS i.n. and administered either PBS i.v. or 0.28 mg MSN-SS-MXF i.v., s.c., or i.m. (4 mice/route) every other day for a total of 3 treatments, and euthanized 24 h later, as described above. Their organs were harvested, homogenized in PBS, digested with 67 - 70% HNO_3, evaporated, and reconstituted in a defined volume of 3-5 v/v% HNO_3 solution for analysis by ICP-OES (ICPE-9000, SHIMADZU, Japan).

Flow cytometry

BALB/c mice were acclimated for one week and infected with 4000 CFU LVS-GFP i.n. or left uninfected (negative control). Two days later, the infected mice were injected i.v. or i.m. with 1 mg of DyLight 650-labeled MSN or left untreated. Three days after infection with LVS-GFP, ~24 h after injection with DyLight 650-labeled MSNs, the mice were euthanized and their spleens and lungs harvested for analysis.

Single-cell suspensions of splenocytes were prepared by gently pressing the cells out of the spleen sac, lysing red blood cells with PharmLyse (BD Pharmingen), washing the cells, and filtering them through a 70-µm nylon cell strainer (Falcon). Single-cell suspensions of total lung cells were prepared by quickly chopping the lungs into small pieces with a scalpel and digesting for 1 h in 10 mL PBS containing 300 U/mL Collagenase type II (Worthington) and 0.15 mg/mL DNase I (Worthington) at 37°C with shaking (300 rpm). The lung cells were filtered through a 40-µm nylon cell strainer (Falcon), red blood cells lysed with PharmLyse, and the lung cells washed. Advanced RPMI 1640 (Invitrogen), supplemented with 2% heat-inactivated fetal bovine serum, 2 mM l-alanyl-l-glutamine (Glutamax; Invitrogen), 10 mM HEPES buffer, 50 µM β-mercaptoethanol, and penicillin (100 IU/mL)-streptomycin (100 µg/mL), was used as the medium. Surface staining was performed in a 96-well V-bottom plate kept on ice. Lung and spleen cells (2 to 4 x 10^6 cells per well) were blocked with 4 µg anti-mouse CD16/32 (TruStain fcX, BioLegend), stained with 0.2 µg PE-labeled anti-mouse F4/80 (1:100 dilution) (BioLegend), washed, and fixed in 1% formaldehyde in PBS. Fixed cells were analyzed on an ImageStream Mark II Imaging Flow Cytometer and 30,000 events at 60x magnification were recorded for each sample gated by focus and aspect ratio vs. area parameters to obtain predominantly single cells. High quality single-cell images were

obtained by gating events post acquisition with IDEAS® software version 4.0 (Amnis) using focus, aspect ratio vs. area, circularity, perimeter, diameter, and contrast parameters. This further refinement resulted in ~10,000 to 14,000 images for samples of lung cells and ~19,000 to 21,000 images for samples of spleen cells. Images with internalized LVS-GFP or internalized DyLight 650-labeled MSN were identified using intensity, max pixel, and internalization parameters. Samples from uninfected and/or untreated (i.e. not injected with MSN) mice were used as negative controls to determine where to draw the selection gates. Cells positive for F4/80 surface staining were gated using a side scatter vs. intensity plot; an unstained control was used to determine the location of the selection gate.

Drug dose-effect plots

The fraction of inhibition for samples treated with different doses of MXF was calculated using bacterial CFU in base-10 logarithm (log CFU) with the equation: Fraction of inhibition = 1 – (log CFU from sample treated with a known concentration of MXF or releasable MXF from MSN-SS-MXF/log CFU from untreated sample). A median-effect plot[9,10] for MXF or MSN-SS-MXF was generated using MXF or MXF-equivalent (MSN) dose in base-10 logarithm as the X-axis and the fraction of surviving/killed bacteria in base-10 logarithm as the Y-axis.

Determination of MXF blood levels by LC-MS

MXF blood concentrations were determined by a modification of published methods.[11,12] Heparinized blood (0.1 mL) was collected by retro-orbital bleed at sequential times after administration of free MXF or MSN-SS-MXF i.v. or i.m. Ciprofloxacin (75 ng) was added

to each sample as an internal standard and 9 volumes (0.9 mL) of acetonitrile were added and mixed thoroughly. The sample was stored overnight at 4°C, mixed again by vortex action, and insoluble material pelleted by centrifugation at 10,000*g* for 10 minutes. The supernatant was transferred to a new tube and dried under vacuum. The dried material was resolubilized in 50 µl water and MXF was quantified by reverse-phase C18-LC-MS**.** LC analysis was performed on a Waters LCT Premier (TOF) Mass Spectrometer (positive electrospray ionization mode) with Acquity UPLC. Chromatographic separations were achieved by an Acquity UPLC BEH C18 column (1.7 µm, 2.1 x 50 mm). The mobile phase consisted of a water 0.3% formic acid/acetonitrile 0.3% formic acid mixture at a flow rate of 0.2 mL/min, with a sample injection volume of 5 µL. Linearity and recovery were assessed by spiking different MXF concentrations in mouse plasma with a ciprofloxacin internal standard. Calibration curves were fitted by a linear regression method through measurement of the ratios of peak areas corresponding to MXF and ciprofloxacin internal standard.

Statistics

Our previous studies using the *F. tularensis* LVS mouse model of tularemia and the same MSN-SS-MXF formulation showed differences between treatment group $\log_{10}$ CFU means of 3.3 standard deviations or larger.[3] Therefore, we chose a sample size of 3 mice per group to provide 80% power to confirm mean differences of 3.3 standard deviations or larger using the $p < 0.05$ significance criterion. We expanded the nanoparticle treatment groups to 4 mice per group for additional power to provide 80% power to confirm anticipated differences of 2.5 standard deviations or larger between the various nanoparticle treatment group means using the $p < 0.05$ significance criterion. Statistical

analyses were performed using GraphPad Prism software (version 7.04). Means were compared across groups by two-way analysis of variance (ANOVA) using the Tukey criteria to adjust p values for multiple comparisons. Comparisons of mean bacterial log CFU in the lung, liver, and spleen between mice treated with MSN-SS-MXF or an equivalent amount of free MXF were based on a logit transform linear dose response model for the log CFU results for free drug, not assuming parallel dose response relationships.[3] The adjusted mean for treatment with free drug was computed under this model, adjusted to the equivalent dose of MSN-SS-MXF, along with the corresponding p value for comparing the adjusted free drug mean to the MSN-SS-MXF mean. A p value of ≤ 0.05 was considered statistically significant.

4.4 Results and discussion

Characterization of properties of MSN-SS-MXF

We examined the MSN by transmission electron microscopy (TEM) before (Fig. 1A-B) and after surface modification for incorporation of the snap-top nanovalves (Fig. 1C-D) and observed that the MSN were well dispersed and of uniform size. Dynamic light scattering (DLS) measurement of the MSN-SS-MXF showed them to have a mean hydrodynamic diameter of 182 nm. The MSN-SS-MXF exhibited a zeta potential of -30 mV in deionized water. The MSN-SS-MXF showed a total loading of 35.9% MXF (wt/wt %), comprising 2.3% residual drug and a specific release (with DMSO and 2-mercaptoethanol reducing agent) of 33.6%. These properties are very similar to those which we have observed previously for these nanoparticles.[3]

Efficacy of MSN-SS-MXF and free MXF by 3 different routes of administration

We conducted two independent experiments to compare the treatment efficacy of MSN-SS-MXF delivered via three different routes in a mouse model of pneumonic tularemia. We infected BALB/c mice intranasally (i.n.) with 6 times the LD_{50} of *F. tularensis* LVS and one day later began treatment by the i.v., i.m., or s.c. routes with either free MXF (50 – 200 µg) or MSN-SS-MXF encapsulated MXF. In the first experiment, the MSN-SS-MXF encapsulated MXF was given at a dose of 60 µg of MXF (Fig. 2A) and in the second experiment the MSN-SS-MXF was given at doses of 50 and 100 µg MXF (Fig. 2B). Doses were given every 48 hours for a total of 3 doses. We have found in a previous study that this dosing is optimal in assessing efficacy of free vs. nanoparticle formulated MXF by intravenous administration in a mouse model of pneumonic tularemia.[3] Higher doses or more frequent administration causes an efficacy plateau (unmeasurable organ burden) precluding comparisons of treatment efficacy.

In the first experiment, the number of live LVS [colony-forming units (CFU)] in the lung at 5 hours post-infection was determined to be 2.7×10^2 per lung. One day later, the bacterial burden increased to 1.4×10^5 CFU per lung. Without treatment, the bacteria continued to multiply in the lung and disseminate to other organs. At the end of the 6-day infection period, the bacterial number had multiplied to more than 10^7 CFU in the lung and 10^6 – 10^7 CFU in the liver and spleen (Figure 2A).

In the first experiment, MSN-SS-MXF (60 µg) given by the i.m. route showed efficacy in reducing bacterial burden in the lungs comparable to that of a 3.3-fold larger dose (200 µg) of free drug given by the same i.m. route. MSN-SS-MXF was also more effective by

the i.m. route than the s.c. or i.v. routes. By the s.c. route, MSN-SS-MXF (60 µg) was more effective than 100 µg of free MXF, and by the i.v. route, the efficacy of MSN-SS-MXF (60 µg) was comparable to that of 100 µg of free MXF. In the liver, i.m. MSN-SS-MXF (60 µg) was more effective than 100 µg of free MXF given i.m. and was more effective than MSN-SS-MXF (60 µg) given i.v. or s.c. MSN-SS-MXF (60 µg) given i.m. reduced bacterial burden in the spleen to a greater extent than 100 µg of free MXF by the same route. MSN-SS-MXF (60 µg) given i.v. or s.c. also decreased bacterial burden to a greater extent than 100 µg of free MXF by the same routes.

In the second experiment, the number of bacteria in the lung at 5-hours and 1-day post infection was 1.5×10^2 CFU and 8×10^4 CFU, respectively. At day 6, the organ burden of bacteria was approximately 10^7 CFU in the lung and $10^5 – 10^6$ CFU in the liver and spleen (Figure 2B). Similar to the first experiment, MSN-SS-MXF (50 µg) given i.m. was as effective as a 4-fold higher dose (200 µg) of free MXF delivered by the same route in reducing bacterial burden in the lung. Also as observed in the first experiment, MSN-SS-MXF administered i.m. was more effective in reducing the lung bacterial load than equal amounts of MSN-SS-MXF given s.c. or i.v. In the liver and spleen, the effect of MSN-SS-MXF given by these three different routes could not be compared because bacterial number in these organs was reduced to a level below the experimental detection limit after treatment with three 50 µg doses, the lower of the two doses tested.

The design of these two experiments was the same except that, in the second experiment, to facilitate comparison of the different treatment methods, we included two concentrations of MSN-SS-MXF to match the lower (50 µg) and medium (100 µg) doses of free MXF. The infection dose was slightly different between the two studies, but within

the range of variation commonly seen in this type of animal infection model. Nevertheless, both studies showed that MSN-SS-MXF was more potent than free MXF and the drugs were more efficacious when given i.m. than i.v.

The median-effect equation[9,10] is widely used for modeling dose-response curves,[13–15] and we found that it accurately modeled our data. We used the median-effect equation to model the dose – response relationship between free MXF, administered by each of the routes, and reduction in bacterial burden in each of the organs, thereby allowing us to calculate – for each route and for each organ – the dose of free drug that would yield a comparable reduction in bacterial burden to MSN-delivered drug. We define the efficacy ratio as the ratio of the free drug to MSN-delivered drug that yields the same reduction in bacterial burden. Table 1 indicates the ratio of bio-equivalent amounts of MSN-SS-MXF to free MXF given by the same route. The efficacy ratios in the lung for MSN-SS-MXF vs. free MXF administered i.m., s.c., or i.v. were 2-3:1 in the first experiment and 3-4:1 in the second experiment (Table 1). The i.m. route had higher MSN-SS-MXF:free MXF efficacy ratios than s.c. and i.v. routes in liver and spleen in the first experiment and about the same efficacy ratios as s.c. and i.v. routes in the liver and spleen in the second experiment (Table 1); in the latter experiment, any potential improvements in the efficacy ratio by the i.m. route could not be ascertained because the efficacy of MSN-SS-MXF was already at a maximum, i.e., the bacterial burden in the liver and spleen - even with MSN-SS-MXF administered i.v. - was already reduced to the limit of detection (Fig. 2). Table 2 shows the ratio of the bio-equivalent amounts of MSN-SS-MXF and free MXF administered i.v., s.c., and i.m. relative to free MXF administered i.v. It is clear from Table 2 that MSN-SS-MXF are more efficacious than free drug by all routes of administration. Moreover, in the

lung after administration of the 50 µg dose of MSN-SS-MXF, the only site and dose level where CFU were above the limit of detection, the i.m. and s.c. routes were more efficacious than the i.v. route.

MXF formulated in nanoparticles and administered i.m. can act on *F. tularensis* at sites of infection by one of the following mechanisms: 1) nanoparticles injected into the muscle are taken up by macrophages and dendritic cells which then traffic via lymphatics and/or blood to infected organs where they release the MXF; 2) nanoparticles injected into the muscle travel freely via lymphatics or blood to infected organs, where the nanoparticles are taken up and release the MXF; or 3) nanoparticles injected into the muscle are taken up by cells in the muscle and free MXF is slowly released from muscle into the blood and circulates to the rest of the body. The i.m. route of administration generally confers a longer half-life than the i.v. route because the drug must transfer from the muscle into the systemic circulation before it can be cleared by hepatic or renal mechanisms. The nanoparticle formulation may have the advantage of conferring an even longer half-life by further prolonging the release of drug from the muscle. The third mechanism can be distinguished experimentally from the first two mechanisms by examining the lung and spleen tissue for silica and nanoparticles, since the first two mechanisms require that nanoparticles actually reach the infected organs after i.m. administration whereas the third mechanism does not.

Analysis of MSN silica in mouse organs by ICP-OES following i.m., s.c., and i.v. administration of MSN-SS-MXF

To determine whether greater delivery of MSNs to infected tissues could account for the greater efficacy of i.m. administration of MSN-SS-MXF, we measured MSN uptake into organs using inductively coupled plasma optical emission spectrometry (ICP-OES). Mice were given 3 doses, 48 hours apart, of MSN-SS-MXF i.v., s.c., or i.m. or 3 doses of PBS i.v., killed 24 hours after the last injection, their organs digested with acid, and the amount of silica assayed by ICP-OES. We found that the level of silica per gram of tissue in the lung, liver, and spleen of mice treated with MSN-SS-MXF by i.m. or s.c. was comparable to the background level of silica in mice receiving sham (PBS) injections (Fig. 3). Only in mice treated with MSN-SS-MXF by the i.v. route were levels of silica in the organs greater than that in sham-treated mice (Fig. 3).

Fluorescent MSNs are detected in the cells of infected organs after i.v. but not i.m. administration

To assess the trafficking of MSNs to infected cells and tissues, we infected mice i.n. with *F. tularensis* LVS that express GFP (LVS-GFP), and two days later injected DyLight 650-labeled MSNs into the mice by the i.v. and i.m. routes. One day after injection, the organs were digested enzymatically and by physical methods, immunostained with a fluorescent antibody to F4/80 (a mouse macrophage marker), and the cells examined with an ImageStream Mark II flow cytometer to assess co-localization of the MSNs and LVS-GFP. Whereas MSNs were present in infected F4/80+ macrophages of the lung and spleen (as well as F4/80- cells) following i.v. administration, they were not present in any cells (infected or uninfected) of these mouse organs after i.m. administration (Fig. 4). Thus, our flow cytometry findings (Fig. 4) were consistent with our ICP findings (Fig. 3); only i.v. administration of MSNs yielded detectable

MSNs in the lung tissue, whereas i.m. administration did not. These results indicate that the MSN-SS-MXF do not travel to infected organs (lung, liver, or spleen) after i.m. administration, leaving only the pharmacokinetic explanation as a viable mechanism for the greater efficacy of MSN-SS-MXF when given by the i.m. vs. the i.v. route.

Pharmacokinetics of MXF in the blood following administration of free or MSN-SS-MXF by i.v. and i.m. routes

Because our ICP analysis and flow cytometry analysis both indicated that i.m. administered MSN-SS-MXF do not traffic to the lung, we used LC-MS to explore whether improved pharmacokinetics could account for the greater efficacy of i.m. vs. i.v. MSN-SS-MXF and the greater efficacy of MSN-SS-MXF vs. unencapsulated MXF. We administered a larger dose of MXF for these pharmacokinetic studies (280 µg MXF) because preliminary studies indicated that the lower doses (e.g. 50 µg) used in the efficacy studies provided too few data points above the limit of detection to adequately characterize and compare the PK profiles obtained with the different routes and formulations. Because the pharmacokinetics of fluoroquinolones in general[16,17] and MXF in particular[18,19] have been shown to be linear, our PK-PD indices determined with the 280 µg MXF dosing in our PK studies can be extrapolated to the lower 50 – 60 µg dosing used in our efficacy studies. The 280 µg MXF dose corresponds to 14 mg/kg and is not a high dose, as it is lower than the 100 mg/kg dose that has been used in other mouse infection models of tularemia[20] and tuberculosis.[21]

Mice were given equivalent amounts (280 µg) of free MXF or MSN-SS-MXF i.v. or i.m. and blood was obtained at sequential times thereafter for determination of MXF

concentration by LC-MS (Figure 5). C_{max} values, defined as the highest concentrations measured as assessed from the time – concentration plot (Fig. 5), were highest for i.v. free MXF and i.v. MSN-SS-MXF, and lowest for i.m. MSN-SS-MXF (Table 3). The area under the curve (AUC) calculated by the linear trapezoidal method was lowest for the i.v. free MXF and similar for the i.v. MSN-SS-MXF, i.m. free MXF, and i.m. MSN-SS-MXF (Table 3). When calculated by the linear-up, log-down trapezoidal method,[22] i.m. MSN showed the greatest AUC, but the difference does not appear to be great enough to account for its markedly greater efficacy (Table 3). On the other hand, the i.m. MSN-SS-MXF yielded a much longer half-life for MXF (6.9 hours) than i.v. MSN-SS-MXF (4.9 hours) and a considerably longer half-life than i.v. and i.m. free MXF (0.9 and 0.7 hours, respectively). Because of its much longer half-life, the time above the MIC for a 280 µg dose is longer following i.m. MSN-SS-MXF (24 hours) than i.v. MSN-SS-MXF (14 hours) and dramatically longer than for free MXF administered either i.v. or i.m. (5.1 and 5.5 hours, respectively). The same rank order of PK-PD indices are obtained assuming linear pharmacokinetics and extrapolating from the 280 µg dose used in our PK studies to the 50 µg dose used in our efficacy studies (Fig. 6 and Table 3). While all of the t>MIC values are shorter using the lower dose, the rank order remains the same, with i.m. MSN-SS-MXF being the longest (6.9 hours), i.v. MSN-SS-MXF the second longest (4.75 hours), and the i.m. and i.v. free MXF being the shortest (3.62 and 2.87 hours, respectively). The AUC/MIC and Cmax/MIC indices are proportionally decreased (Table 3). The t>MIC values predicted for the 50 µg dose of free MXF or MSN-SS-MXF given by the i.m. or i.v. routes correlate well with the observed lung CFU efficacy ratios, with a positive correlation coefficient (R^2 = 0.992, Fig. 6B). AUC/MIC has a positive but weaker correlation with

efficacy ratio (R^2 = 0.75, Fig. 6C), and C_{max}/MIC shows a negative correlation with efficacy ratio (Fig. 6D).

DISCUSSION

Research into antibiotic formulations, delivery platforms, and routes of administration has the potential to improve therapeutic index by increasing efficacy and decreasing toxicities. For example, in the case of fluoroquinolones, a liposomal formulation of ciprofloxacin delivered by the inhalational route has been shown to be much more effective than oral ciprofloxacin in a mouse model of pulmonary tularemia using the highly virulent Schu S4 strain of *F. tularensis*.[23] Liposomal and nanoparticle formulations each have advantages and disadvantages. While liposomal formulations are highly biocompatible and several have already received FDA approval for marketing, mesoporous silica nanoparticles have several potential advantages, including: 1) an extremely high drug loading capacity because of their high internal surface area,[24] 2) high physicochemical stability (e.g., they are not subject to phospholipid hydrolysis, phospholipid oxidation, and have negligible drug leakage), 3) a rigid structure that can be manufactured with different sizes and aspect ratios to optimize tissue penetration and cellular targeting properties,[25,26] 4) versatility in incorporation of design features to achieve stimulus controlled drug release from the pores of the MSNs (e.g. in response to a change in redox potential, as in the current study),[1–4] and 5) facile modification of the surface of the MSNs by attachment of ligands to promote specific cellular targeting.[1,24,27]

We have demonstrated in a mouse model of pneumonic tularemia that MXF formulated in redox-operated MSNs is markedly more efficacious than an equivalent amount of free

drug and that this greater efficacy is further enhanced by administration of the MSNs i.m. vs. i.v. The greater efficacy of the MSN formulation is not attributable to enhanced delivery of the MSNs to infected cells or tissues, but instead to the markedly longer half-life of the MXF and the markedly longer duration that blood levels of MXF are above the MIC.

Three different pharmacokinetic parameters have been correlated with antibiotic treatment efficacy in various antibiotic-infection models: the ratio between peak blood level and MIC (Cmax/MIC); the AUC/MIC ratio; and time above MIC (t>MIC).[28–30] While administration of free MXF or MSN-SS-MXF i.v. leads to much higher Cmax than administration of MSN-SS-MXF i.m. (Fig. 5), the higher Cmax does not result in greater efficacy (Fig. 6D), suggesting that t>MIC or AUC/MIC is a more important factor in treatment efficacy in our model. While the linear trapezoidal method of AUC calculation is the standard method described in FDA guidance for bio-equivalence studies,[31] the linear-up/log-down trapezoidal AUC is likely a more accurate estimation of AUC as it corrects for the logarithmic as opposed to linear decline in MXF blood levels during the elimination phase.[22] Calculated by this method, the AUC/MIC ratio predicts the following efficacy ranking: i.m. MSN-SS-MXF > i.v. MSN-SS-MXF = i.m. free MXF > i.v. free MXF. On the other hand, t>MIC predicts an efficacy ranking of i.m. MSN-SS-MXF > i.v. MSN-SS-MXF > i.m. free MXF = i.v. free MXF (Table 3 and Fig. 6C). Table 2 data (excluding data for sites and doses at the limit of detection) show that the observed efficacy ranking matches the t>MIC prediction rather than the AUC/MIC prediction (Fig. 6B). This suggests that for our mouse model of tularemia, MXF efficacy is more time-dependent than concentration-dependent, i.e. concentrations substantially higher than the MIC do not provide more effective killing but concentrations above the MIC for a longer time do.

Both the antibiotic and the infectious agent are critical in determining which pharmacokinetic parameter is most important. In our system, i.m. administration of MXF in redox-operated snap top nanoparticles led to a dramatically prolonged half-life and prolonged t>MIC. While t>MIC was the best predictor of efficacy in our model of MXF treatment of pneumonic tularemia, in other infection-antibiotic models, such as the clinical response to aminoglycoside therapy, the higher Cmax/MIC ratio provided by i.v. free drug may be more important to therapeutic efficacy. In addition, *F. tularensis* is exquisitely sensitive to fluoroquinolones, with an MIC(50) of 25 ng/mL for MXF in our studies, comparable to a published broth microdilution MIC(50) of 8 ng/ml for LVS[32] and 23 ng/ml for a *F. tularensis* subsp. *holarctica* clinical reference strain.[32] Other microbial pathogens have a higher MIC(50) for fluoroquinolones and would require higher doses than used in this study to achieve efficacy. For example, drug susceptible *M. tuberculosis* has an MIC(50) of 120 ng/ml[33] and the AUC/MIC ratio is the parameter found to be the best predictor of fluoroquinolone efficacy in a mouse model of tuberculosis.[34] We observed that nanoparticle encapsulated MXF also provided a higher AUC after i.m. than i.v. administration, and thus might also prove to be more effective for treatment of tuberculosis. Many infectious disease treatments are now shifting to drugs and formulations with longer half-lives as a means to improve treatment efficacy and to decrease the need for frequent dosing. For example, thrice weekly dosing of teichoplanin for treatment of out-patient bacterial infections,[35] once weekly treatment with dalbavancin for skin infections,[36] three times a week maintenance dosing of bedaquiline for TB treatment,[37] and once monthly dosing of cabotegravir/rilpivirine for HIV-1 infection.[38] Nanoparticle formulations such as ours and selection of dosing route (e.g. i.m. vs. i.v.)

can be used to modulate the pharmacokinetic profile, increasing both t>MIC and AUC, to optimize treatment efficacy.

While we did not observe trafficking of our i.m. and s.c. delivered MSNs to lung, liver, or spleen, it is possible that different formulations of NPs or that an intradermal (i.d.) route of administration would have yielded more delivery of the MSNs to lung, liver, and spleen. In this regard, it is noteworthy that i.d. delivered pluronic-stabilized poly(propylene sulfide) NPs (<100 nm) have been shown to traffic through lymphatics to reach the blood and then be taken up by mononuclear phagocytes in the spleen.[39] Indeed, the i.d. delivered NPs provided a 50% greater bioavailability in the blood than NPs delivered i.m.[39]

4.5 Conclusion

We have shown in a model of pulmonary tularemia that MXF encapsulated within redox-activated MSN is markedly more effective than free drug and that the i.m. route is more effective than the i.v. route. We have shown that this increased efficacy is not attributable to improved targeting, but instead to prolongation of the drug half-life and improved pharmacokinetics. In these studies, our MSN-SS-MXF have not been modified to include any specific targeting features, but instead rely on passive uptake. When given by the i.v. route, uptake is primarily into cells of the mononuclear phagocytic system in liver, spleen, and lung, which correlates well with the cells that are infected by *F. tularensis*. Indeed, our fluorescence flow cytometry analysis confirmed successful targeting of the nanoparticles administered by the i.v. route to infected cells in the lung. Nevertheless, we observed higher efficacy when the MSN-SS-MXF was given by i.m. and s.c. routes that did not lead to uptake of the nanoparticles by infected cells in these organs. While

pharmacokinetic parameters proved more important than nanoparticle targeting in these studies, it is possible that incorporation of additional design features that further enhance nanoparticle targeting and delivery to lung tissue and to infected cells[40,41] would enhance the efficacy of the i.v. route of NP administration.

Abbreviations

ANOVA, analysis of variance; APTES, 3-aminopropyl triethozysilane; AUC, area under the curve; CFU, colony forming unit; C_{max}, maximum serum concentration; CTAB, cetyltrimethylammonium bromide; DLS, Dynamic light scattering; DMF, dimethylformamide; DMSO, dimethylsulfoxide; HTMP, 3-(trihydroxysilyl) propyl methylphosphonate;

i.d., intradermal; i.m., intramuscular; i.n., intranasally; ICP-OES, inductively coupled plasma optical emission spectrometry; i.v., intravenous; K_{el}, elimination rate constant; LC, liquid chromatography; LC-MS, liquid chromatography-mass spectrometry; $LD_{50,}$ dose causing 50% of untreated mice to die; LVS, Live Vaccine Strain; GFP, green fluorescence protein;

MIC, minimum inhibitory concentration; MSN, mesoporous silica nanoparticle; MXF, moxifloxacin; MSN-SS-Ada, adamantane-modified MSN; MSN-SS-MXF, MSN-disulfide snaptop loaded with MXF; NP, nanoparticle; PBS, phosphate buffered saline; PD, pharmacodynamics; PK, pharmacokinetics; PLGA, poly-lactic-co-glycolic acid; R^2, correlation of determination; s.c., subcutaneous; SD, standard deviation; SEM, standard error of the mean;

$t_{1/2}$, half-life; t>MIC, time above MIC; TEOS, tetraethylorthosilicate; TEM, transmission electron microscopy; TOF, time of flight; TSBC, trypticase soy broth supplemented with 0.2% cysteine; UPLC, ultra-performance liquid chromatography; wt/wt %, weight/weight percentage

4.6 Tables and figures

Table 4.1. Efficacy ratios of MSN-SS-MXF:Free MXF

Experiment	Organ	MSN-SS-MXF Dose (μg)	Route of administration		
			i.v.	s.c.	i.m.
		Experiment 1			
	Lung	60	2.10	2.40	3.36
	Liver	60	1.43	1.46	2.09
	Spleen	60	1.45	1.59	2.25
		Experiment 2			
	Lung	50	1.84	3.28	3.58
		100	2.95	3.42	4.58
	Liver	50	4.19	4.19	4.11
		100	2.11	2.07	2.04
	Spleen	50	3.65	4.07	3.71
		100	1.84	2.02	1.88

Table 4.2. Efficacy ratios relative to i.v. free MXF in experiment 2

Treatment	Organ	MXF dose (μg)	Route of administration		
			i.v.	s.c.	i.m.
Free MXF	Lung	50	1.00	0.87	1.21
		100	1.00	0.69	0.94
		200	1.00	1.00	0.86
	Liver	50	1.00	0.19	0.69
		100	1.00	0.46	0.70
		200	1.00	0.95	1.09
	Spleen	50	1.00	0.49	0.98
		100	1.00	0.69	1.16
		200	1.00	0.90	0.89
MSN-SS-MXF	Lung	50	1.85	2.87	3.07
		100	2.86	3.09	3.17
	Liver	50	4.20	4.23	4.15

	100	2.11	2.06	2.06
Spleen	50	3.57	3.61	3.57
	100	1.80	1.78	2.26

Table 4.3. Pharmacokinetic parameters of MSN-SS-MXF and free MXF after i.v. and i.m. administration of a dose corresponding to 280 µg MXF and predicted values after a dose of 50 µg MXF.

Pharmacokinetic parameters and indices measured after a 280 µg dose of MXF	Free MXF		MSN-SS-MXF	
	i.v.	i.m.	i.v.	i.m.
K_{el} ($hours^{-1}$)	0.76	0.93	0.14	0.10
$t_{1/2}$ (hours)	0.91	0.74	4.95	6.93
C_{max} (µg/ml)	1.83	1.42	1.65	0.54
Linear trapezoidal $AUC_{0\text{-}48h}$ (µg·hours/ml)	2.54	3.42	3.56	3.49
Linear-up Log-down trapezoidal $AUC_{0\text{-}48h}$ (µg·hours/ml)	1.66	2.62	2.70	3.33
t>MIC (hours)	5.14	5.50	14.65	24.06
C_{max}/MIC	73.2	56.8	66	21.6
$AUC_{0\text{-}48h}$/MIC	66.4	104.8	108	133.2
Pharmacokinetic indices predicted after a 50 µg dose of MXF	**Free MXF**		**MSN-SS-MXF**	
	i.v.	i.m.	i.v.	i.m.
C_{max} (µg/ml)	0.33	0.25	0.29	0.10

Linear-up Log-down trapezoidal $AUC_{0\text{-}48h}$				
(μg·hours/ml)	0.30	0.47	0.48	0.59
t>MIC (hours)	2.9	3.6	4.8	6.90
C_{max}/MIC	13.07	10.14	11.79	3.86
$AUC_{0\text{-}48h}$/MIC	11.86	18.71	19.29	23.79

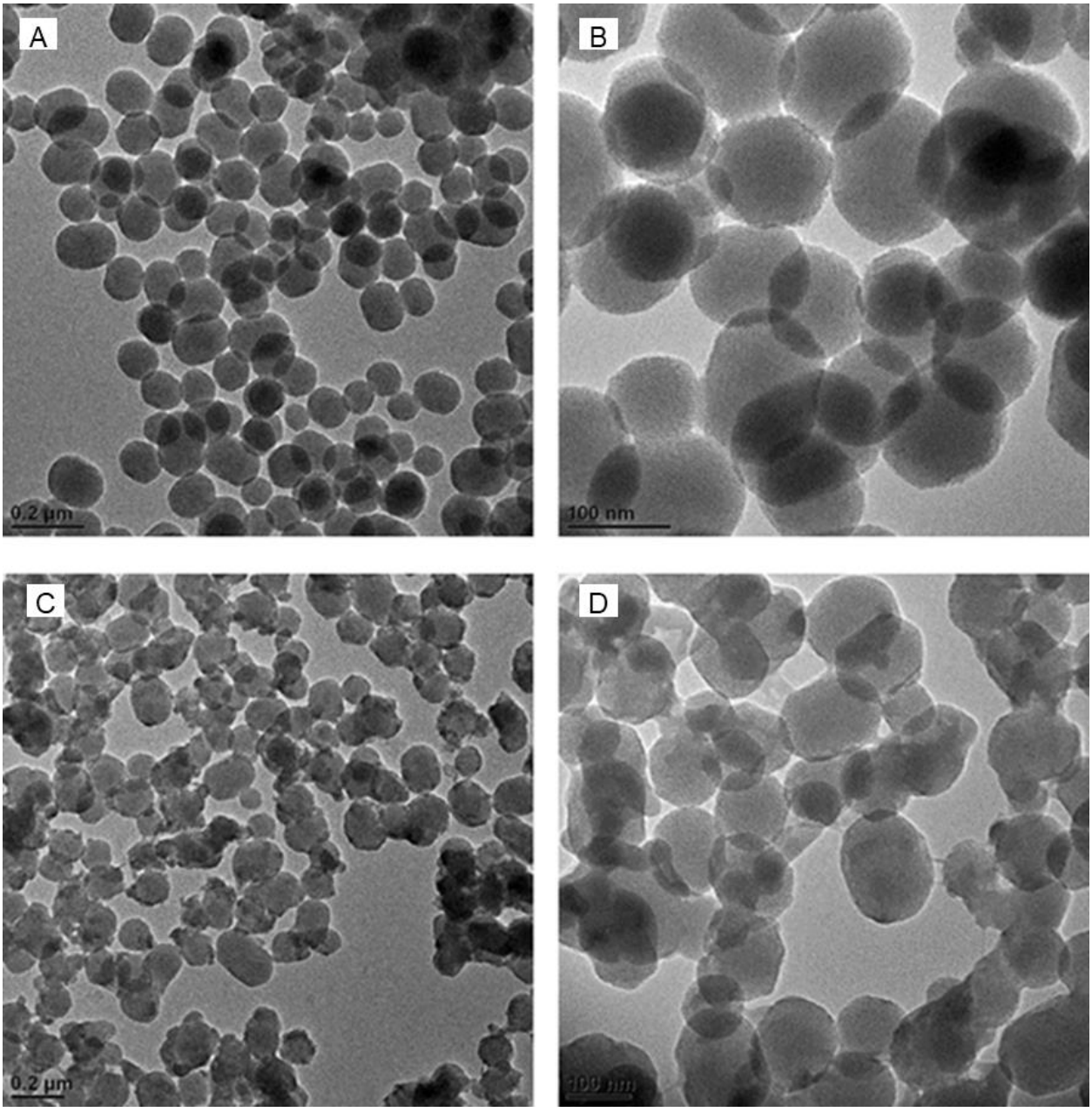

Figure 4.1. TEM image of MSN before (A - B) and after (C - D) surface modification to incorporate redox-operated snap-top nanovalves. Size bars (A, C) 0.2 µm; (B, D) 100 nm.

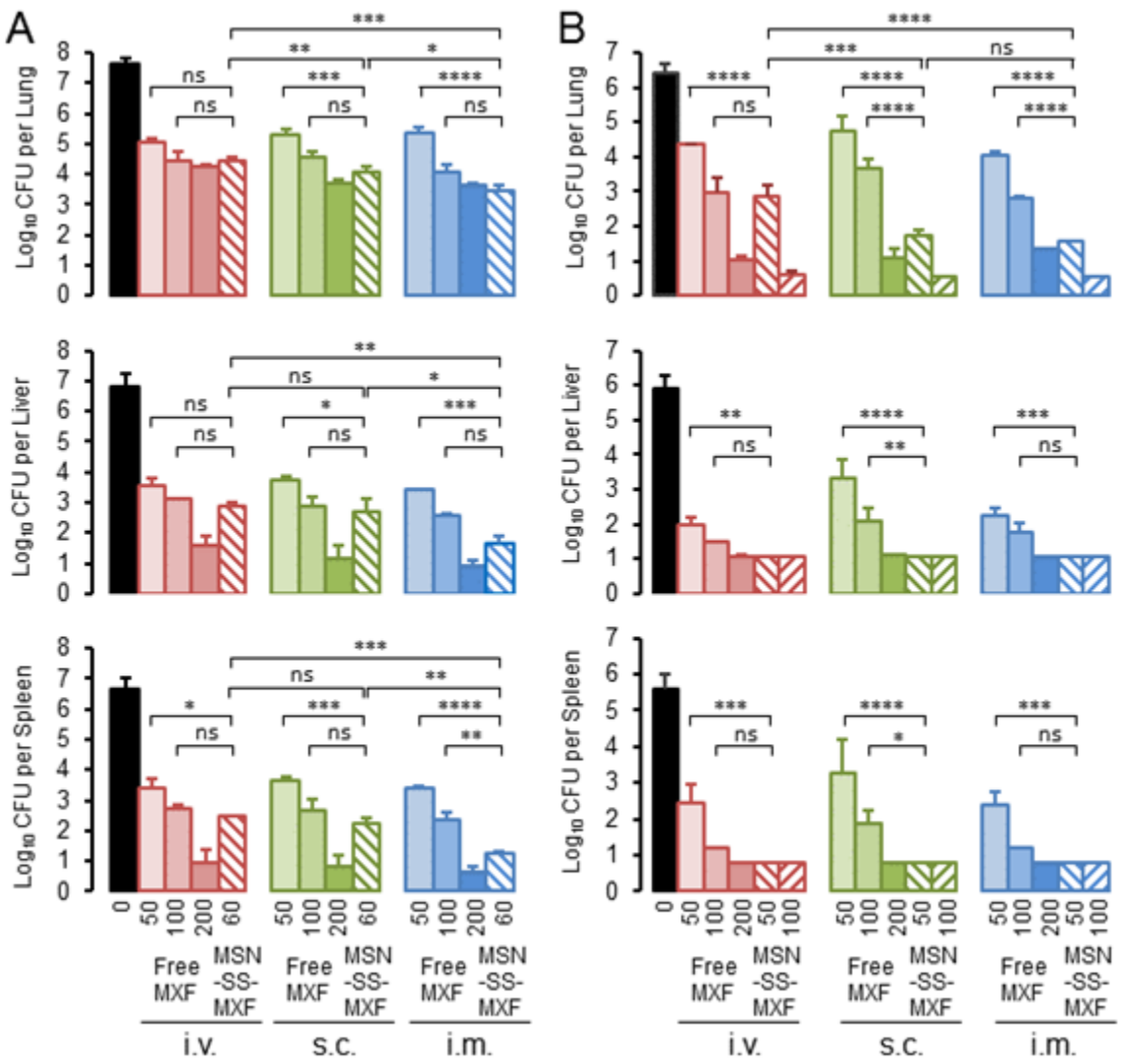

Figure 4.2. Efficacy of MSN-SS-MXF and free MXF administered i.v., s.c., or i.m. in two independent experiments. BALB/c mice were infected with F. tularensis LVS i.n. at day 0. Mice were treated on day 1, 3, and 5 with free MXF (n = 3 mice/group) or MSN-SS-MXF (n = 4 mice/group) at the dose and route of administration indicated. Control mice were sham-treated with PBS i.v. Doses of MSN-SS-MXF indicated in the first (A) and second (B) experiments were the amount of free MXF-equivalent delivered. Bacterial burdens in the lung (top panel), liver (middle panel), and spleen (bottom panel) were determined one

day after the last treatment on day 6. Data are mean ± SEM. Treatment efficacy between groups was analyzed using two-way ANOVA with Tukey's multiple comparisons test. ****, $p < 0.0001$; ***, $p < 0.001$; **, $p < 0.01$; *, $p < 0.05$; ns, not significant.

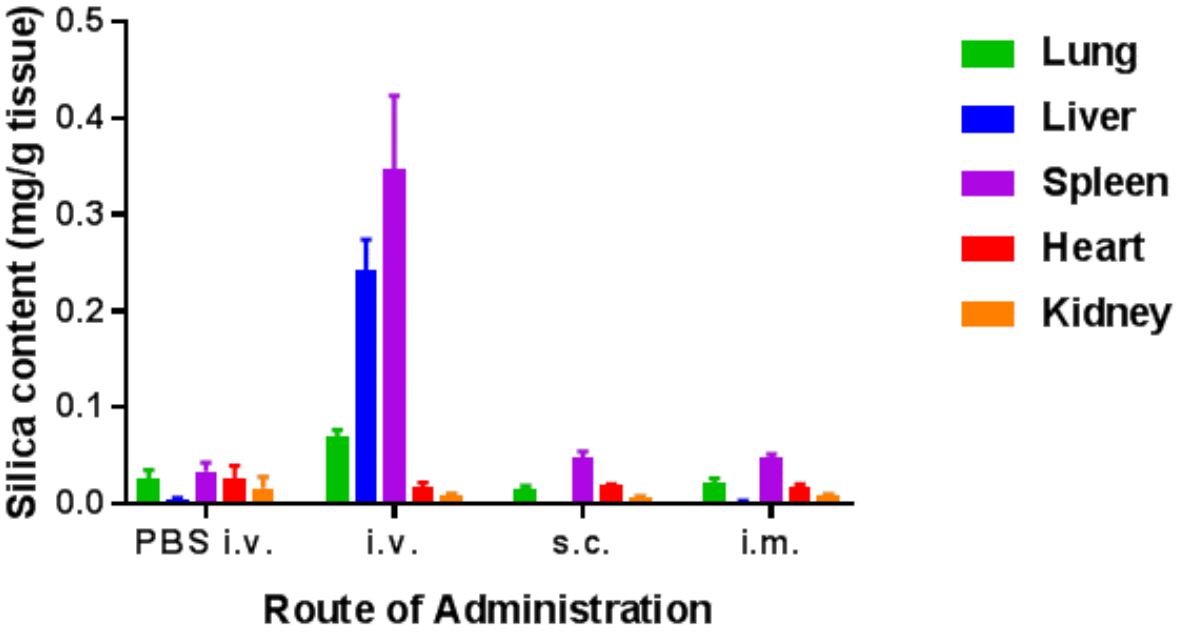

Figure 4.3. Organ biodistribution of silica. The amount of silica in organs from *F. tularensis* LVS infected mice was determined after administration of MSN-SS-MXF via the route indicated. Data are mean ± SD of 3 mice in the PBS i.v. group and 4 mice each in the MSN-SS-MXF i.v., s.c., and i.m. groups.

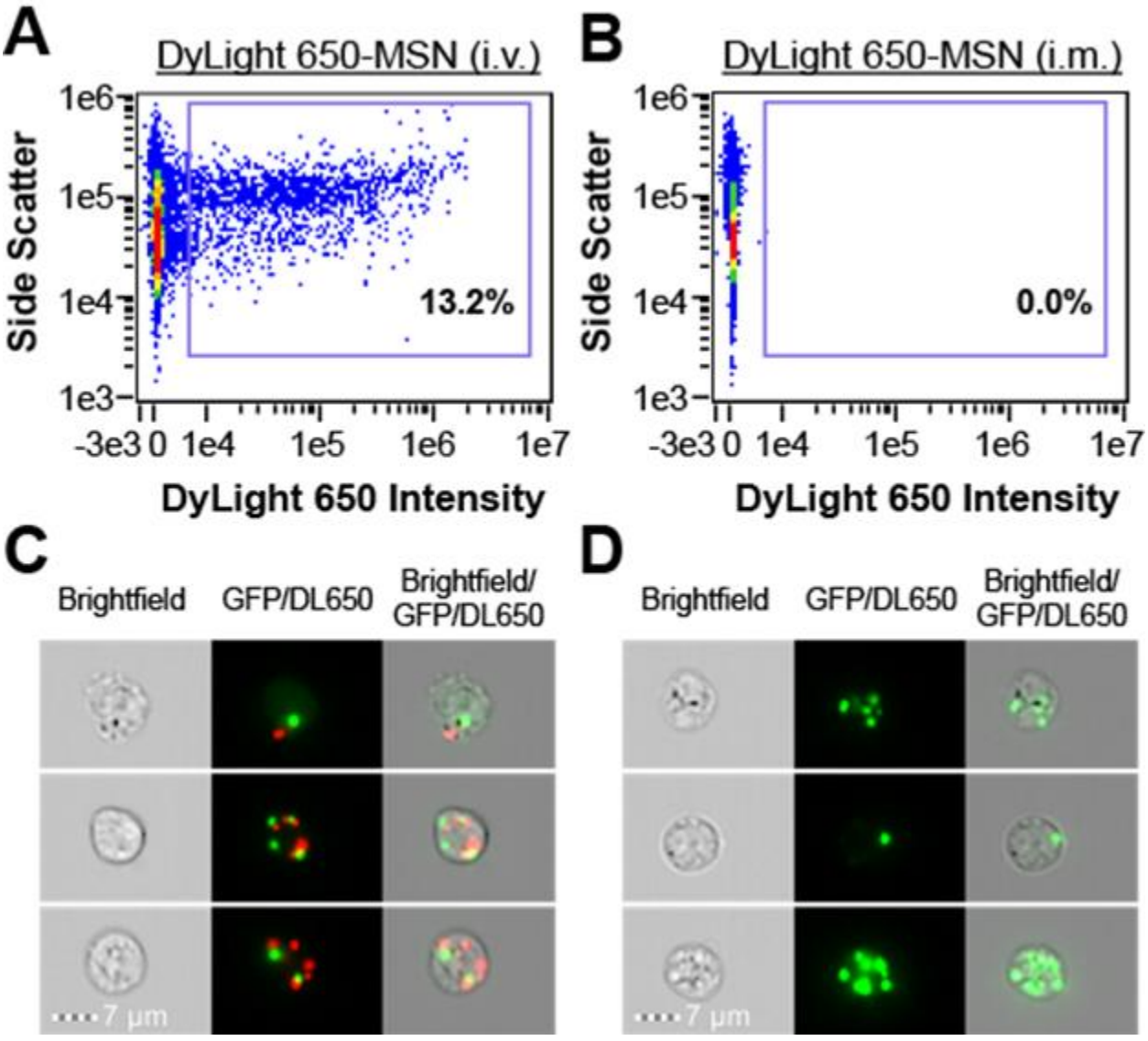

Figure 4.4. DyLight 650-labeled MSNs are detected in lung cells after i.v. but not i.m. administration. (A, B) Imaging flow cytometry density plots of lung cells from mice infected with LVS-GFP were obtained one day after i.v. (A) or i.m. (B) administration of DyLight 650-labeled MSNs. (C) Images from (A) showing DyLight 650-positive lung cells that are also GFP-positive (i.e. infected with LVS-GFP). (D) Images from (B) showing DyLight 650-negative lung cells infected with LVS-GFP.

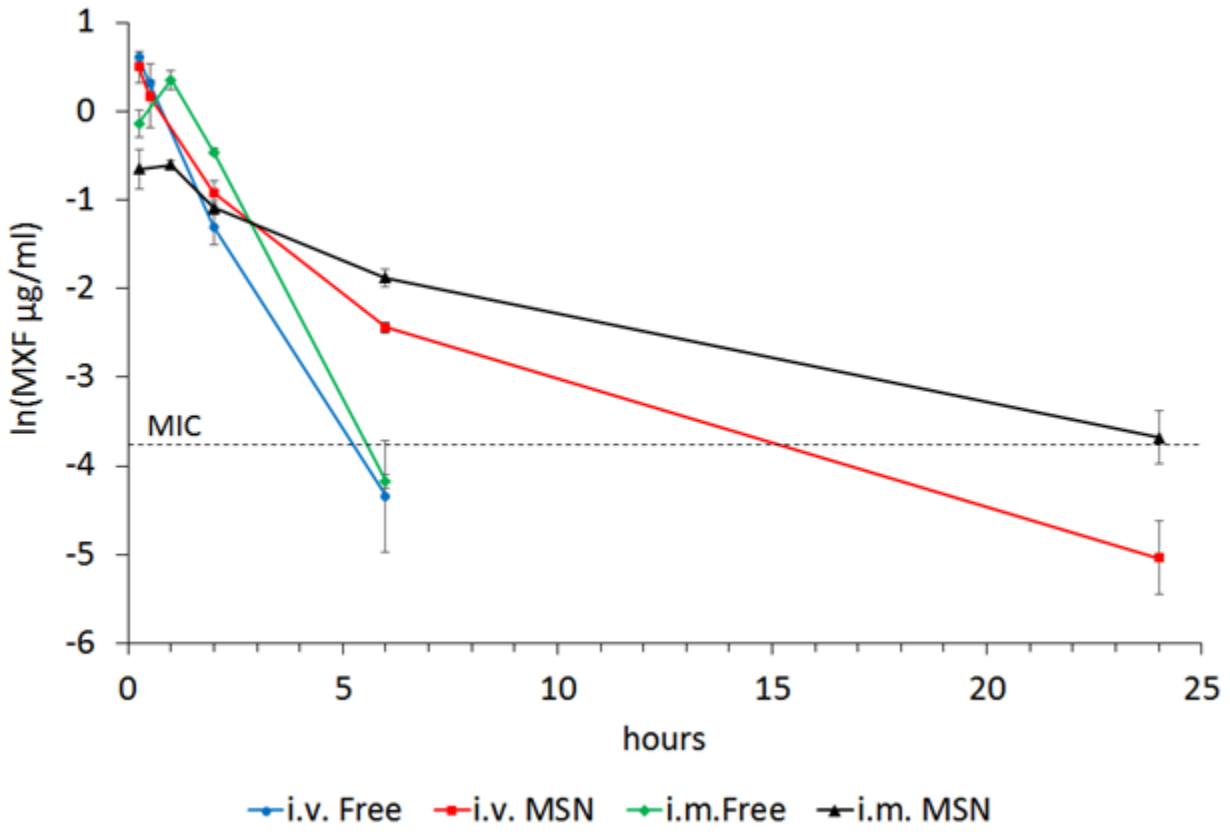

Figure 4.5. Blood levels of MXF (plotted as natural log of µg/ml concentrations) after i.v. or i.m. administration of 0.28 mg of MXF either as free drug or as MSN-SS-MXF. The MXF MIC for LVS (0.025 µg/ml) is indicated with a dotted horizontal line. Blood MXF levels were below the limit of detection at time points greater than 6 hours after i.v. and i.m. administration of free MXF. Data are means ± SEM of determinations from 3 mice/data point.

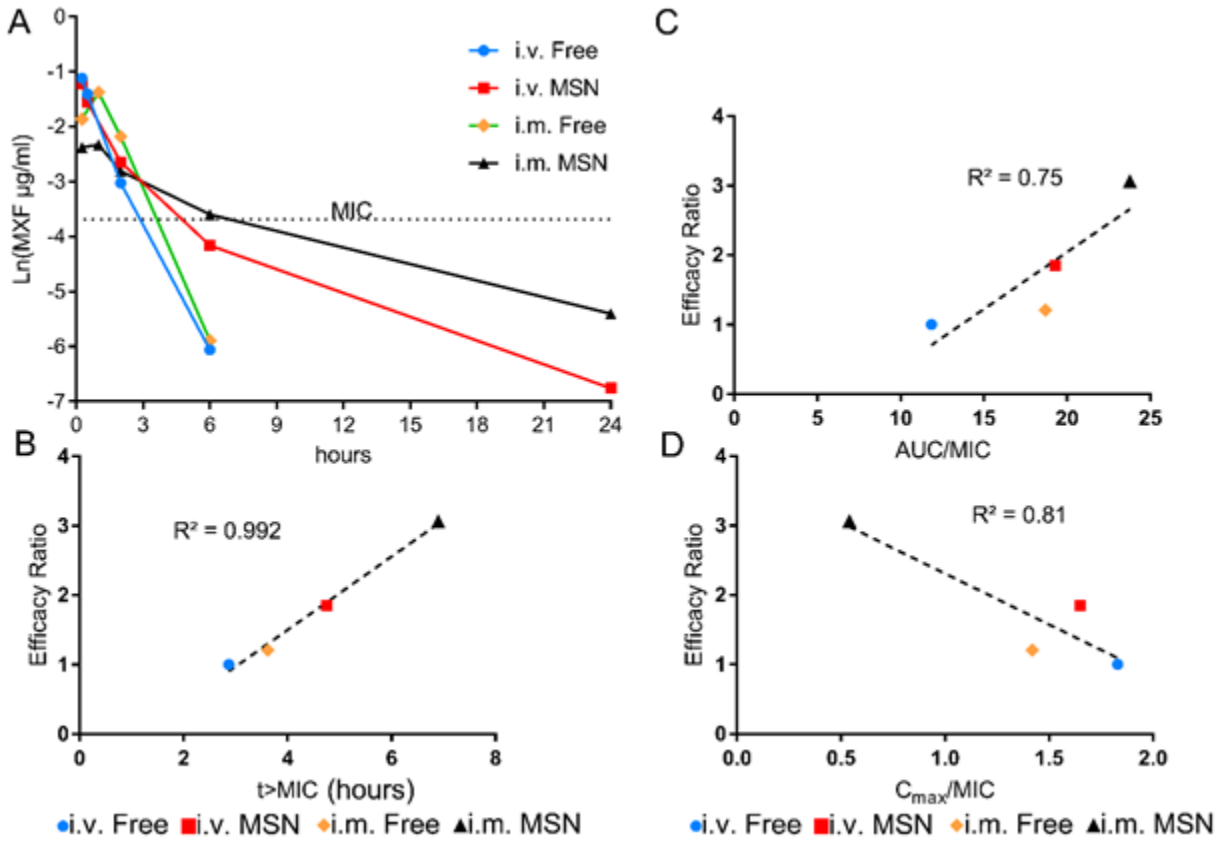

Figure 4.6. Predicted blood levels of MXF after i.v. or i.m. administration of 50 µg of MXF either as free drug or as MSN-SS-MXF (A) and plots of pharmacokinetic indices vs. efficacy ratios (B-D). (A) Blood levels of MXF are calculated, assuming linear pharmacokinetics by extrapolation from Fig. 5 and plotted as natural log of µg/ml concentrations. The MXF MIC for LVS (0.025 µg/ml) is indicated with a dotted horizontal line. (B-D) Pharmacokinetic indices for t>MIC (B), AUC/MIC (C), and Cmax/MIC (D) from Table 3 are plotted on the x-axis and corresponding lung CFU efficacy ratios for the 50 µg dose of MXF (free MXF or MXF encapsulated in MSN-SS-MXF, delivered i.m. or i.v., relative to i.v. MXF, Table 2) are plotted on the y-axis. The coefficient of determination (R^2) between the efficacy ratio and each PK index is shown in each plot.

4.7 References

1. Li, Z., Barnes, J. C., Bosoy, A., Stoddart, J. F. & Zink, J. I. Mesoporous silica nanoparticles in biomedical applications. Chem. Soc. Rev. 41, 2590–2605 (2012).
2. Coti, K. K. et al. Mechanised nanoparticles for drug delivery. Nanoscale 1, 16 (2009).
3. Lee, B. Y. et al. Redox-Triggered Release of Moxifloxacin from Mesoporous Silica Nanoparticles Functionalized with Disulfide Snap-Tops Enhances Efficacy Against Pneumonic Tularemia in Mice. Small 12, 3690–3702 (2016).
4. Ambrogio, M. W. et al. Snap-top nanocarriers. Org. Lett. 12, 3304–3307 (2010).
5. Li, S. D. & Huang, L. Pharmacokinetics and biodistribution of nanoparticles. Mol. Pharm. 5, 496 (2008).
6. Hwang, A. A. et al. pH-responsive isoniazid-loaded nanoparticles markedly improve tuberculosis treatment in mice. Small 11, 5066 (2015).
7. Clemens, D. L. et al. Targeted intracellular delivery of antituberculosis drugs to Mycobacterium tuberculosis-infected macrophages via functionalized mesoporous silica nanoparticles. Antimicrob. Agents Chemother. 56, 2535 (2012).
8. Fenaroli, F. et al. Nanoparticles as drug delivery system against tuberculosis in zebrafish embryos: direct visualization and treatment. ACS Nano 8, 7014 (2014).
9. Chou, T. C. & Talalay, P. Quantitative analysis of dose-effect relationships: the combined effects of multiple drugs or enzyme inhibitors. Adv. Enzym. Regul. 22, 27 (1984).
10. Chou, T. C. Theoretical basis, experimental design, and computerized simulation

of synergism and antagonism in drug combination studies. Pharmacol Rev. 58, 621 (2006).

11. Lee, S. J. et al. Development and validation of LC-ESI-MS/MS method for analysis of moxifloxacin and levofloxacin in serum of multidrug-resistant tuberculosis patients: Potential application as therapeutic drug monitoring tool in medical diagnosis. J. Chromatogr. B Anal. Technol. Biomed. Life Sci. 1009–1010, 138 (2016).
12. Respaud, R. et al. High-performance liquid chromatography assay for moxifloxacin in brain tissue and plasma: validation in a pharmacokinetic study in a murine model of cerebral listeriosis. J. Anal. Methods Chem. 2012, 436349 (2012).
13. Sampah, M. E. S., Shen, L., Jilek, B. L. & Siliciano, R. F. Dose–response curve slope is a missing dimension in the analysis of HIV-1 drug resistance. Proc. Natl. Acad. Sci. U. S. A. 108, 7613 (2011).
14. García-Fuente, A. et al. CISNE: An accurate description of dose-effect and synergism in combination therapies. Sci. Rep. 8, 4964 (2018).
15. Lee, J. J. & Kong, M. Confidence intervals of interaction index for assessing multiple drug interaction. Stat. Biopharm. Res. 1, 4 (2009).
16. Scaglione, F., Mouton, J. W., Mattina, R. & Fraschini, F. Pharmacodynamics of levofloxacin and ciprofloxacin in a murine pneumonia model: peak concentration/MIC versus area under the curve/MIC ratios. Antimicrob. Agents Chemother. 47, 2749 (2003).
17. Lode, H., Borner, K. & Koeppe, P. Pharmacodynamics of fluoroquinolones. Clin.

Infect. Dis. 27, 33 (1998).

18. Stass, H., Dalhoff, A., Kubitza, D. & Schuhly, U. Pharmacokinetics, safety, and tolerability of ascending single doses of moxifloxacin, a new 8-methoxy quinolone, administered to healthy subjects. Antimicrob. Agents Chemother. 42, 2060 (1998).
19. Sullivan, J. T. et al. Pharmacokinetics of a once-daily oral dose of moxifloxacin (Bay 12–8039), a new enantiomerically pure 8-methoxy quinolone. Antimicrob. Agents Chemother. 43, 2793 (1999).
20. Piercy, T., Steward, J., Lever, M. S. & Brooks, T. J. G. *In vivo* efficacy of fluoroquinolones against systemic tularaemia infection in mice. J. Antimicrob. Chemother. 56, 1069 (2005).
21. Yoshimatsu, T. et al. Bactericidal activity of increasing daily and weekly doses of moxifloxacin in murine tuberculosis. Antimicrob. Agents Chemother. 46, 1875 (2002).
22. Chiou, W. L. Critical evaluation of the potential error in pharmacokinetic studies of using the linear trapezoidal rule method for the calculation of the area under the plasma level--time curve. J. Pharmacokinet. Biopharm. 6, 539 (1978).
23. Hamblin, K. A. et al. Liposome encapsulation of ciprofloxacin improves protection against highly virulent Francisella tularensis Strain Schu S4. Antimicrob. Agents Chemother. 58, 3053 (2014).
24. Tarn, D. et al. Mesoporous silica nanoparticle nanocarriers: biofunctionality and biocompatibility. Acc. Chem. Res. 46, 792 (2013).
25. Meng, H. et al. Aspect ratio determines the quantity of mesoporous silica nanoparticle uptake by a small GTPase-dependent macropinocytosis mechanism.

ACS Nano 5, 4434 (2011).

26. Huang, X., Teng, X., Chen, D., Tang, F. & He, J. The effect of the shape of mesoporous silica nanoparticles on cellular uptake and cell function. Biomaterials 31, 438 (2010).

27. Liong, M. et al. Mesostructured multifunctional nanoparticles for imaging and drug delivery. J. Mater. Chem. 19, 6251 (2009).

28. Wright, D. H., Brown, G. H., Peterson, M. L. & Rotschafer, J. C. Application of fluoroquinolone pharmacodynamics. J. Antimicrob. Chemother. 46, 669 (2000).

29. Moore, R. D., Lietman, P. S. & Smith, C. R. Clinical response to aminoglycoside therapy: importance of the ratio of peak concentration to minimal inhibitory concentration. J. Infect. Dis. 155, 93 (1987).

30. Schentag, J. J., Nix, D. E. & Adelman, M. H. Mathematical examination of dual individualization principles (I): Relationships between AUC above MIC and area under the inhibitory curve for cefmenoxime, ciprofloxacin, and tobramycin. DICP, Ann. Pharmacother. 25, 1050 (1991).

31. U.S. Food and Drug Administration. Guidance for Industry: Bioequivalence Guidance. Cvm 1–28 (2006) doi:10.1089/073003104322838303.

32. Yesilyurt, M. et al. Antimicrobial susceptibilities of Francisella tularensis subsp. holarctica strains isolated from humans in the Central Anatolia region of Turkey. J. Antimicrob. Chemother. 66, 2588 (2011).

33. Gillespie, S. H. & Billington, O. Activity of moxifloxacin against mycobacteria. J. Antimicrob. Chemother. 44, 393 (1999).

34. Shandil, R. K. et al. Moxifloxacin, ofloxacin, sparfloxacin, and ciprofloxacin against

Mycobacterium tuberculosis: evaluation of *in vitro* and pharmacodynamic indices that best predict *in vivo* efficacy. Antimicrob. Agents Chemother. 51, 576 (2007).

35. Lamont, E. et al. Development of teicoplanin dosage guidelines for patients treated within an outpatient parenteral antibiotic therapy (OPAT) programme. J. Antimicrob. Chemother. 64, 181 (2009).
36. Boucher, H. W. et al. Once-weekly dalbavancin versus daily conventional therapy for skin infection. N. Engl. J. Med. 370, 2169 (2014).
37. Janssen Therapeutics. Highlights of Prescribing Inforation - Bedaquiline. (2012).
38. Margolis, D. A. et al. Long-acting intramuscular cabotegravir and rilpivirine in adults with HIV-1 infection (LATTE-2): 96-week results of a randomised, open-label, phase 2b, non-inferiority trial. Lancet 390, 1499 (2017).
39. Kourtis, I. C. et al. Peripherally administered nanoparticles target monocytic myeloid cells, secondary lymphoid organs and tumors in mice. PLoS One 8, e61646 (2013).
40. Friedman, A. D., Claypool, S. E. & Liu, R. The smart targeting of nanoparticles. Curr. Pharm. Des. 19, 6315 (2013).
41. Oh, P. et al. Live dynamic imaging of caveolae pumping targeted antibody rapidly and specifically across endothelium in the lung. Nat. Biotechnol. 25, 327 (2007).

Chapter 5

Optimization of a disulfide snap-top MSNs delivery system for inhalation administration of MXF with enhanced *in vivo* efficacy

5.1 Abstract

A MSN based disulfide snap-top nanovalve delivery system was optimized for *in vivo* delivery of moxifloxacin via inhalation administrative route. An aqueous suspension of MSN-SS-MXF was then aerosolized and delivered to F. tularensis Live Vaccine Strain (LVS) infected mice using a nose only aerosolization device. The mice were exposed to a total of 0, 0.1, 0.2, or 0.7 mg of MXF (as MSN-SS-MXF), and it showed that the aerosolized nanoparticle treatments markedly reduced bacterial burdens in lung, liver and spleen. Importantly, we recently have shown that inhalational delivery of MSNs does not cause detectable toxicity (e.g. inflammatory cells, loss of cells, etc.) to lung tissues, positioning us to study the efficacy of inhalational delivery of drug-loaded MSNs against Tuberculosis (TB).

5.2 Introduction

Mesoporous silica nanoparticles (MSNs) have numerous advantages as drug delivery platforms, including stability in biological conditions, uniformity, inherent lack of toxicity, versatility in incorporating additional design features, and capacity to encapsulate high concentrations of different types of cargo due to their ultra-high internal surface area, yielding exceptionally high loading capacities.[1] MSNs can be functionalized with a variety of different internal and external surface design features, including those that allow for controlled release of cargo under specific environmental conditions.[2] Moreover, MSNs are well tolerated, bio-degradable and do not bioaccumulate.[3] Our previous studies have shown that intravenous (IV) administration of the TB drug INH via a pH controlled-release

mechanism on MSNs results in much more rapid reduction in the lung, spleen, and liver burden of Mtb than treatment with an equivalent amount of free drug in the mouse TB model.[4] We have obtained similar results treating pneumonic tularemia in mice with MSNs releasing moxifloxacin (MXF) by two different controlled-release mechanisms: pH and redox.[5,6] Intriguingly, we have found that intramuscular (IM) delivered redox-activated MSNs loaded with MXF (MSN-SS-MXF) is more efficacious than IV administered MSN-SS-MXF, and delivery of these MSNs by either route is much more efficacious than free drug.[6] Those findings enable the platform of MSN-SS-MXF as a great candidate for the delivery of anti-infectious drug moxifloxacin for the treatment of Tuberculosis (TB).

In addition, recent studies showed that using platforms of nanotherapeutics via inhalation offered enhanced efficacy over other routs of administration[7,8]. Moreover, we have found that an inhalation route for MSNs administration could deliver this nanotherapeutics with different surface charges directly to the lung macrophages.[9,10] Therefore, we propose to study the efficacy of inhalational delivery of antibiotics against the intracellular pathogen Mtb. It could be expected that the inhaled nanoparticle therapy delivers high concentrations of antibiotics directly to infected marcrophages in the lung, thus has the potential to shorten the duration of treatment needed for relapse-free cure. It is reasonable to hypothesize that aerosolized drug formulations have the potential to improve the treatment of TB both by delivery of drug directly to infected region and also by improving the pharmacokinetics of the drug in lung tissue.[11]

In this work, we optimized the synthesis of a previously proposed MSN based delivery system, namely MSN-SS-MXF with improved water dispersibility that strictly required by the inhalation route administration. In addition, the loading and release of MXF from the

MSNs was investigated and optimized. These studies enabled the delivery of MSN-SS-MXF via inhalation route by aerosolization of MSNs and achieved an enhanced efficacy of killing F. tularensis in a mouse model, exceeding the treatment efficacy of our previous experiment using the intramuscular route of administration to a curable level for the disease.

This chapter is based on work done with collaborator Daniel L. Clemens and Bai-Yu Lee at Division of Infectious Diseases, UCLA for bioassays and mouse inhalation tests.

5.3 Experimental

Materials

Cetyltrimethylammonium bromide (CTAB, 95%), tetraorthoethyl-silicate (TEOS, 98%) 3-trihydroxysilyl)propyl methylphosphonate (42% in H2O), 1-adamantanethiol (95%), 2-mercaptoethanol, lead thiocyanate (99.5%), β-cyclodextrin (≥97%), Hoechst 33342 (≥97%), and toluene (99.8%) were purchased from Sigma (St. Louis, MO). (3-mercaptopropyl) trimethoxysilane, N-(2-Aminoethyl)-3-aminopropyltrimethoxysilane (NAPTS, 90%) were purchased from Gelest (Morrisville, PA). Chloroform was purchased from EMC (Billerica, MA). Bromine and 2,2'-Dipyridyldisulfide was purchased from Fisher Scientific (Pittsburgh, PA). Chloroform was purchased from EMD (Billerica, MA).

Synthesis of Phosphonated MSNs

The synthesis of MCM-41 was based on well-established published procedures. Cetyltrimethylammonium bromide (CTAB, 250 mg, 0.7 mmol) was dissolved in H_2O (120 mL) and NaOH (875 µL, 2 M). The mixture was heated to 80 °C and kept stable for 30

min, followed by adding a mixture of tetraethyl orthosilicate (TEOS, 1.2 mL) and diethylphosphatoethyltriethoxysilane (DEPETS) (0.2 mL) drop-wise into the solution while stirring vigorously. The solution was kept at 80°C for 2 h and as-synthesized nanoparticles were centrifuged and washed thoroughly with methanol.

Synthesis of MSN-SS-ADA with thiocyanogen as oxidizing agent

The particles were synthesized according to our previous publication.[6] In a typical synthesis, phosphonated MCM-41 (100 mg) was dispersed into dry toluene (10 mL), mixed with (3-mercaptopropyl) trimethoxysilane (24 µL, 0.1mmol), and refluxed for 12 h under nitrogen atmosphere. Thiol group modified MCM-41 (100 mg) was washed and dispersed again in anhydrous toluene (10 mL) in a second step. To prepare thiocyanogen, lead thiocyanate (800 mg) was dispersed in 10 mL chloroform and titrated by bromine (200 µL) in chloroform (10 mL). The titration product mixture was filtered and the filtrate containing thiocyanogen in chloroform was light yellowish. 1-adamantanethiol (17 mg, 0.1 mmol) and as-synthesized thiocyanogen were added into the MSN toluene suspension. The disulfide oxidation reaction took four days under 4 ℃ and nitrogen gas atmosphere. As-synthesized material was yellowish and washed thoroughly with toluene, methanol and water.

Synthesis of MSN-SS-ADA with 2,2'-Dipyridyldisulfide as oxidizing agent

The particles were synthesized according to a previous publication with modifications.[12] Typically, MCM-41 (100 mg) was dispersed into dry toluene (10 mL), mixed with (3-mercaptopropyl) trimethoxysilane (24 µL, 0.1mmol), and refluxed for 12 h under nitrogen atmosphere. Then the as-synthesized thiolate MSNs (MSN-SH) were collected and

washed with ethanol thrice and dispersed in ethanol (10 ml). 2,2'-Dipyridyldisulfide (50 mg, 0.113 mmol) is added to the MSNs ethanol suspension for stirring in dark overnight. Afterwards, the as-synthesized MSN-SS-pyridine (MSN-SS-py) is then washed and dispersed in fresh ethanol with a concentration of 10 mg/ml. Eventually, 1-adamantanethiol (17 mg, 0.1 mmol) was dissolved into the MSN-SS-py suspension and kept stirring and reaction in dark overnight. The resulting MSN-SS-adamantine (MSN-SS-ADA) was collected by centrifugation and washed thoroughly by ethanol and DI water before stored in DI water for later loading of moxifloxacin experiment.

Loading of MXF into MSN-SS-ADA and capping with beta-CD

The loading of MXF molecules were realized by dissolving MXF in DI water or 1X PBS solution with a concentration of 36 mg/mL. As synthesized MSN-SS-ADA particles were pre-washed with either DI-water or 1X PBS according to the later loading environment to treat the inner pore environment of MSNs with the proper solvent. Afterwards, MSN-SS-ADA particles were dispersed in MXF in DI water or 1X PBS solution with a concentration of 10mg/ml and rotate overnight for the MXF molecule to diffuse into the pore structures. Afterwards, 40mg of beta-cyclodextrin was added to the particle suspension and rotate for another 4 hours for pore capping. Then the loaded nanoparticles, denoted as MSN-SS-MXF, was washed with specific solvent and conditions by centrifugation and resuspension. The drug molecule uptake and loading capacity was recorded by measuring the concentration of MXF in loading and washing solution and the differences was calculated for drug molecule uptaken by MSNs or loaded in MSNs after washing by weight percent.

Physicochemical characterization of the MSN

Transmission electron microscopy (TEM) images of MSN were obtained using a JEM1200-EX (JEOL) instrument (JEOL USA, Inc., Peabody, MA). Particle size and zeta potential were measured by ZetaSizer Nano (Malvern Instruments Ltd, Worcestershire, UK) with 50 µg/mL MSN dispersed in de-ionized water.

Release of MXF from MSN-SS-MXF at given condition by UV-Vis absorption and bioassays

We used a modification of our previously described F. novicida bioassay[6] to determine the maximum amount of MXF released from particles. MXF released from MSN-SS-MXF in PBS or DMSO or acidified DMSO with and without 2-mercaptoethanol was measured by determining inhibition of F. novicida growth in TSBC. Similarly, release of MXF from MSN-SS-MXF in PBS, DMSO or acidified DMSO was measured in a parallel experiment by dispersing 10 mg MSN-SS-MXF in 1 mL of given solvent and rotate overnight for cap opening and drug molecule release from the pores. Then the MSNs were spin down by centrifugation and MXF concentration in supernatant was measured by UV-Vis absorption base on Beer's law and read out by standard curve interpolation. Uptake capacity is defined as the discrepancy of MXF in loading stock solution and initial spin down supernatant (uptaken by MSNs) devided by weight of MSNs in the solution. That is, uptake capacity (wt %) = $[(W_{\text{MXF before loading}} - W_{\text{MXF after loading}}) / W_{\text{particle}})] \times 100\%$. Release capacity is defined as amount of MXF in supernatant of the release solvent after certain time for drug molecule diffusion divided by weight of MSNs in the release solvent. That is, release capacity (wt %) = $(W_{\text{released}}$ MXF / $W_{\text{particle}}) \times 100\%$.

Efficacy in Killing F. tularensis in a Mouse Model of Pneumonic Tularemia

Eight-week old, female, pathogen-free BALB/c mice purchased from Taconic were acclimated for 1 week. Mice were infected by the intranasal route with 4000–8000 CFU of F. tularensis LVS, a dose equivalent to about 6–12 times the LD_{50}, respectively. Two mice were euthanized 5 h after infection (day 0) to establish the number of bacteria in the lung at the start of the experiment. An additional three mice were euthanized 1 d later (day 1) to determine bacterial growth over that time period. Mice were then sham-treated (3 mice/group), treated with free MXF (3 mice/group for each dose) or treated with MSN-SS-MXF (4 mice/group for each dose) by tail vein injection every other day for a week (days 1, 3, and 5 for a total of three treatments). Mice were euthanized 1 d after the last treatment (day 6). Lungs, livers, and spleens from infected mice that were sham treated or treated with free MXF or MSN-SS-MXF were homogenized in PBS, pH 7.4. The organ homogenates were serially diluted and plated on GCII chocolate agar plates containing sulfamethoxazole (40 μg mL^{-1}), trimethoprim (8 μg mL^{-1}), and erythromycin (50 μg mL^{-1}) to prevent growth of contaminants. The agar plates were incubated at 37 °C for 4 d at which time the number of bacterial colonies on each plate was counted.

Statistics

Statistical analyses were performed using GraphPad Prism software (version 5.01) and R 3.2.[13] Means were compared across groups using one-way analysis of variance (ANOVA) using the Bonferroni criteria to adjust P values for multiple comparisons. Comparisons of mean bacterial log CFU in the lung, liver, and spleen between mice treated with MSN-SS-MXF or an equivalent amount of free MXF were based on a logit

transform linear dose response model for the log CFU results for free drug, not assuming parallel dose response relationships. The adjusted mean for treatment with free drug was computed under this model, adjusted to the equivalent dose of MSN-SS-MXF, along with the corresponding P value for comparing the adjusted free drug mean to the MSN-SSMXF mean. A P value of 0.05 or less was considered statistically significant.

5.4 Results and discussion

Previously, we have developed a novel MSNs based delivery system, where a disulfide snap-top nanovalve was used to realize responsive release of anti-infectious drug moxifloxacin (MXF) against pneumonic tularemia and showed enhanced efficacy over that of equivalent amount of free MXF in a mice model.[14] Specifically, the disulfide bond linking the nanovalve to the MSNs would respond to the high level of reducing environment intracellularly in the macrophage, therefore upon bond broken and pores opening up, the preloaded MXF molecules would diffuse out and induce localized high dosage cytotoxicity. The operation of this disulfide snap-top functionality was proved effective in a test tube, via bioassay and *in vitro* test of human macrophage and killing Intracellular F. tularensis, and eventually tested in a Mouse Model of Pneumonic Tularemia with over three fold more effective than the equivalent free MXF. Optimization of the loading and release amount of MXF from individual MSNs is also essential for maximize the treatment efficacy. We have investigated: a) the MSN's inner pore charges; b) the MSN's concentration of phosphonate groups; c) the MSN's disulfide stalk surface coverage; d) the loading concentration of MXF; and e) the loading pH, and found the optimal conditions to be negatively charged phosphonated MSNs (10 μL DEPETS/10 mg)

with disulfide stalk surface coverage of 10 μmol loaded with 1 mL 40 × 10^{-3} m MXF in PBS solution (pH 7.4). The as prepared disulfide snap-top MSNs with MXF loaded (MSN-SS-MXF) were administrated in the mice model via intravenous (i.v.), subcutaneous (s.c.), and intramuscular (i.m.) routes. We have discovered that the i.m. route provided the highest efficacy of treatment among the three, and detailed pharmacokinetic study was presented in Chapter 4. Herein, we tested another promising administrative route of inhalation, as previous study has shown the delivery of MSNs via inhalation would relocate the MSNs directly to the lung macrophages where most of the infectious disease happens.[10] In this work, we have studied and optimized the delivery of MSN-SS-MXF via inhalation route in a mouse model for the treatment of F. tularensis. Special requirement is raised by the inhalation administrative route as nanoparticles have to be well-dispersed in aqueous solution throughout the whole period of aerosolization process which would take up to several hours. Therefore, optimizations for nanoparticle synthesis and preparation will be discussed, together with loading and washing conditions for maximization of MXF loading and release within the MSNs. Ultimately, the killing efficacy of MSN-SS-MXF delivered via inhalation is studied and compared with the previous i.m. route. With the enhanced efficacy *in vivo*, the inhalation route of the MSN-SS-MXF delivery system manifested great potential in the treatment of various types of infectious diseases.

Alternative synthesis routes of MSN-SS-MXF and modification of the synthesis to enhance nanoparticle water dispersibility/ MXF loading & releasing

Two alternative synthesis route for preparing the MSNs modified with disulfide snap-top stalk (MSN-SS-ADA) as illustrated in Figure 5.1. Four trials of inhalation experiments

were selected and summarized in Table 5.1., showing corresponding moxifloxacin loaded MSNs snap-top particles (MSN-SS-MXF) and modification applied, and the treatment efficacy that is represented by bacteria colony forming unit (CFU) counts. As mentioned in previous discussion, we first tested our previous MSN-SS-MXF delivery system in water suspension for the first trial of inhalation route. However, as the aerosolization process took over 4 hours, rather poor water dispersibility became a major issue for the delivery as MSNs started to crash out of solution after first 15-20 min. This was not a major concern for other administrative route such as i.v. or i.m. as we could sonicate thoroughly the MSNs suspension at rather low concentration, thus MSNs would suspend rather well in those cases. For inhalation treatment, the concentration of nanoparticle aqueous suspension is normally 4-10 mg/mL which is 40-100 fold higher than that of i.v. (for i.v. route, typically not over 100 ug/mL or even lower concentration) Therefore, a strict requirement on MSNs water dispersibility is posted by this inhalation route. An alternative synthesis method using 2,2'-Dipyridyldisulfide as oxidizing agent was investigated, the as-synthesized MSN-SS-ADA was characterized by DLS and zeta potential for comparison with the other method. TEM images of as synthesized particles were shown in Figure 5.2. (B), where a rough surface can be seen for route 1 using thiocyanogen as the oxidizer. From Table 5.1., it can be found that the DLS and zeta potential values were rather similar for both synthesis routes, indicating at low concentration (tested at approximately 100 ug/ml) MSN-SS-ADA formed by both methods would have similar physiochemical property in aqueous suspension. MSNs synthesized by route 2 using 2,2'-Dipyridyldisulfide as oxidizing agent were tested in trial 2 of inhalation. The water dispersibility was much improved as the MSNs were well suspended during an up to 6

hour aerosolization process with the help of a stir bar at concentration of 4 mg/mL. However, the loading and release of MXF was lower than the previous sample from 30% to 18 %, showing limited killing efficacy *in vivo*. Meanwhile, a synthesis sequence with route 1 was applied with the removal of CTAB surfactant before the oxidation process for forming the disulfide bond. As shown in Figure 5.2. (C), the surface roughness was much reduced and a picture of the sample showed a change of color from pale yellow to brownish yellow. The as-synthesized MSN-SS-MXF with modification was tested in trial 3 of inhalation. With the improved water dispersibility and enhanced MXF release capacity, an improvement of the treatment efficacy was shown as CFU went down from 7.51 to 5.75 with a 6-hour treatment. The optimization of loading and washing condition to enhance the release capacity of MXF from MSNs was performed within each trial of inhalation experiment on individual route of synthesis. This will be briefly introduced in the following section.

Loading & washing conditions on the MXF release capacity

Optimization of loading and washing condition of MXF was conducted independently on both synthesis route before applying sample for inhalation treatment. As we have already found in our previous work[6], the charge of inner pore walls and drug molecule, the washing protocol, loading solution condition and nanovalve surface coverage are important parameters for maximizing loading and release capacity of MXF. Herein, we showed in Figure 5.2., washing with different solvent (DI water or 1X PBS) would provide rather different release performance, indicating water is a better solvent to elucidating MXF from MSNs. Also, it was shown in Figure 5.2. (B) that one time of water washing would be sufficient to remove unloaded MXF from MSNs.

Improvement in MXF efficacy in a mouse model with optimized MSN-SS-MXF

With the optimized MSN-SS-MXF by synthesis modification and loading and washing protocol optimization, the effect of different time duration of inhalation treatment with MSN-SS-MXF aerosols was investigated in a mouse model in trial 4. In brief, mice were infected by the pulmonary route with F. tularensis LVS on day 0 and given daily aerosol treatments on days 1-3, delivering the indicated total amount of MXF in MSN-MXF format. On day 4, the mice were killed and numbers of F. tularensis bacteria in lung, liver, and spleen were determined. In Figure 5.3., the absolute weight value of tested mice and weight change percentage showed that except for no treatment where body weight dropped about 8% for the mice, 2, 4, 6 hours of treatment maintained the body weight. The bacteria CFU count is illustrated in Figure 5.4. for different organs. The CFU in liver and spleen was brought down to instrument detection limit. The CFU count in lung was summarized in Table 5.2., as a 6-hour treatment offered the best killing efficacy with a mean of 0.69 from no treatment of 7.38 in log scale.

5.5 Conclusion

We have optimized the synthesis of MSN-SS-MXF, a MSN based snap-top delivery system with redox responsive disulfide linker for controllable release. The water dispersibility of such particles was enhanced by using alternative synthesis route or optimization of synthesis sequence. In the meantime, the loading and washing condition of MXF in MSNs were investigated, where it was found that the loading solvent was crucial as charge property and solubility of drug molecule would greatly affect the loading and release capacity. Eventually, an optimized drug loading and washing protocol was applied

with modified synthesis route, high amount of MXF delivery was achieved with inhalation administrative route. As a consequence, much enhanced treatment efficacy on F. tularensis infected mice was realized, bring bacteria CFU in lung down from 7.38 to 0.69 and that below detection limit in liver and spleen. With such low level of CFU counts, body immune system would facilitate the complete removal of infection and the disease could be considered curable.

5.6 Tables and figures

MSN-SS-MXF caption	Synthesis description	DLS (nm)	Zeta (mv)	Release of MXF measured by UV-Vis absorption	Release of MXF measured by bioassay	Inhalation trial brief summary
1st trial	thiocyanogen as oxidizer	397	-27	31.3%	27.1%	Water dispersity: poor
						MXF release capacity: high
						MXF delivered to lung: low
						CFU count change: NA
2nd trial	2,2'-Dipyridyldisulfide as oxidizer	247	-36	17.1%	18.3%	Water dispersity:good
						MXF release capacity: low
						MXF delivered to lung: low
						CFU count change: 7.23 – 6.64
3rd trial	Increased surface –SH, remove surfactant first, then thiocyanogen oxidizing	131	-37	29.0%	20.7%	Water dispersity: good
						MXF release capacity: decent
						MXF delivered to lung: decent
						CFU count change: 7.51 – 5.75
4th trial	Minimium washing with DI H2O	182	-30	89.4%	95.9%	Water dispersity: good
						MXF release capacity: high
						MXF delivered to lung: high
						CFU count change: 7.38 – 0.69

Table 5.1. Summary of inhalation trials and MSN-SS-MXF samples used for specific trials with a brief description of optimization on samples and nanoparticle characterizations and inhalation treatment efficacy in CFU counts.

	MSN-SS-ADA (H)	MSN-SS-ADA (P)	MSN-SS-MXF (H)	MSN-SS-MXF (P)
DLS (nm)	196.8	335.6	222.6	557.1
Zeta (mv)	-33.4±0.9	-9.3±1.7	-21.4±0.5	-8.5±2.1

Table 5.2. DLS and zeta potential of MSN-SS-ADA and MSN-SS-MXF after washing and dispersed in DI water (H) or in 1XPBS (P), respectively.

Mouse	0 h	2 h	4 h	6 h
1	7.62	2.10	0.75	0.24*
2	7.47	2.64	0.41	1.41
3	7.07	2.36	1.49	0.41
Mean	7.38	2.37	0.88	0.69

Table 5.3. The bacteria CFU count for 0, 2, 4, 6 hours of inhalation treatment of MSN-SS-MXF nanoparticles on three independent mice. (*At limit of detection)

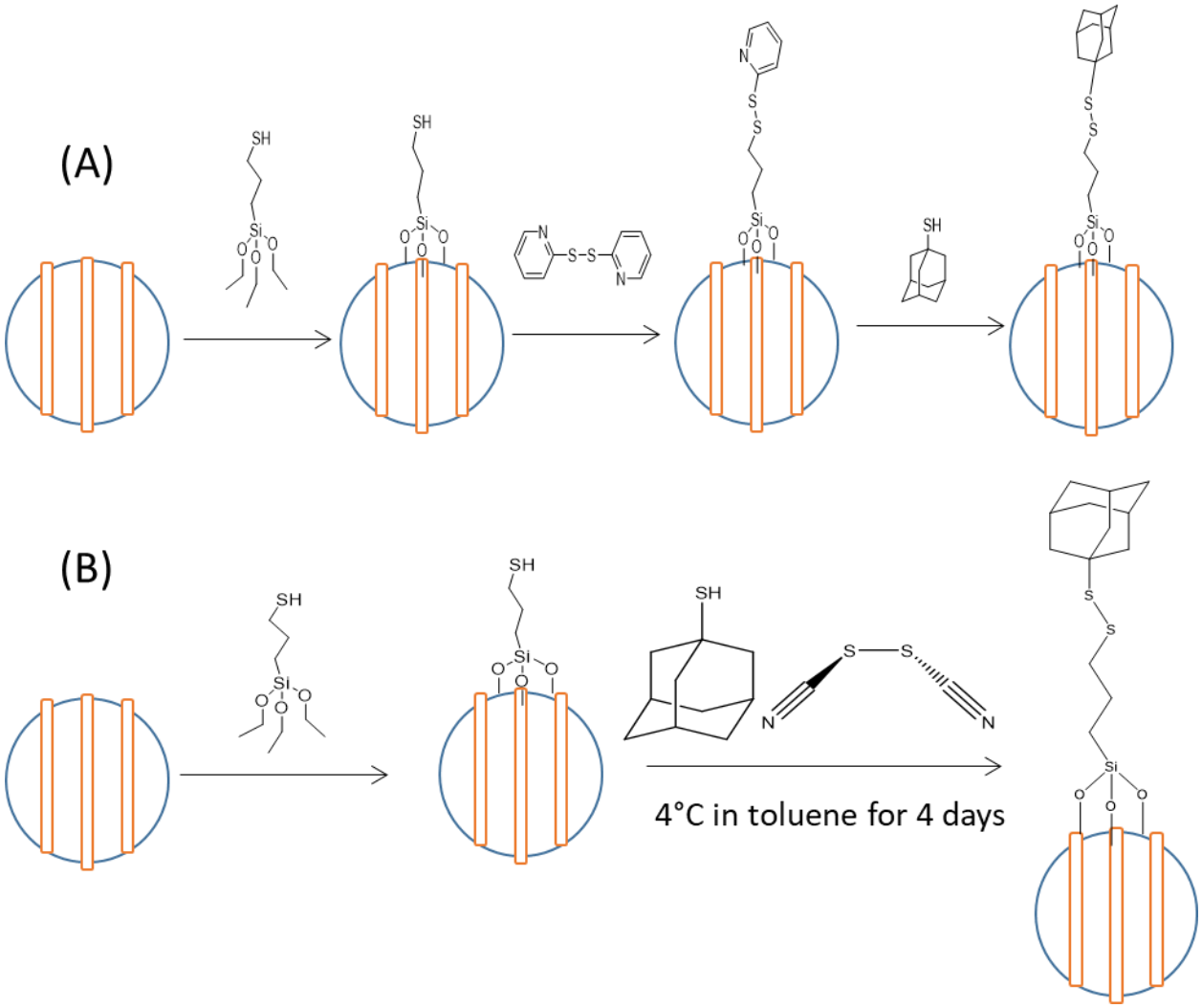

Figure 5.1. Synthesis routes of disulfide snap-top MSNs (MSN-SS-ADA), (A) using 2,2'-Dipyridyldisulfide as the oxidizing agent, (B) using thiocyanogen as the oxidizing agent.

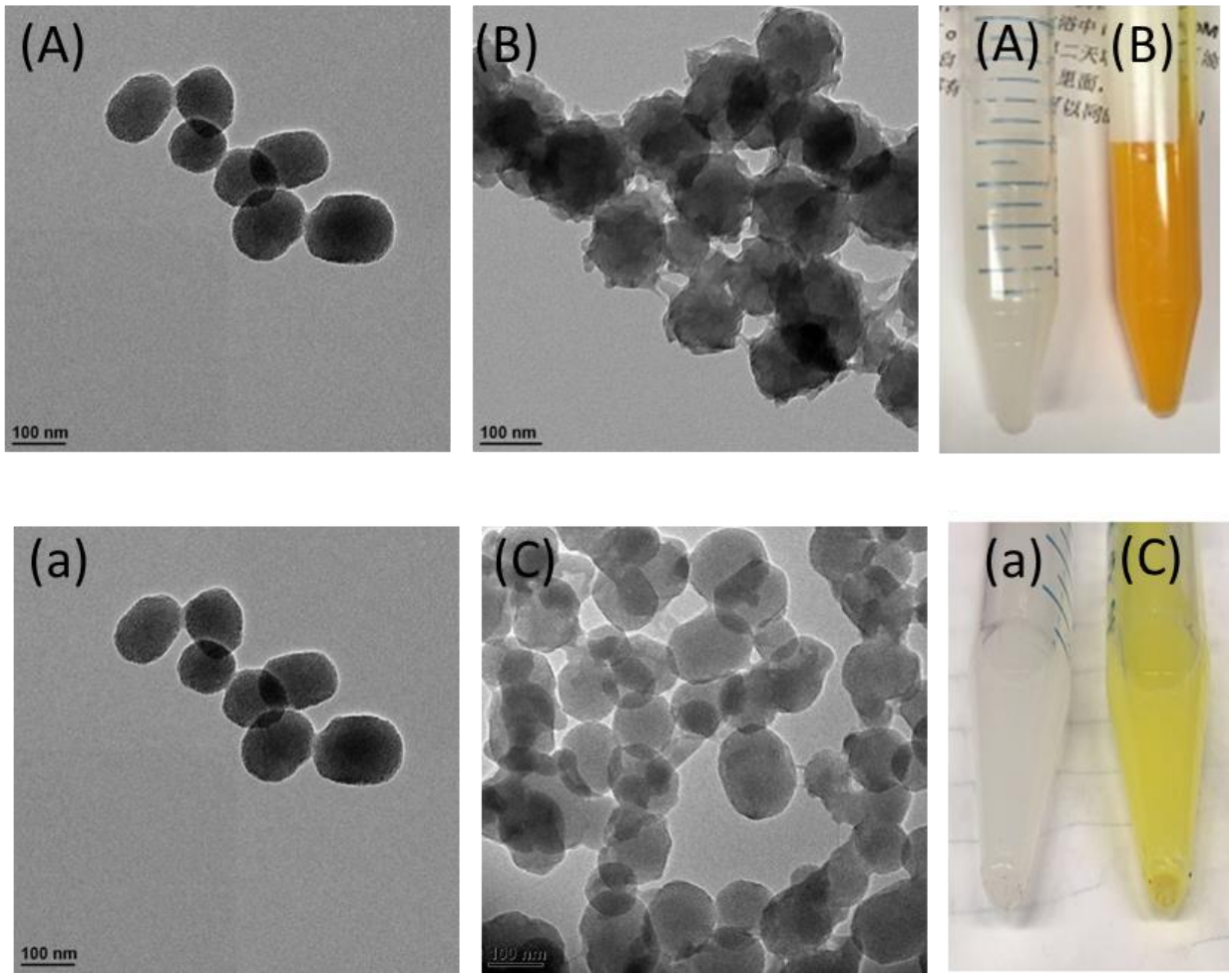

Figure 5.2. On the left: TEM images of as-synthesized MSN-SS-ADA with different synthesis routes. (A) and (a), using 2,2'-Dipyridyldisulfide as oxidizing agent; (B), using thiocyanogen as oxidizer, oxidize with presence of CTAB; (C) using thiocyanogen as oxidizer, oxidize after removal of CTAB. On the right: picture of centrifuge tubes with as synthesized MSNs colloidal suspension in H_2O at concentration of 10 mg/mL.

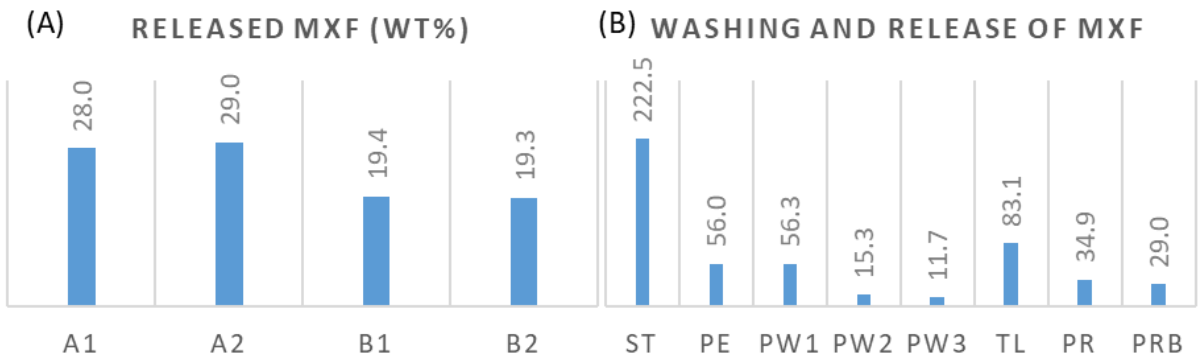

Figure 5.3. Loading and release of MXF at different conditions. (A) Release of MXF from MSN-SS-MXF (wt.% shown in Y axis) with different loading and washing protocols, A1/A2: loaded in 1XPBS, washed 3 times with 1XPBS and 2 times with DI H_2O; B1/B2: loaded in 1XPBS, washed 5 times with DI H_2O. (B) Washing and release of MSN-SS-MXF, loaded with 1XPBS, washing with 1XPBS and wt.% shown in Y axis. ST: stock solution before loading, PE: elute solution, PW1: washing-1 supernatant, PW2: washing-2 supernatant, PW3: washing-3 supernatant, TL: theoretical loading amount of MXF (= ST-PE-PW1-PW2-PW3), PR: release measured by UV-Vis absorption, PRB: release measured by bioassay.

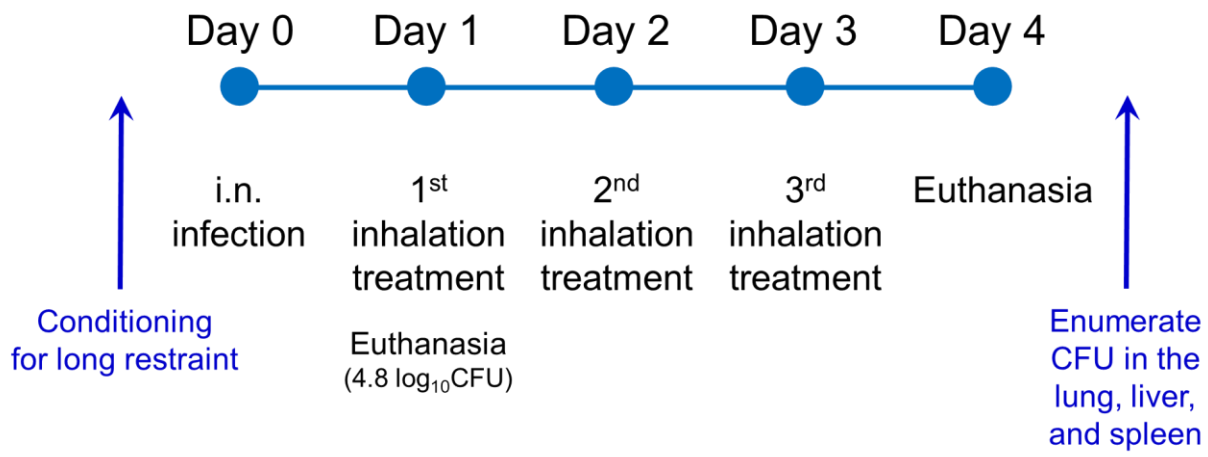

Figure 5.4. Scheme of inhalation treatment and experiment design for mice study.

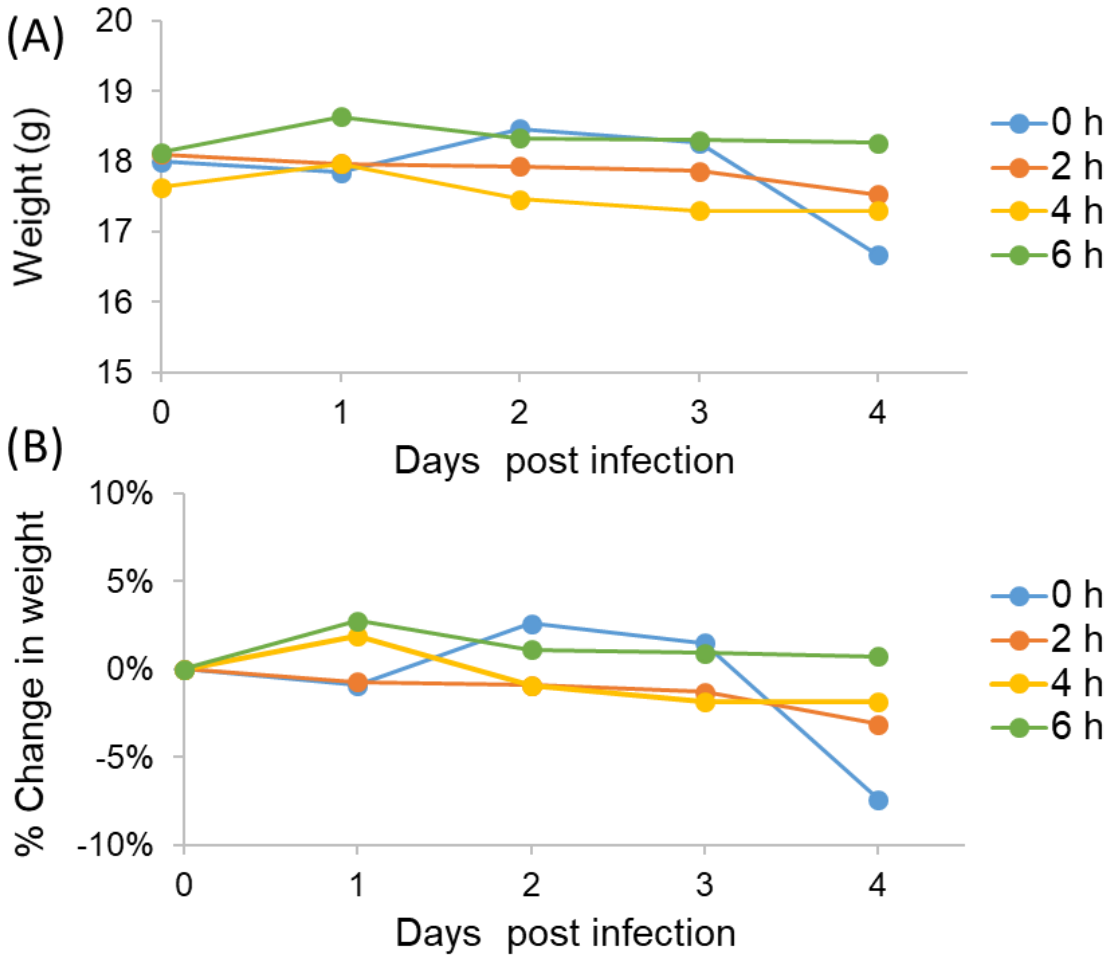

Figure 5.5. Treatment with MSN-SS-MXF prevents weight loss in mice infected with F. tularensis. Mice with pneumonic tularemia were weighed daily during the course of treatment. (A and B) Data shown are absolute weight change and percentage change of mice, respectively. The mice were treated with inhalation duration of 0, 2, 4, 6 hours, as indicated.

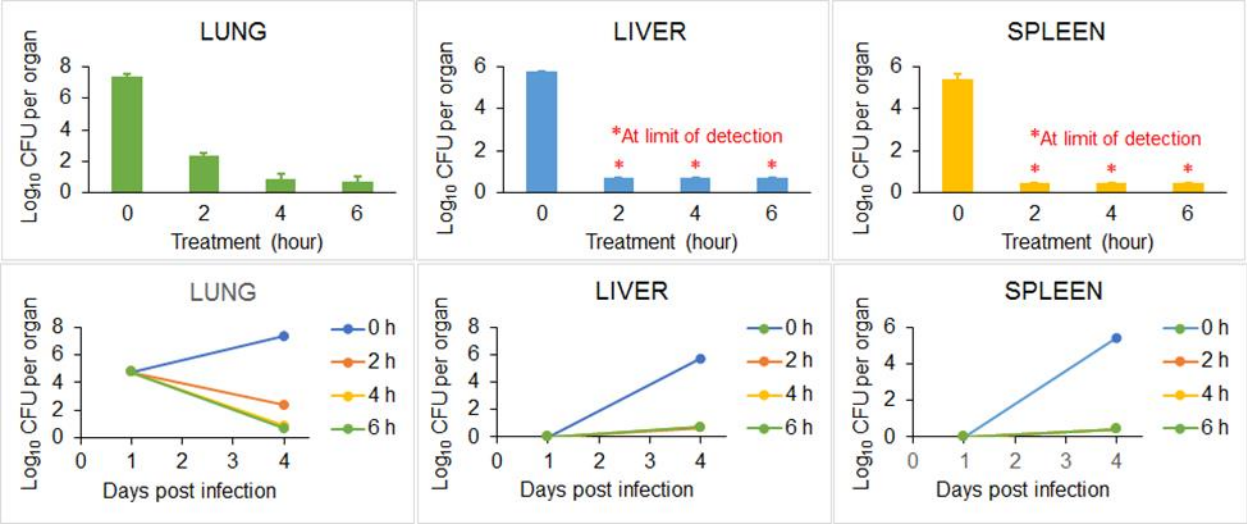

Figure 5.6. Mice were infected with F. tularensis LVS by the intranasal route. Bacterial burden in the lung was monitored over the course of infection. The mice were treated with inhalation duration of 0, 2, 4, 6 hours, as indicated. The effect of each treatment on F. tularensis burden in lung, liver, and spleen was determined by assaying the bacterial CFU one day after the final treatment.

5.7 References

1. Li, Z., Barnes, J. C., Bosoy, A., Stoddart, J. F. & Zink, J. I. Mesoporous silica nanoparticles in biomedical applications. *Chem. Soc. Rev.* **41**, 2590–2605 (2012).
2. Cotí, K. K. *et al.* Mechanised nanoparticles for drug delivery. *Nanoscale* **1**, 16–39 (2009).
3. Lin, V. S.-Y. Veni, vidi, vici and then... vanished. *Nat. Mater.* **8**, 252–253 (2009).
4. Hwang, A. A. *et al.* pH-responsive isoniazid-loaded nanoparticles markedly improve tuberculosis treatment in mice. *Small* **11**, 5066 (2015).
5. Li, Z. *et al.* Mesoporous silica nanoparticles with pH-sensitive nanovalves for delivery of moxifloxacin provide improved treatment of lethal pneumonic tularemia. *ACS Nano* **9**, 10778–10789 (2015).
6. Lee, B. Y. *et al.* Redox-Triggered Release of Moxifloxacin from Mesoporous Silica Nanoparticles Functionalized with Disulfide Snap-Tops Enhances Efficacy Against Pneumonic Tularemia in Mice. *Small* **12**, 3690–3702 (2016).
7. Hamblin, K. A., Wong, J. P., Blanchard, J. D. & Atkins, H. S. The potential of liposome–encapsulated ciprofloxacin as a tularemia therapy. *Front. Cell. Infect. Microbiol.* **4**, 79 (2014).
8. Norville, I. H. *et al.* Efficacy of liposome-encapsulated ciprofloxacin in a murine model of Q fever. *Antimicrob. Agents Chemother.* **58**, 5510–5518 (2014).
9. Li, X. *et al.* Aerosol droplet delivery of mesoporous silica nanoparticles: A strategy for respiratory-based therapeutics. *Nanomedicine Nanotechnology, Biol. Med.* **11**, 1377–1385 (2015).

10. Buskard, D. X. *et al.* Surface Charge Effects On Inhaled Engineered Nanomaterial Delivery And Retention In The Respiratory Tract Of Mice. in *C103. OUTDOOR AIR POLLUTION: EPIDEMIOLOGY AND MECHANISMS* A6838–A6838 (American Thoracic Society, 2017).
11. Clemens, D. L. *et al.* Nanoparticle Formulation of Moxifloxacin and Intramuscular Route of Delivery Improve Antibiotic Pharmacokinetics and Treatment of Pneumonic Tularemia in a Mouse Model. *ACS Infect. Dis.* **5**, 281–291 (2019).
12. Liu, H. *et al.* Integrated combination treatment using a “Smart” chemotherapy and microRNA delivery system improves outcomes in an orthotopic colorectal cancer model. *Adv. Funct. Mater.* **28**, 1801118 (2018).
13. Team, R. C. R Foundation for Statistical Computing; Vienna, Austria: 2015. *R A Lang. Environ. Stat. Comput.* 2013 (2018).
14. Lee, B.-Y. *et al.* Redox-triggered release of moxifloxacin from mesoporous silica nanoparticles functionalized with disulfide snap-tops enhances efficacy against pneumonic tularemia in mice. *Small* **12**, 3690 (2016).

Chapter 6

A facile synthesis method of mesoporous silica nanoparticles with different pore structures for pore size enlargement via an emulsion-assisted sol-gel process

6.1 Abstract

This chapter presents a facile and general synthesis procedure for the preparation of various types of mesoporous silica nanoparticles with enlarged pore size. By revisiting previous synthesis methods for the pore expansion mechanisms, we discovered an emulsion-assisted sol-gel reaction via a simple sonication process, resulting in MSNs with expanded pore size and uniform and monodispersed morphology. Synthesis parameters such as reaction temperature, addition of swelling agent to CTAB ratio and reaction pH condition were investigated for the effect on pore swelling and particle morphology. The necessity of the sonication process was also proved. The as-synthesized nanoparticles were characterized by TEM, SAXS, DLS and N_2 gas adsorption/desorption, confirming that this synthesis method is facile and highly reproducible.

6.2 Introduction

In the last decade, mesoporous silica nanoparticle (MSNs) have been proven as a great candidate as a promising drug delivery platform due to their high biocompatibility.[1–4] The normal pore size for MCM-41 is around 2.2 nm using CTAB as surfactant.[5] However, this limited size of pore is not large enough to withhold large molecules and/or DNA/siRNA. Typical dimension of a single strand 21-nt siRNA is 2.6 × 5.6 nm, which is right above the pore size limit for normal MCM-41. Though it was reported that a normal Fe_3O_4@silica core-shell system can accommodate certain siRNA or even DNA strands[6,7], larger pore size is still expected for a further increase in the cargo dimension. As a result, an ideal 4-

6 nm large pore with good accessibility and tunability will be a target structural parameter for the purpose of this study.[8–10]

The enlargement of the mesopores is often realized by the addition of micelle swelling agent, which will increase the size of the micelle.[11] (Figure 6.1.) A variety of compounds can be used as micelle expander, including benzene and its alkyl-substituted derivatives (most notably, 1,3,5-trimethylbenzene, TMB), linear hydrocarbons and other hydrophobic small molecules.[11–13] However, the pore expansion often accompanies with a loss the structure ordering.[14,15] It is thus challenging to realize the swelling effect of the pore while maintaining a reasonable structure of the particle for further use. Blocking the large pore with nanovalves for controllable cargo release have only been reported with SBA-15, the size of which is typically over 400nm and not suitable for biological applications.[16] Therefore, the swelling effect for the plain silica and core-shell system were both investigated with discussion on varying synthesis conditions. By simply mixing the swelling agent with the reaction solution before adding TEOS, an enlarged pore size could be expected with increasing ratio between the surfactant and swelling agent. Two typical swelling agents (TMB and decane) are applied according to the literature.[17] In addition, different types of base catalyst were used, and other aspects as reaction temperature, adding sequence of reactants are also employed.

In this work, a facile, highly reproducible method for the synthesis of various types of mesoporous silica nanoparticle or core-shell Fe_3O_4@MSNs with enlarged pore size is introduced. A crucial sonication treatment is involved to facilitate the emulsion-assisted sol-gel reaction for nanoparticle formation. Parameters such as reaction temperature,

reaction pH and usage of swelling agent are also discussed, showing their effect on the pore enlargement process.

6.3 Experimental

Materials

All materials were used as purchased without further purification. Cetyltrimethylammonium bromide (CTAB, 95%), tetraorthoethyl-silicate (TEOS, 98%), 1-adamantanethiol (95%), ethyl acetate (EA, ⩾ 99.7%), 2-mercaptoethanol, lead thiocyanate (99.5%), β-cyclodextrin (≥97%), Hoechst 33342 (≥97%), and toluene (99.8%) were purchased from Sigma (St. Louis, MO). (3-mercaptopropyl) trimethoxysilane, N-(2-Aminoethyl)-3-aminopropyltrimethoxysilane (NAPTS, 90%) were purchased from Gelest (Morrisville, PA). Chloroform was purchased from EMC (Billerica, MA). Bromine was purchased from Fisher Scientific (Pittsburgh, PA). Chloroform was purchased from EMD (Billerica, MA).

Synthesis of MSNs with enlarged pore size in aqueous precursor (without sonication)

A modified synthesis recipe was implanted for the large-pore MSNs synthesis. With regard to the recipe for MCM-41 synthesis as mentioned in chapter 2 and 4, same amount of reactants was used, while the molar ratio between reactants was kept as 1.0 CTAB: 2.2 NaOH: x TMB: 8.8 TEOS: 10115.0 H2O: 8.8 Ethyl acetate. Typically, 50mg cetyltrimethylammonium bromide (CTAB, Aldrich, 95%) was dissolved in 25 mL water with 150 μL NaOH (2.0 M), the solution of which was heated to 80°C under rapid stirring. After 30 minutes at this temperature, 270 μL tetraethylorthosilicate (TEOS, Aldrich, 98%)

was added dropwisely. About 1 minute afterwards, a same volume of 270 µL ethyl acetate was quickly added. The solution slowly turned to transparent blue, indicating the nucleation and growth of silica nanoparticles. Reaction was kept at 80°C for 2 hours, then the solution was cooled down to room temperature, and the nanoparticles were collected by centrifugation at 7800 rpm. The pellet from centrifugation was redispersed and washed with ethanol for three times, and dispersed in ethanol for further use. Each individual experimental trial under different synthesis conditions was labeled as S#-NaOH-1-x-T, indicating the reaction was catalyzed with NaOH with a one to x molar ratio between CTAB and TMB at certain temperature T. Likewise, when using alternative base catalyst of ammonium hydroxide, samples were labeled as N#-NH_4OH-1-x-T. Furthermore, a double swelling agent method was applied with the addition of TMB and decane before adding silica source. (An equilibrium dwell time of 2 hours was maintained for the addition of each swelling agent to make sure the penetration of swelling agents.) The samples for those trials are labelled as 1-9+3 as an example for the addition of 9 time decane and 3 time TMB with an order of adding decane first. (Same way of labelling samples was applied for core-shell samples in the next discussion section.)

Synthesis of hexagonal/ radial type pore structured MSNs with enlarged pore size in emulsion (with sonication)

Large pore MCM-41 derivative

In a typical synthesis, 0.1g CTAB (cetyltrimethylammonium bromide) is dissolved in 45 mL DI water in a 100mL round bottom flask. 350 µL sodium hydroxide solution (2M) is added to the aqueous. After the CTAB is dissolved, 305 µL TMB (1,3,5- trimethylbenzene)

is added to the solution. The flask is then brought to a water batch sonicator for continuous sonication of 30 minutes twice (total 1 hour). The mixture turned from transparent to stable white milky emulsion. In the meantime, an oil bath is heated and stabilized at a temperature of 70˚C. After the one-hour sonication, a stir bar is put in the flask and flask is transferred to the oil bath. Approximately 15 minutes later when the temperature is stabilized with the oil bath, 0.5mL TEOS (Tetraethyl orthosilicate) is added to the solution dropwisely and 0.4 mL ethyl acetate is added to the solution 150 seconds after the addition of TEOS. The reaction is kept at 70˚C for 2 and a half hours. Then the mixture is cooled to room temperature and product is separated from the aqueous mixture by centrifugation (7800rpm) and washed with water and ethanol 2 twice each. (By suspending the particle in water/ ethanol after centrifugation.)

To extract the surfactant (CTAB) and TMB, we suspend the particles in ethanol (approximately one batch in 80 mL ethanol) and add 10 mL concentrated hydrochloride acid. Refluxing the mixture for one hour. This process is done twice to fully remove the CTAB. After this step, particles are washed and suspended in ethanol for storage/ later use.

Large pore radial-pore MSNs derivative

In a typical synthesis for MSNs with radial pore structures, 100mg CTAB is dissolved in 25 mL of DI water in a 100mL round bottom flask. 112 µL NH_4Cl (with a concentration prepared as 100mg/mL) is added to the mixture together with an addition of 50 µL sodium hydroxide solution (1M). After everything is dissolved, 457 µL TMB is added and again the mixture is sonicated at same condition for 1 hour. Meanwhile, an oil bath at 83˚C is

prepared and stabilized. After the sonication, the flask is transferred to the oil bath and kept waiting for approximately 15 minute for temperature equilibrium. After this, 375 µL TEOS is added to the solution rapidly. The reaction is kept at this temperature for 2 and a half hours. Afterwards, the product is collected in a same manner as described in the previous procedure. CTAB is removed as described above. This type of particles was having radial pore structures that is different from the above mentioned MCM-41 like ones.

Synthesis of Fe_3O_4@SiO_2 core-shell particles with enlarged pore size in emulsion

Typically, 25mg CTAB is dissolved in 10 mL DI water in a 50 mL round bottom flask. 0.75g iron oxide nanoparticles (with a concentration of 7.5 mg/mL dispersed in chloroform) is then added on a balance to the round bottom flask. The mixture is sonicated in a water bath for 10 min and then manually shaken in an oil bath at 70°C for 10 min to evaporate the chloroform, forming a brownish transparent solution. 0.0125g Arginine is then added to the mixture solution. After everything is dissolved, 114 µL TMB is added and the mixture is sonicated at the same condition for 1 hour. Eventually the sonicated mixture in an emulsion form is transferred back to the oil bath at 70°C and stabilize for 15 min before adding in 100 µL TEOS and kept at this temperature for a 3-hour reaction. As synthesized particles are collected and washed with CTAB removal as described before.

Physicochemical characterization of synthesized large pore MSNs/ core-shell particles

As synthesized pore enlarged MSNs were characterized for hydrodynamic sizes, zeta potentials, and morphologies respectively. The shapes and porous structures were characterized using transmission electron microscopy (JEOL JEM 2010, JEOL USA, Inc.,

Peabody, MA). The nanoparticle sizes and zeta potentials in pure water were measured by ZetaSizer Nano (Malvern Instruments Ltd., Worcestershire, UK). Nitrogen gas adsorption/ desorption analysis was performed on an Autosorb-iQ (Quantachrome Instruments) with the temperature of 77 K. All of the measurements were performed with the nanoparticles suspended in filtered water or filtered cell culture media at 40 μg mL^{-1} nanoparticle concentration.

6.4 Results and discussion

Different type of MSNs with enlarged pore size were synthesized based on proposed particle formation mechanisms.[11] In general, tetraethyl orthosilicate (TEOS) was used as a silica source, surfactant cetyltrimethylammonium bromide (CTAB) was the structure directing agent for all types of MSNs; Different base catalysts in various amount were used and effect on pore enlargement from changing reaction pH condition was studied. The amount and combination of swelling agent: 1,3,5-trimethylbenzene (TMB) together with decane was utilized at given conditions for pore swelling.[18] A sonication process was introduced and the effect with or without the presence of sonication treatment on pore expansion was investigated. Parameters and different reaction conditions were listed in table 6.1. and will be further discussed in the later section.

The synthesis and characterization on different types of MSNs with enlarged pore size without sonication

As discussed in previous literatures[11], a proposed pore swelling process was illustrated in Figure 6.1., where before the TEOS hydrolysis and condensation process, the template

agent, CTAB, forming micelles in the aqueous environment with its hydrophilic head (charged ammonium group) pointing outward to the aqueous and the long hydrophobic alkyl chain packed and facing away from aqueous, forming the core of the micelle. The swelling agent, such as trimethylbenzene or decane, is essentially hydrophobic small molecules, that once added to the CTAB aqueous solution, would be energetically favored to enter the core region of the CTAB micelles, thus enlarging the overall size of the micelle which would lead to pore size enlargement. The incorporation of swelling agent into the aqueous micelle solution normally involved intensive stirring process to facilitate the mixing.[11,15,19] Furthermore, a relevant swelling mechanism involving the incorporation of double swelling agents of TMB and decane can be explained in Figure 6.2.[18] TMB molecules can interact with surfactant through electrostatic interactions between the π electrons of the benzene core and the positively charged head group of CTAB. As a result, TMB molecules would be stabilized at the outer surface micelles and hinders further incorporation of other swelling agent molecules. This was the primary reason why double swelling agent method was introduced, and might also be one possible explanation for the solubility limit of TMB in CTAB micelles.

TEM images for the as-synthesized particles are shown as follows for each trial condition in Figure 6.4. to Figure 6.6. The particle diameter and pore size estimated from the TEM image were also reported accordingly. Initially, the reaction temperature was kept at 80 degrees, while the ratio between swelling agent and CTAB was increased. A double swelling agent method was also applied according to a previous report[18] as discussed earlier. From the TEM images, overall morphology and particle size can be characterized. Meanwhile, the pore size appeared to be enlarged with increasing swelling agent amount,

yet the result is inconclusive since the swelling effect was not happening to all micelles. Therefore, SAXS measurement was performed, which as a facile and quick technique comparing to BET measurement, can provide the repeating distance of pored diameter plus pore wall thickness.[1] Namely, a typical SAXS scan was employed through an incident angle from 0 to 5 degrees, where mesostructure of the sample can be revealed. In addition to the d spacing, the packing order can also be obtained from the diffraction pattern. As shown in Figure 6.7., the diffraction pattern for sample NaOH-1-6-80 was a typical shape that can be assigned to a 2D hexagonal structure, with each peak corresponding to d_{10}, d_{11} and d_{20}, respectively. This is a typical SAXS pattern for MCM-41s, while as for other synthesis conditions, the two satellite peaks become shoulder-like or even disappeared, which indicated a loss of the structural ordering. Result of SAXS measurement will be shown and compared at the end of each synthesis conditions.

It was reported that temperature also played an important role for the swelling effect, specifically at low temperature, swelling would be more obvious.[11] The reason was attributed to an increased solubility of swelling agent into the micelle. In detail, at high temperature, the micelles become more loosely packed, thus the accommodation of swelling agent is not secured. The effect of temperature was discussed with a comparison between S4 and S5. The pore size seemed to be enlarged at a lower temperature, while a surprisingly better size distribution was achieved at the same time. Meanwhile, the ordering of the structure was partially lost for a lower temperature reaction, which can be explained as a result of the reduced condensation rate. With further increased TMB added, the size distribution was even bigger, while the size of pores changed little, comparatively. As expected, the disturbance of synthesis from swelling agent became

more severe beyond a SA to CTAB ratio of 8. The SAXS patterns of all samples were collected and shown in Figure. 6.7. The shift of d_{10} peak can be clearly seen to a lower angle, indicating an enlarged repeating distance between the mesopores. A maximum shift was achieved with sample S4 (1-8TMB), as d_{10} was increased from 4.1452 nm for sample without SA (Figure 6.4.) to 4.964 nm for S4. It was noticed that when comparing peaks of raw data together, the peak of S4 seemed to be a broaden peak, while when plotted out individually, a more obvious peak can be obtained. (Figure. 6.4. (b) (d)) The broadening might be due to a broad distribution of the pore size for this sample since pores are not evenly enlarged with the swelling agent. Meanwhile, the swelling effect for S5 (1-12TMB) came out not as large as S4, which might be explained as, with this high amount of SA added, phase separation between TMB and water happened, or the solubility limit of TMB in CTAB micelle was reached. This experimentally supported as after even 3 hours of equilibration, TMB oil phase was still observed in the aqueous solution. This phase separation would also induce a large size distribution of particles since the oil droplets can act as nucleation centers for the growth of silica, which was supported by the TEM images.

TEM images combined with result from SAXS measurement indicated that the swelling effect was not quite obvious with this synthesis condition, even a shift of the d_{10} peaks and enlargement of some pores under TEM were observed. Therefore, another synthesis system was chosen with NH_4OH as the catalyst instead of NaOH, where a lower condensation rate of silica was expected. A typical synthesis route was similar to that with NaOH, while a different molar ratio between the reactants was used according to the literature. (1.0 CTAB: 32.8 NH_3: 3.0 TMB: 9.0 decane: 5.5 TEOS: 491.7 EG: 6938.9

H_2O).[20] Notice that ethylene glycol was used and mixed into the aqueous solution before the addition of swelling agents, the function of which was to gain a better dispersity and a more round-shaped morphology of particles by increasing the viscosity of solution. The samples were labelled in the same fashion as N#-NH_4OH-1-x-T, and TEM images of

From the ammonium hydroxide synthesis system, large pore MSNs were obtained and visualized under TEM (in Figure 6.5. for sample N1-N6). The largest size of pores was achieved with sample N5, where a double-swelling agent strategy was applied. Comparing different synthesis conditions here, it can be seen that with the increasing ratio between SA to CTAB, the pore structure was swelled up from not-barely seen to a really opened-up fashion. When added 12 times of TMB, the pore structure was again severely disturbed (N4). No obvious 2D hexagonal ordering can be observed from SAXS or TEM, thus direct comparison between NH_4OH samples to NaOH samples was not proper besides a different condensation rate in the reaction. For sample N5 and N6, a different adding sequence of swelling agents was applied, while a quite deviated swelling effect can be observed. The effect of adding sequence of swelling agent was explained as the steric hindrance of TMB molecules. A proposed mechanism was illustrated in Figure. 6.2.[18] TMB molecules can interact with surfactant through electrostatic interactions between the π electrons of the benzene core and the positively charged head group of CTAB. As a result, TMB molecules would be stabilized at the outer surface micelles and hinders further incorporation of other swelling agent molecules. This was the primary reason why double swelling agent method was introduced, and might also be one possible explanation for the solubility limit of TMB in CTAB micelles.

As shown in Figure 6.7., it was a little difficult to see clear peaks for some of the samples with increasing pore sizes. Ideally, the diffraction peaks should be superimposed on the background. While for the samples of this synthesis condition, the scattering curve became shoulder-like shape with no obvious peaks. As for some samples that were expected to have large pores, only a change of intensity was observed when curve was compared to that of the sample holder. It can be speculated that the well-ordered hexagonal packing of micelles was gone, where micelles were more loosely packed. Meanwhile, the size of particle is smaller, especially comparing to the size of the pore, which indicated that less repeating distance was found in one-unit cell of nanoparticle. Or, for sample N5, the peak (or shoulder) was further shifted to a lower angle into the background. Therefore, BET measurement was performed so as to get a better idea of those samples that didn't show a clear "peak position" in the SAXS. (The result of BET will be included and discussed together with the core-shell section.) The overall morphology of the MSNs was not as good as that with the NaOH base, as smaller particles with crosslinking to different extents were synthesized. Ethyl acetate was introduced to this system with the purpose of reducing the crosslinking, yet no obvious effect was observed. Further efforts would be expected to modify the morphology of the particles, especially as for preparation of *in vivo* study, where crosslinking of particle might induce aggregation of particles in circulation system.[21]

Synthesis and Characterization of iron oxide MSN Core-shell composite

The synthesis method of iron oxide core/shell structure is based on the synthesis of MCM 41 and a typical synthesis protocol is described in the experimental section. Sample for

the core-shell study was labelled as CS# arginine/NH_4OH-1-x-T, the TEM images of which are presented in below.

As shown in TEM images in figure 6.6., the overall morphology and dispersity for sample CS1–CS5 can be well maintained in the core-shell system even with high amount of swelling agent involved in the system. It was not surprising for this different behavior comparing to the previous plain MSNs case. Since the iron oxide NCs would serve as nucleation centers for the further condensation of silica, the growth mechanism was believed to be quite different from that of plain silica. Inspired by the plain silica study, the type of base catalyst was changed to ammonium hydroxide. Similar spherical particles were obtained, while the pore structure was slightly different as more of a radial channel-like morphology was obtained with NH_4OH comparing to a “wormlike” pore structure for the arginine case. It seemed that more swelling agent could be employed since the structure of particle was well maintained. The SAXS data showed a shift of the d_{10} peak to a lower angle, and the BET measurement proved a maximum enlargement from CS3 of 3.78 nm, which was a 40% increment in size comparing to a reported 2.7 nm size for normal Fe_3O_4@silica composite.

To briefly sum up, we found in the previous reaction conditions, with higher reaction pH (NaOH over NH_4OH), the pore structure was more regulated and well-defined, yet the swelling agent tend to enter the micelles more easily as they are more loosely packed in at lower synthesis pH condition. Temperature played an important role as it affected the packing of the micelle as well as the hydrolysis and condensation rate of TEOS, leading to a better pore expansion performance at relatively lower reaction temperature. However, from previous experiments, the simple mixing by stirring provided a rather

passive way for the swelling agents to reach the core of micelles in aqueous solution and thus resulting in less control over the synthesis and might lead to aggregated nanoparticle formation and inconsistent pore enlargement.

The synthesis and characterization on different types of MSNs having enlarged pore size with sonication

Recent publications proposed an emulsion-assisted pore expanding synthesis, the proposed mechanism is illustrated in Figure 6.3.[22], where the silica source molecule 1,4-bis(triethoxysilyl)benzene (BTEB) gradually diffuse into the aqueous phase from the oil phase, leading to lower concentration of hydrolyzed organosilica species that slowed down the overall condensation rate. This is crucial for the formation of pore enlarged MSNs, because if the condensation rate is higher as shown in Figure 6.3. (d), where the initial concentration of BTEB is higher, then dense organosilica formed instead of enlarged mesoporous structure. Yet, this process required a 72-hour stabilization step with very specific stirring speed. Herein, we proposed a facile and highly reproducible synthesis method, utilizing a water bath sonication process to generate stable emulsion of the oil in water, swelling agent (TMB) in CTAB aqueous solution system. A similar process of hydrolysis and condensation of TEOS happened at the interface of the emulsion and facilitated the formation of MSNs with enlarged pore size. Parameters of reaction pH condition, reaction temperature and amount of swelling agent added in the system are also investigated for their effects on the overall morphology of the MSNs and enlarged pore formation. By varying those parameters, we realized the control of particle size and pore size with monodisperse and uniform particle morphology.

Three different types of mesoporous silica nanoparticles were synthesized according to the experimental section, namely, pore expanded MSNs of MCM-41 type, MSN-b with radial pore structure and Fe3O4@MSNs core-shell particles. In Figure 6.8., TEM images of those three types with or without the addition of swelling agent and pore expansion process. It is clear as shown in the images that the pore size was enlarged while the particle morphology was maintained as uniform spheres (a TMB/CTAB molar ratio of 12:1). When looking back at table 7.1., by comparing the base catalyst used for MCM-41 type and MSN-b both with sonication process, the TEM images of both particles with same TMB/CTAB ratio (12:1) showed different pore structures. (Figure 6.9.) The pore channels were almost 2D hexagonally packed within the MCM-41 type while pores were radial-like for MSN-b type with bigger pore openings at the end of pore channels. This can be explained that for the synthesis of MSN-b, the pH of the reaction was buffered by the addition of NH_4Cl, thus the packing of micelle was weaker than the NaOH counterpart, so as a slower hydrolysis and condensation rate. Therefore, for the higher pH condition for the MCM-41 type, the 2D hexagonal pore structure was maintained, while the morphology of the MSN-b type was more monodisperse and uniformly spherical. The temperature effect on the synthesis and pore swelling process was investigated with a varying waiting time after the sonication before the addition of TEOS. The temperature of the emulsion was approximately 40°C and the oil bath was set to 70°C. The exact reaction temperature was not monitored as the addition of TEOS will introduce a temperature drop, but the increasing waiting time before the addition of TEOS would lead to an increasing reaction temperature. The size of the nanoparticle ranged from 80-90 nm to 50-60 nm as the waiting time ranged from 30 min to 10 min, whereas the pore size of the MSNs almost

remained unchanged. This indicated that temperature was not the determining factor for pore expansion yet affecting the overall size of the synthesized nanoparticles. The necessity of the sonication process and the amount of TMB needed for the reaction was studied, with TEM images of MSNs synthesized at those different conditions illustrated in figure 6.10. As shown in this figure, without the sonication process with a TMB/CTAB ratio of 12:1, or with the sonication process but with a TMB/CTAB ratio of 4:1, no pore expansion was observed. This indicates that it was crucial to have the sonication process with enough amount of TMB as the oil phase introduced into the CTAB aqueous solution, in another word, the formation of the emulsion is necessary for the formation of the pore enlarged MSNs. This pore expansion method was then applied to the Fe_3O_4@MSNs where the sonication treatment was again introduced after adding the TMB into the CTAB solution for emulsion formation. Similarly, as the base catalyst used in the reaction is arginine which was a rather weak organic base, and it would hydrolyze into a pH buffer form, the rate of the TEOS condensation was therefore regulated and a similar radial pore structure was formed. Comparing to previous experiments with change of swelling agent of TMB and decane but no sonication and emulsion-assisted process, the later pore expansion phenomenon was more obvious with the sonication process, giving a pore size of 6.8 nm over 3.8 nm after pore enlargement.

6.5 Conclusion

The delivery or accommodation of large molecules such as gene, enzyme/protein or drug molecules that are large in size could be essential for various kinds of biological applications.[23–27] Research had been done on the synthesis and possible mechanism of

mesoporous silica or derivatives with enlarged mesopores size.[28,29] Previous synthesis routes have been revisited in this work, finding that previous methods are often tedious and time consuming, or difficult to reproduce. Herein, we described a facile and highly reproducible synthesis method for making various types of MSNs with different pore structures or for different application. The effects of swelling agent usage, reaction pH and temperature conditions and the effect of sonification or emulsion formation process were investigated, which enabled us to control the pore size and particle morphology. This facile and highly reproducible synthesis method produced MSNs ranged from 50-90 nm and with typical pore size from 3 to 8 nm. Currently, this novel technique is utilized to synthesis large pore MSNs for enzyme trapping for sensor applications and could be promising for various of biological applications related to large molecule like protein or enzyme accommodation.[30]

6.6 Tables and figures

Type of MSNs	Base catalyst used	Typical pore structure	Swelling agent used	Presence of sonication process	Effect of increasing SA:CTAB ratio
MCM-41	NaOH (2M)	2D Hexagonal packed channels	TMB, TMB + decane	W/ WO	Pore size increase from ratio 12:1 to 16:1, particle morphology is disturbed at high ratio
MSN-a	NH_4OH	Radial/ random	TMB, TMB + decane	WO	Pore size increase from ratio 12:1 to 16:1, particle morphology is disturbed at high ratio
MSN-b	NaOH (1M) plus NH_4Cl	Radial	TMB	W/ WO	Pore size increase with increasing ratio
Fe_3O_4@MSN	Arginine	Radial	TMB	W	Pore size increase with increasing ratio

Table 6.1. Summary of parameters investigated for the synthesis of pore enlarged MSNs.

Sample ID	d spacing (nm)	Pore size by BJH (nm)	Surface Area (m2/g)
CS2-1-6	6.0433	3.78	912.760
CS5-1-9+3	5.5077	3.24	972.959
N5-1-9+3	NA	5.16	553.1

Table 6.2. BET and SAXS data summary for samples with most obvious swelling effect

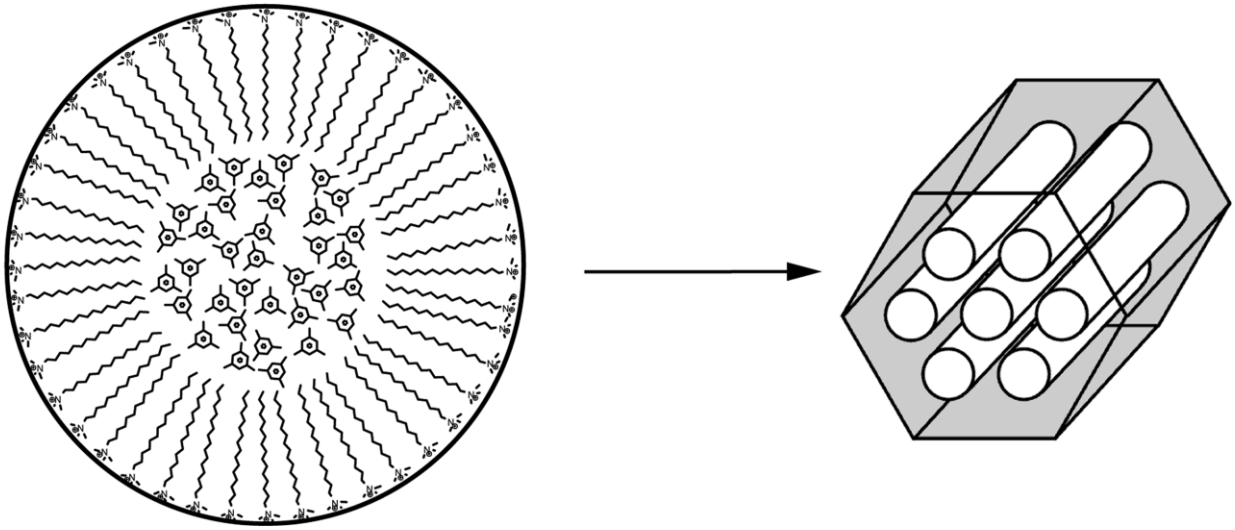

Figure 6.1. Schematics of micelle swelling with trimethylbenzene (TMB)[11]

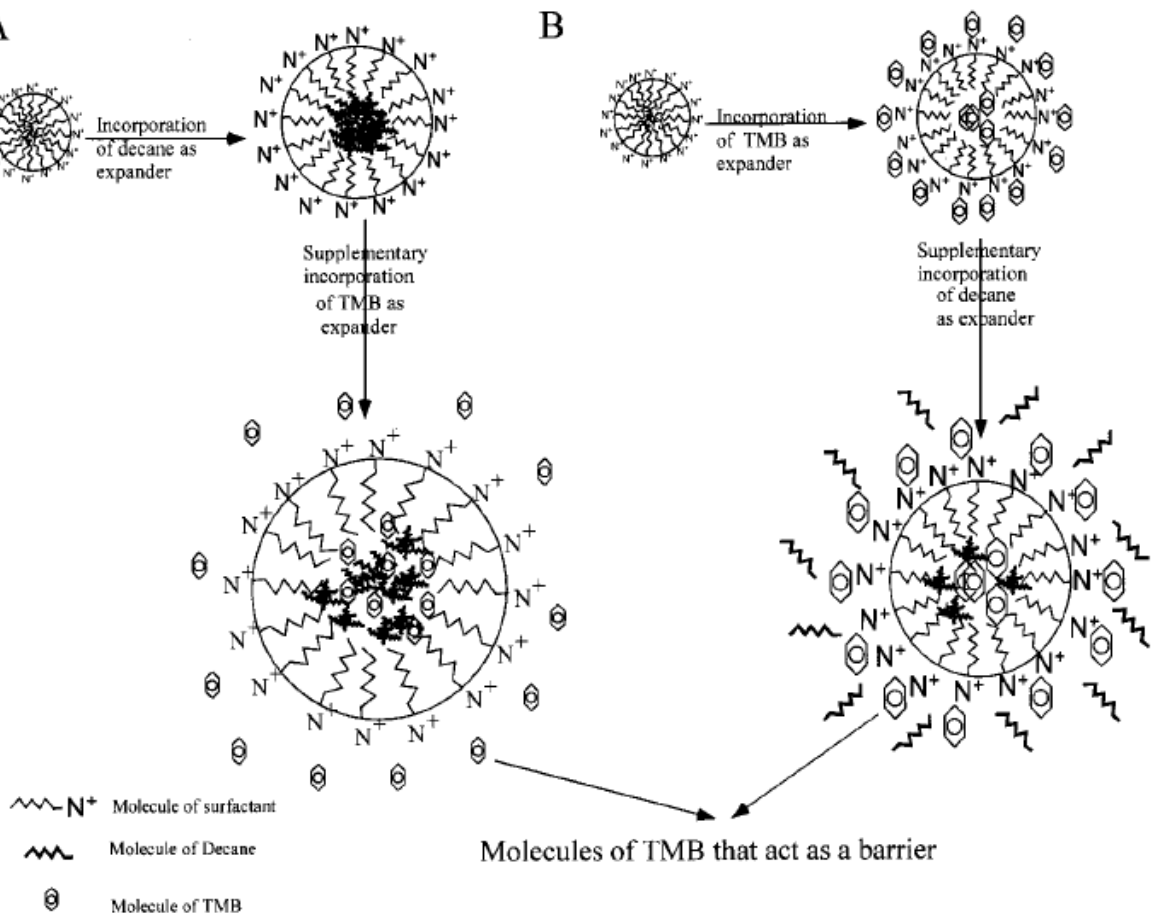

Figure 6.2. Possible mechanism for the incorporation of decane and TMB into micelles: (A) decane added before TMB (B) decane added after TMB[18]

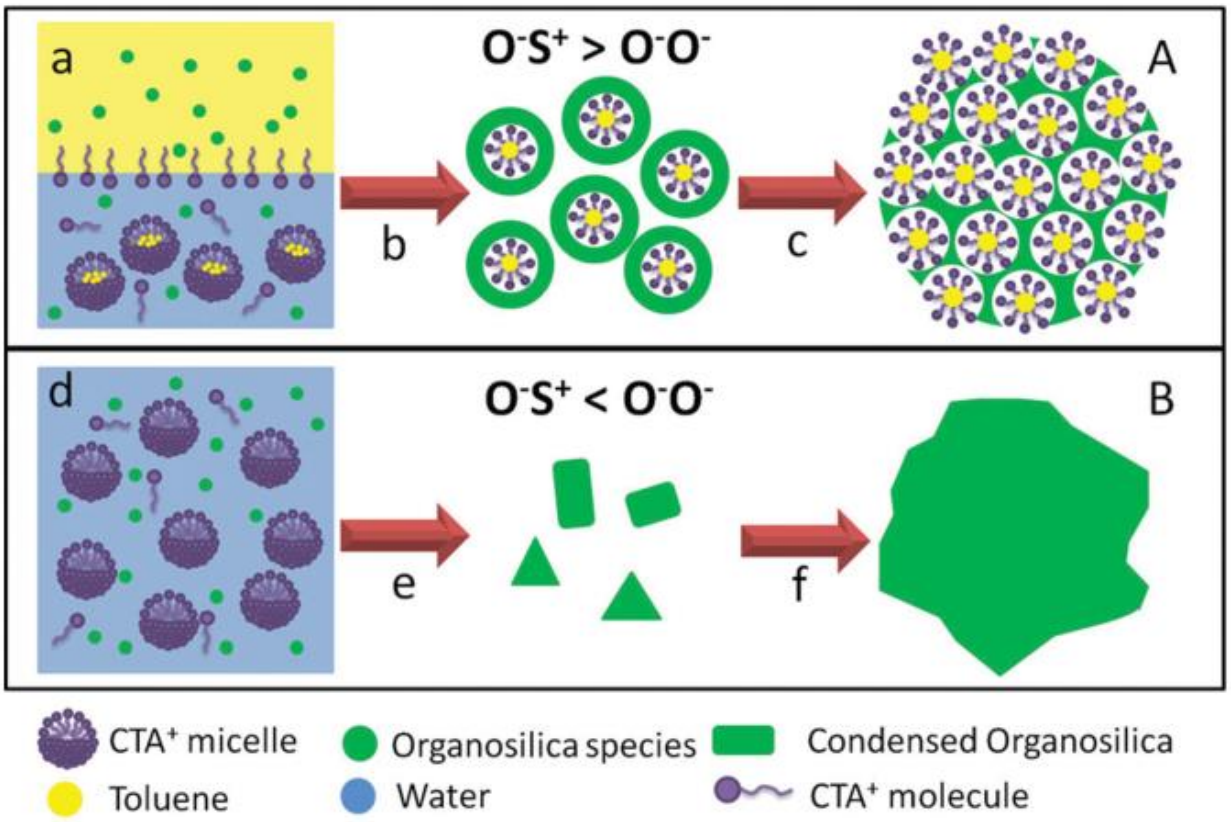

Figure 6.3. Scheme of synthesis mechanism for oil-water phase assisted synthesis of large pore MSNs.[22]

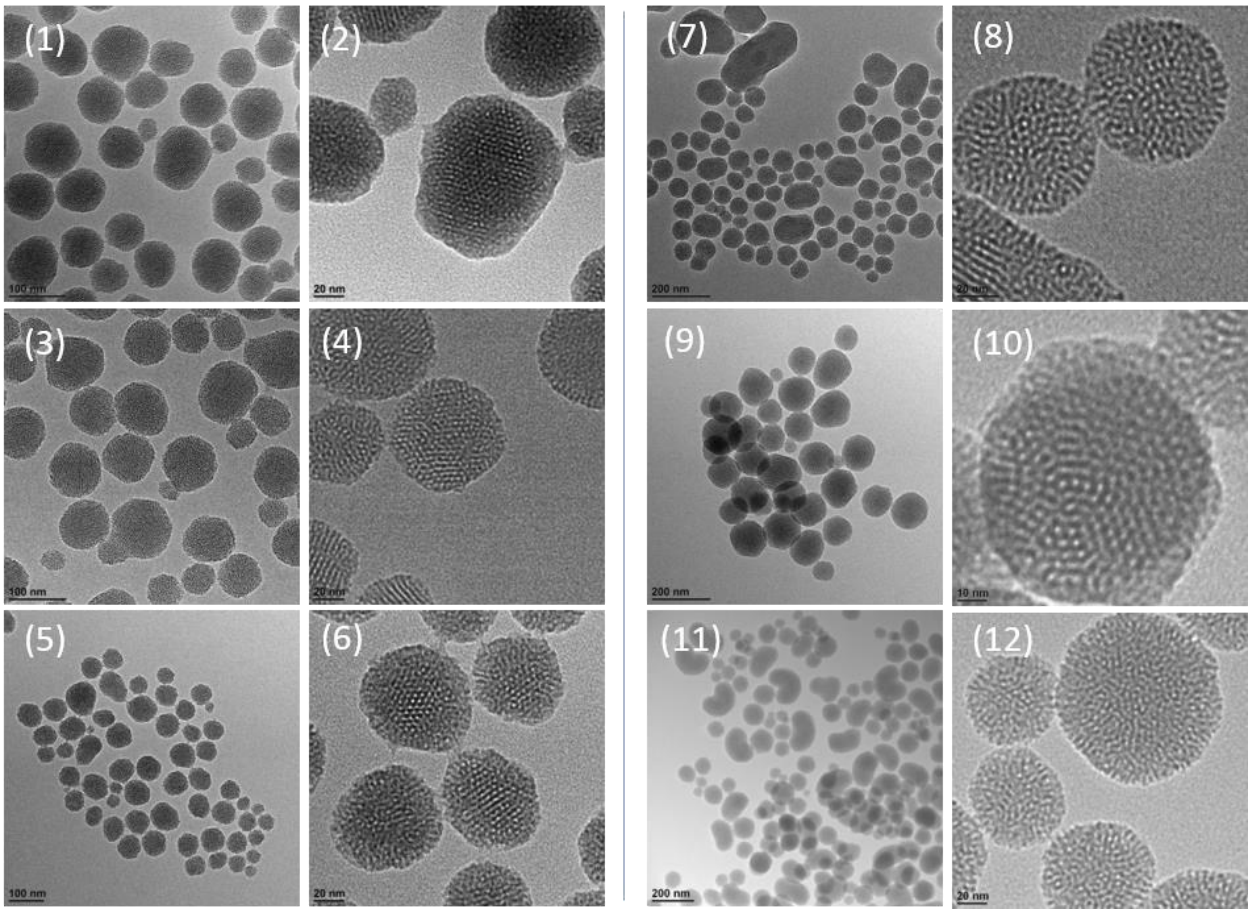

Figure 6.4. TEM images of S1-S6. (1) (2), S1: NaOH-1-4TMB-80, D= 80±10 nm, Pore= ~2.82 nm. (3) (4), S2: NaOH-1-6TMB-80, D= 90±10 nm, Pore= (1.8+3.2)/2=2.5 nm. (5) (6), S3: NaOH-1-3decane+3TMB-80, D= 60±10 nm, Pore= ~2.7 nm. (7) (8), S4: NaOH-1-8TMB-80, D= ~70 nm with large particles, Pore= 3.0-3.3 nm. (9) (10), S5: NaOH-1-8TMB-70, D= ~100 nm medium size distribution, Pore= 3.0-3.6 nm. (11) (12), S6: NaOH-1-12TMB-70, D= wide size distribution, Pore= 2.5-4.0 nm.

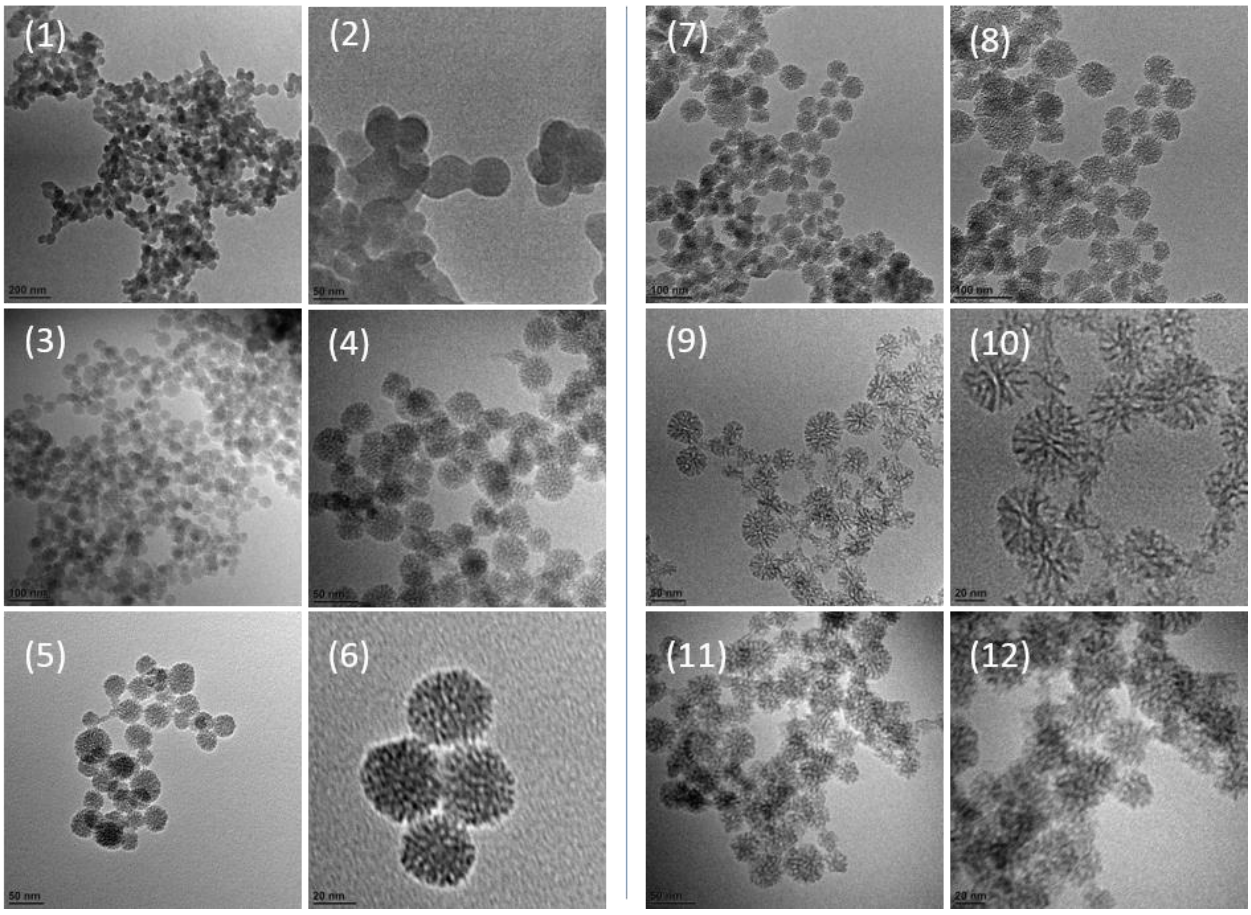

Figure 6.5. TEM images of N1-N6. (1) (2), N1: NH_4OH-1-0-70, D= ~58 nm crosslinking, Pore= NA. (3) (4), N2: NH_4OH-1-8decane-70, D= ~58 nm crosslinking, Pore= ~3.6 nm. (5) (6), N3: NH_4OH-1-8TMB-70, D= ~38 nm crosslinking, Pore= 2.8-3.7 nm. (7) (8), N4: NH_4OH-1-12TMB-70, D= ~50 nm crosslinking and large particle, Pore= ~4.2 nm and open structure. (9) (10), N5: NH_4OH-1-9decane+3TMB-70, D= ~50 nm crosslinking and minor size distribution, Pore= 3.8-6.6 nm. (11) (12), N6 NH_4OH-1-3TMB+9decane-70, D= ~40 nm crosslinking, Pore= 3.3-4.6 nm.

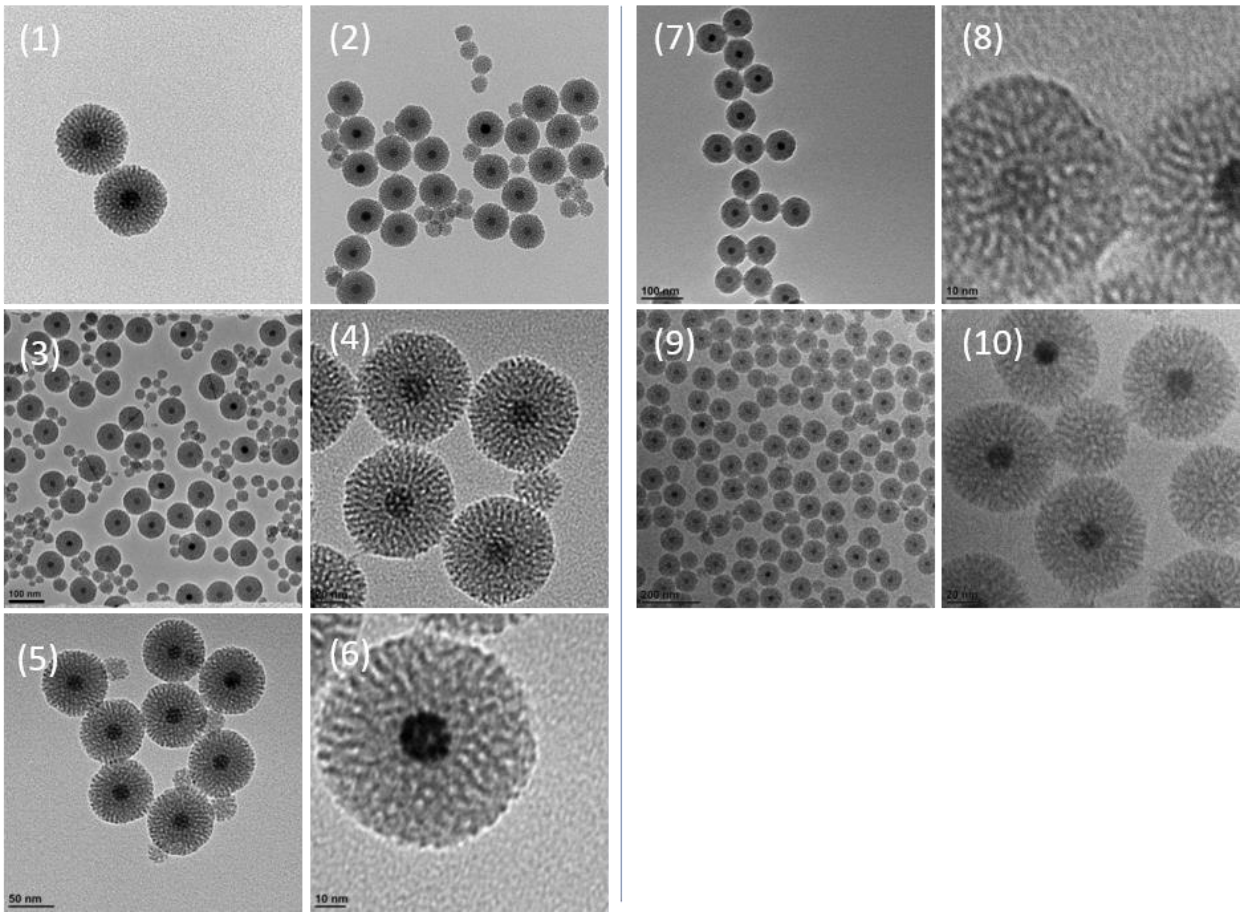

Figure 6.6. TEM images of CS1-CS5. (1) (2), CS1: arginine-1-0-70, D= 70±5 nm, Pore= ~2.7 nm. (3) (4), CS2: arginine-1-4TMB-70, D= 70±5 nm, Pore= 2.8-3.7 nm. (5) (6), CS3: arginine-1-6TMB-70, D= 75±5 nm, Pore= 2.8-3.7 nm. (7) (8), CS4: arginine-1-9decane+3TMB-70, D= 70±5 nm, Pore= 3.6-4 nm. (9) (10), CS5: NH_4OH-9decane+3TMB-70, D= 70-80 nm, Pore=2.2*~5 nm

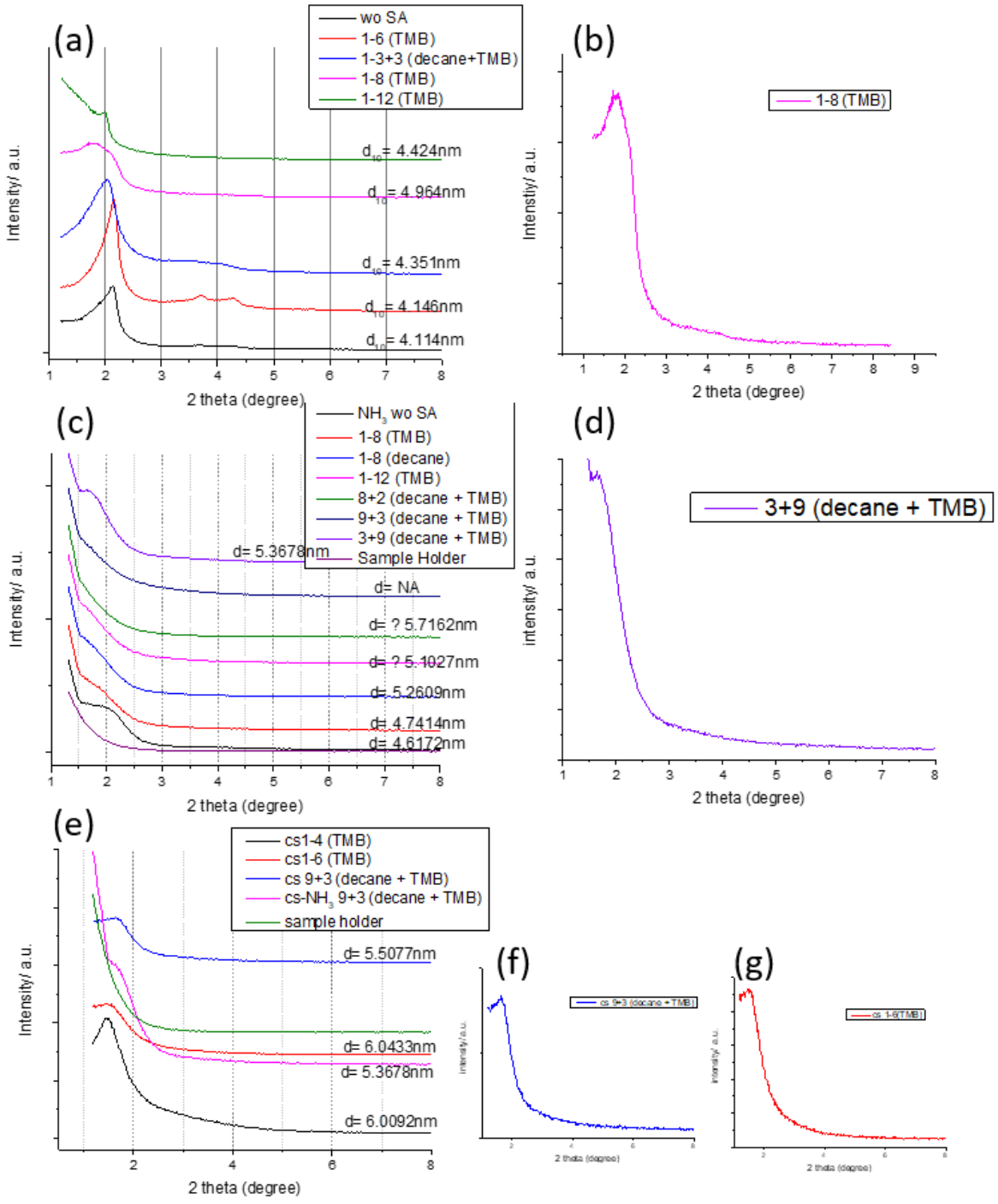

Figure 6.7. SAXS measurement for MSNs synthesized with different bases: (a),(b) with NaOH, (c),(d) with NH3H2O, (e)-(g) for core-shell samples

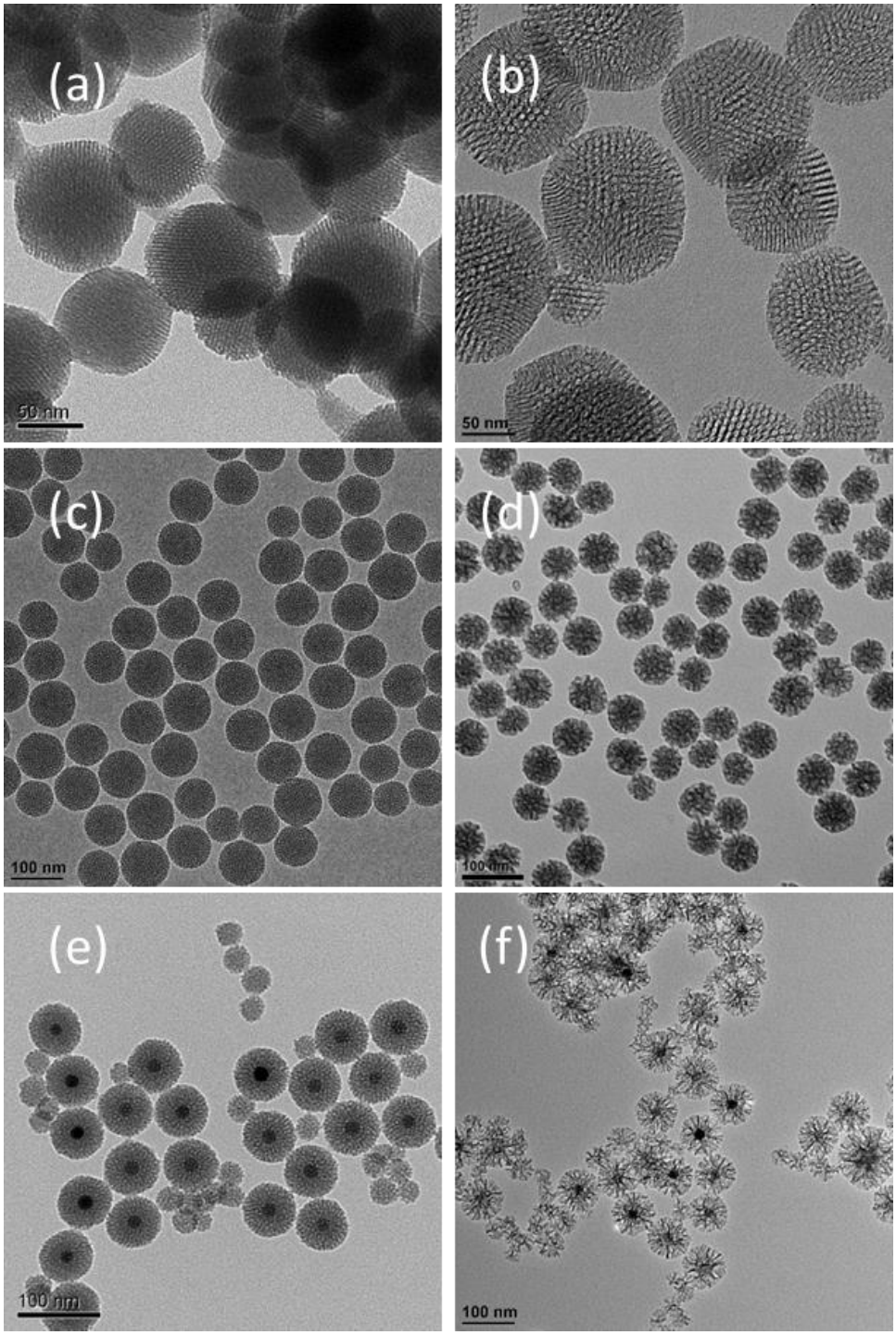

Figure 6.8. TEM images of three different types of MSNs with/ without pore enlargement. (a), (b): MCM-41 with cylindrical pore structures; (c), (d): MSNs with radial pore structures; (e), (f): Fe3O4@MSN core-shell structures with radial pores.

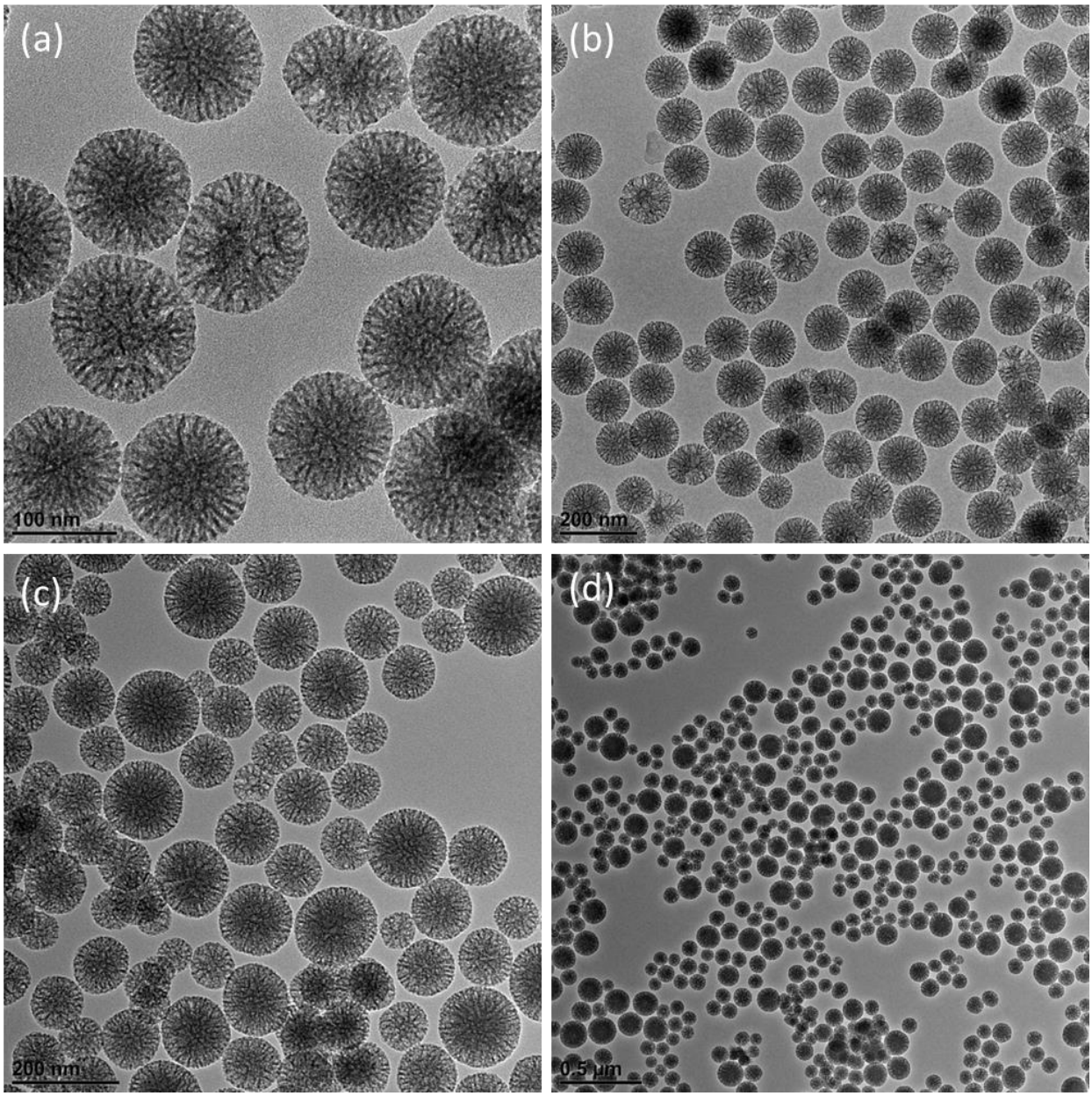

Figure 6.9. TEM images of radial MSNs with addition of different amount of swelling agent. molar ratio between TMB/CTAB is 12:1 for (a), (b) and 16:1 for (c), (d), respectively.

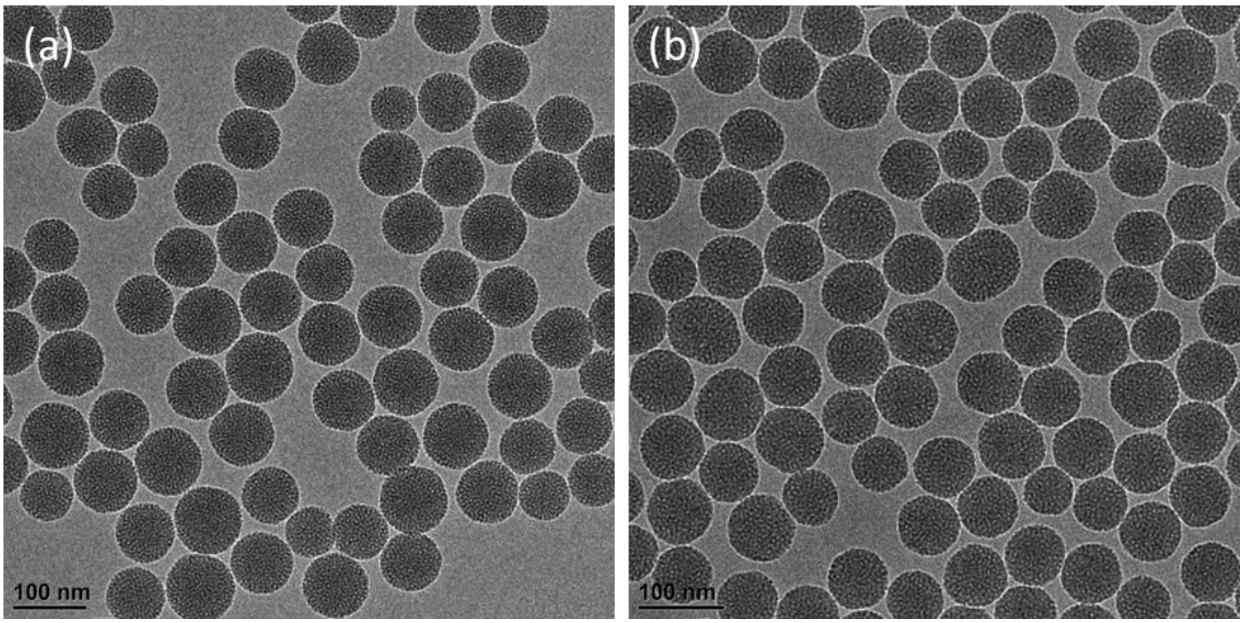

Figure 6.10. TEM images radial MSNs, (a) adding 12:1 TMB/CTAB but without sonication; (b) with sonication process and adding 4:1 TMB/CTAB.

6.7 References

1. Firouzi, A. *et al.* Cooperative organization of inorganic-surfactant and biomimetic assemblies. *Science (80-.).* **267**, 1138 LP – 1143 (1995).
2. Brinker, C. J. & Scherer, G. W. *Sol-gel science: the physics and chemistry of sol-gel processing*. (Academic press, 2013).
3. Grün, M., Lauer, I. & Unger, K. K. The synthesis of micrometer-and submicrometer-size spheres of ordered mesoporous oxide MCM-41. *Adv. Mater.* **9**, 254–257 (1997).
4. Stöber, W., Fink, A. & Bohn, E. Controlled growth of monodisperse silica spheres in the micron size range. *J. Colloid Interface Sci.* **26**, 62–69 (1968).
5. Li, Z., Barnes, J. C., Bosoy, A., Stoddart, J. F. & Zink, J. I. Mesoporous silica nanoparticles in biomedical applications. *Chem. Soc. Rev.* **41**, 2590–2605 (2012).
6. Li, X. *et al.* A mesoporous silica nanoparticle – PEI – Fusogenic peptide system for siRNA delivery in cancer therapy. *Biomaterials* **34**, 1391–1401 (2013).
7. Li, X., Xie, Q. R., Zhang, J., Xia, W. & Gu, H. The packaging of siRNA within the mesoporous structure of silica nanoparticles. *Biomaterials* **32**, 9546–9556 (2011).
8. Malmsten, M. Inorganic nanomaterials as delivery systems for proteins, peptides, DNA, and siRNA. *Curr. Opin. Colloid Interface Sci.* **18**, 468–480 (2013).
9. Meng, H., Xue, M., Zink, J. I. & Nel, A. E. Development of pharmaceutically adapted mesoporous silica nanoparticles platform. *J. Phys. Chem. Lett.* **3**, 358–359 (2012).
10. Li, J., Wang, Y., Zhu, Y. & Oupický, D. Recent advances in delivery of drug-

nucleic acid combinations for cancer treatment. *J. Control. Release* **172**, 589–600 (2013).

11. Kruk, M. Access to Ultralarge-Pore Ordered Mesoporous Materials through Selection of Surfactant/Swelling-Agent Micellar Templates. *Acc. Chem. Res.* **45**, 1678–1687 (2012).
12. Yang, Y. *et al.* Anion Assisted Synthesis of Large Pore Hollow Dendritic Mesoporous Organosilica Nanoparticles: Understanding the Composition Gradient. *Chem. Mater.* **28**, 704–707 (2016).
13. Roberts, C. M. *et al.* Nanoparticle delivery of siRNA against TWIST to reduce drug resistance and tumor growth in ovarian cancer models. *Nanomedicine Nanotechnology, Biol. Med.* **13**, 965–976 (2017).
14. Hartono, S. B. *et al.* Functionalized large pore mesoporous silica nanoparticles for gene delivery featuring controlled release and co-delivery. *J. Mater. Chem. B* **2**, 718–726 (2014).
15. Knežević, N. & Durand, J. O. Large pore mesoporous silica nanomaterials for application in delivery of biomolecules. *Nanoscale* **7**, 2199–2209 (2015).
16. Xue, M., Cao, D., Stoddart, J. F. & Zink, J. I. Size-selective pH-operated megagates on mesoporous silica materials. *Nanoscale* **4**, 7569–7574 (2012).
17. Blin, J.-L. & Su, B.-L. Tailoring pore size of ordered mesoporous silicas using one or two organic auxiliaries as expanders. *Langmuir* **18**, 5303–5308 (2002).
18. Zhang, J., Li, X., Rosenholm, J. M. & Gu, H. Synthesis and characterization of pore size-tunable magnetic mesoporous silica nanoparticles. *J. Colloid Interface Sci.* **361**, 16–24 (2011).

19. Slowing, I. I., Trewyn, B. G. & Lin, V. S.-Y. Mesoporous silica nanoparticles for intracellular delivery of membrane-impermeable proteins. *J. Am. Chem. Soc.* **129**, 8845–8849 (2007).

20. Zhang, J., Niemelä, M., Westermarck, J. & Rosenholm, J. M. Mesoporous silica nanoparticles with redox-responsive surface linkers for charge-reversible loading and release of short oligonucleotides. *Dalt. Trans.* **43**, 4115–4126 (2014).

21. Sarker, D. K. *Pharmaceutical emulsions: a drug developer's toolbag*. (John Wiley & Sons, 2013).

22. Yang, Y. *et al.* Biphasic Synthesis of Large-Pore and Well-Dispersed Benzene Bridged Mesoporous Organosilica Nanoparticles for Intracellular Protein Delivery. *Small* **11**, 2743–2749 (2015).

23. Al-Dosari, M. S. & Gao, X. Nonviral gene delivery: principle, limitations, and recent progress. *AAPS J.* **11**, 671 (2009).

24. Wiethoff, C. M. & Middaugh, C. R. Barriers to nonviral gene delivery. *J. Pharm. Sci.* **92**, 203–217 (2003).

25. Keles, E., Song, Y., Du, D., Dong, W.-J. & Lin, Y. Recent progress in nanomaterials for gene delivery applications. *Biomater. Sci.* **4**, 1291–1309 (2016).

26. Vaghari, H. *et al.* Application of magnetic nanoparticles in smart enzyme immobilization. *Biotechnol. Lett.* **38**, 223–233 (2016).

27. McClements, D. J. Encapsulation, protection, and delivery of bioactive proteins and peptides using nanoparticle and microparticle systems: A review. *Adv. Colloid Interface Sci.* **253**, 1–22 (2018).

28. Yu, C., Tian, B., Fan, J., Stucky, G. D. & Zhao, D. Nonionic block copolymer

synthesis of large-pore cubic mesoporous single crystals by use of inorganic salts. *J. Am. Chem. Soc.* **124**, 4556–4557 (2002).

29. Wang, Y. *et al.* Small-sized and large-pore dendritic mesoporous silica nanoparticles enhance antimicrobial enzyme delivery. *J. Mater. Chem. B* **4**, 2646–2653 (2016).

30. Yu, Q., Deng, T., Lin, F.-C., Zhang, B. & Zink, J. I. Supramolecular Assemblies of Heterogeneous Mesoporous Silica Nanoparticles to Co-deliver Antimicrobial Peptides and Antibiotics for Synergistic Eradication of Pathogenic Biofilms. *ACS Nano* **14**, 5926–5937 (2020).

Chapter 7

Design and fabrication of thin films with ultra-large mesoporous and macroporous hierarchical structure

7.1 Abstract

Mesoporous silica spheres with ultra large mesopores of 15-20 nm were synthesized using a triblock copolymer as a template. By mixing with micron size polystyrene spheres as sacrificing templates, a thin film with dual pore sizes of 15-20 nm mesopores and 10 um macropores was fabricated. With the addition of TEOS glue solution (acidified TEOS sol solution), the hierarchical structure of the as prepared thin film was maintained without collapsing even with over 550°C calcination. Such dual pore-sized hierarchical structured thin films are ideal as gas absorbents with proper modification of capture chemistry and may show great potential in the field of biosensing, separations and cell engineering.

7.2 Introduction

Over the past few years, novel porous solid structures that were fabricated by self-assembling binary colloidal spheres have attracted much attention worldwide.[1–3] Such often complex structures could be utilized as functional materials for the application of mass separation[4], tissue engineering[5,6], drug delivery[7,8], sensing[9,10] and catalytic reaction[11,12]. Wang and co-workers reported for the first time a three-dimensional structured inverse binary opal fabricated by the self-assemble method.[13,14] However, despite that self-assemble method via colloidal spheres is facile to implement and offer great potential to scale up, there are several limitations associate it as well. Namely, the size of the colloidal building blocks is typically limited to submicron by certain assembling methods; the self-assembly process could be time consuming with days up to months;

and most importantly, the as-formed binary porous structures are often fragile for further tests.[15] Therefore, it is necessary to develop a more rapid and cost-effective and robust self-assemble method for practical applications with the as-assembled porous solid structures.

Herein, a hierarchical porous thin film structure as gas absorbent was proposed and realized via self-assemble method using fine-fixed size mesoporous silica spheres (MSS) and polystyrene spheres (PSS) as illustrated in Figure 1.1. Ultra large pore silica spheres[16] were chosen to fulfill the requirement of accommodating 2-5 nm ultra-small gold nanoparticles[17,18] for gas capturing chemistry, and 10 μm PSS was utilized as sacrificing template to structure the network for passive gas flow as modeled in a separated calculation study. A horizontal deposition self-assemble technique[15] was adapted to realize the rapid and scalable thin film fabrication process. In addition, a solution of acidified TEOS sol was introduced to perform as glue to stabilize the porous solid thin film structure without sacrificing the ultra large mesopores within the MSS building blocks. Such thin film platform will be tested with further infiltration of gold nanoparticles for gas sampling and storage.

7.3 Experimental

Materials

All chemicals are used as purchased without further purification. Potassium sulfate (K_2SO_4, $\geqslant$ 99%), 1,3,5-trimethylbenzene (TMB, 98%), tetraorthoethylsilicate (TEOS, 98%), ammonium fluoride (NH_4F, $\geqslant$ 99%), Pluronic P123 polymer (Mw: 5,800) and

polystyrene microspheres (PSS, 10 μm) were purchased from Sigma (St. Louis, MO). Sulfuric acid (H_2SO_4, ⩾99%) and hydrogen peroxide (H_2O_2, 30% w/w in H_2O) were purchased from Fisher Scientific (Pittsburgh, PA).

Synthesis of ultra large pore mesoporous silica spheres (MSS)

In a typical synthesis of mesoporous silica spheres (MSS), potassium sulfate (K_2SO_4, 3.6 g, 0.02 mol) and Pluronic P123 polymer (2.0 g) were dissolved in DI water (60 mL) mixed with hydrochloride acid (HCl, 37%, 10 mL) in a 250 mL beaker with a 2-inch stir bar kept stirring at 300 rpm for 2 hours at room temperature till the solution is clear. Afterwards, 1,3,5-trimethylbenzene (TMB, 2.32 mL, 15.8 mmol) was added into the mixture with stirring for another 2 hours. Finally, tetraethylorthosilicate (TEOS, 4.61 mL, 20 mmol) was added into the mixture at a rate of 600 μl/min with the stir on via a syringe pump. Another 10min stirring was kept after the TEOS addition was complete. Then, the stir bar was removed and the mixture milky white mixture solution was poured into a 250 mL bottle and kept at room temperature for 24-hour aging. Ammonium fluoride (NH_4F, 24 mg, 0.65 mmol) was dissolved in DI water (2 mL) which was added to the mixture after first 24 hours aging. Then the bottle was transferred to an oven for a further aging process at 100 °C for 72 hours. The final white precipitate was dropped out and washed four times by 50:50 water/ ethanol mixture via centrifugation at 3000 rpm for 5 min. The white sample was then collected and dried in an oven at 100 °C overnight. Finally, the sample as white powders were calcined at 550 °C for 6 hours to remove the polymer template.

Silicon/ glass substrate cleaning and preparation

Silicon wafer was cut into 1.5 × 1.5 cm^2 pieces as working substrates. Glass substrate was prepared by cutting microscope slide into 2.5 × 2.5 cm^2 pieces. The substrates were first rinsed and cleaned in ethanol by sonication in water bath for 30 min. Then the substrates were dried and soaked in fresh prepared piranha solution for 2 hours to clean extra organic residuals on the surface. Finally, the Si/ glass substrates were rinsed with water and ethanol then blow dried with N_2 gas and placed in a sample petri dish before further coating.

Fabrication of thin film of MSS and polystyrene spheres (PSS) on silicon substrate

The as-cleaned Si/ glass substrate in sample petri dish was transferred to a desiccator. Onto the substrate, a mixture of MSS and PSS (with weight ratio of 1:1, 1:2 and 1:4) well dispersed in 50:50 water/ ethanol solvent was evenly drop casted by a 100 mL micropipette for 60 µl × 3 times. Then the film was allowed to dry-out overnight for solvent evaporation.

Layer-by-layer deposition of MSS-PS films

The as-cleaned Si/ glass substrate in petri dish was placed in a desiccator. An initial layer of MSS (25 mg) in 50:50 water/ ethanol solution (1 mL) was drop casted by a 100 mL micropipette for 60 µL × 3 times. (denoted as MSS layer) The film was allowed to dry out overnight then transferred to an oven and aging at 300 °C for 3 hours. After the thermal treatment, the film was cooled to room temperature then transferred back to the desiccator. A first layer of MSS-PSS mixture was formed by drop casting a 50:50 water/ ethanol suspension (60 µL × 3 times) of MSS-PSS (50 mg/ 50 mg) with a 100 mL micropipette onto the film. (denoted as MSS-PSS layer) After drying out the previous

layer, a 2nd layer and 3rd layer of MSS-PSS mixture was formed by repeating the drop casting process as described above. Finally, the film was placed in an oven at 550 °C for 6 hours to remove the PSS template.

Prepare and addition of TEOS precursor solution to regulate macro-pores within the film

The TEOS sol solution (TEOS glue) was prepared by mixing tetraethylorthosilicate (TEOS, 90%, 1 mL), DI water (1 mL) and hydrochloride (HCl, 73 µL), then this sol solution was further diluted with methanol (8 mL). The TEOS sol solution was introduced into the film structure by completely soaking each formed layer of MSS-PSS mixture with the TEOS glue (60 µL, 3 times), then drying out the glue in desiccator before next layer deposition.

Physicochemical characterization of synthesized MSS and as-prepared films

The structure of ground/ unground MSS powders were characterized using transmission electron microscopy (JEOL JEM 2010, JEOL USA, Inc., Peabody, MA). The morphology of as-synthesized films was characterized using Scanning Electron Microscope (JEOL model 6700, JEOL USA, Inc., Peabody, MA). Nitrogen gas adsorption/ desorption analysis was performed on an Autosorb-iQ (Quantachrome Instruments) with the temperature of 77 K. The samples for the gas adsorption/ desorption analysis were prepared as described before, as for MSS films was prepared by only depositing solution of only MSS at a concentration of 100 mg/mL; while more or less TEOS samples were prepared by using 60 µL or 20 µL TEOS glue per layer, respectively.

7.4 Results and discussion

A hierarchical structured film device was proposed as illustrated in schematic figure 7.1. The substrate was either silicon or glass. The primary particles within the film was a type of mesoporous silica spheres (MSS) that had a diameter of around 2-3 um. Those particles possessed ultra large pores that were template by a specific block copolymer P123. The ultra large pores would serve as host for active materials such as 2-5 nm gold nanoparticles or other organic moieties as gas capturing agent.[17,18] Besides the primary silica particles, there were 10 um macropores interconnecting throughout the whole film that were template by polystyrene spheres (PSS). Those macropores would serve as gas flow channels that could potentially benefit the gas absorbing property. The PSS templates were removed by calcination as depicted in figure 7.1. (B) and (C) as before and after calcination. To enhance the mechanical property of this rather loose structured film, the intra-particle space was filled with solidified TEOS sol solution (TEOS glue), which after solidification would provide extra surface area due to the intrinsic mesoporous that could benefit the gas transport.

Modified synthesis of mesoporous silica spheres

The primary mesoporous silica spheres (MSS) were synthesized according to previous publications with certain modifications.[19,20] As the size of the MSS is highly sensitive to the temperature for the aging process right after the addition of TEOS solution for the nucleation and growth process, the initial aging temperature was decreased from 37°C to room temperature (21°C), generating a smaller overall particle size from 4-5 μm as

described in the original method to 2-3 μm. The purpose of synthesizing a smaller size particle is to increase the packing of MSS, namely increase the number of MSS at given area. Simply from geometry stand point of view, the MSS would fall in the intra-particle spaces created by the stacking of polystyrene spheres (PSS), the area of which is fixed by the size of PSS. 10 um PSS was chosen over 50 um PSS for the reason of improved mechanical stability and diminished difficulty for layer stacking. After the synthesis and washing process, the sample was then dried at 80°C in a vacuum chamber. A fraction of the sample was grounded in a mortar with mild pressure. The as-synthesized MSS w/ wo grounding were characterized by transmission electron microscopy. As shown in Figure 7.2., (a) (b) (c) were TEM images of MSS particle without grounding, (a) showed an intact MSS with an overall size of 2-3 um. With a closer look from image (b) and (c), we found that MSS particles had rough surface that might be generated from the foam-like polymer template. In image (d) (e) (f) of the grounded particles, we can see debris of the after-grounding particles having porous structures. The ultra large pores with sizes of around 20 nm can be seen by directly measuring the pore openings.

Template hierarchical thin film with MSS/ PSS mixture

To realize the hierarchy thin film structure, different ratio (1:1, 1:2, 1:4) between MSS and PSS dispersed in different solvent condition were tested first. Initial prototypes were tested with sliced silicon wafer as the substrate. The Si substrate was cleaned by ethanol and fresh piranha to remove excess organic residuals on the surface.[21–23] As shown in Figure 7.3. insertions, a solvent of 50:50 water/ ethanol mixture with a 1:1 ratio between MSS and PSS gave the best film coverage and MSS-PSS distribution comparing to the

1:2 and 1:4 ratio counterparts. By counting the number of PSS particles (yolk-shell shape spheres seen in the SEM images due to charging effect), roughly a ratio of 106:55:45 (20:10:10) in a given area for the initial ratio of 1:4, 1:2 and 1:1 between MSS and PSS, respectively. This correlates with the surface coverage phenomenon as shown in the inserted picture as too much PSS added induced a worsen surface coverage of mixture solution on the substrate while similar surface coverages were obtained for 1:2 and 1:1 conditions (a 1:1 ratio was chosen in later experiments to reserve limited PSS materials). In figure 7.4., by comparing image (A) and (B), the top view SEM images showed the morphology of the film before and after calcination to remove the PSS template. It was found that the MSS were possibly reorganizing during the calcination process while the PSS were getting burnt out. This led to a decrease in number of PSS cavities per area/ space before and after calcination. To preserve the macropores structure template by the PSS, a specific composition of TEOS sol solution (TEOS glue) was introduced by infiltrating each layer of MSS-PSS mixture after it's dried out before the calcination process. The composition of the TEOS glue was modified from a previous publication[24] with further dilution to slow down the sol-gel process, allowing the gelation happening while the solvent evaporated from within the film. After the film completely dried out, it was then put through calcination to remove the PSS template. From Figure 7.5., morphology was compared among MSS-PSS films with the addition of different amount of TEOS glue. The films shown in the images were prepared with identical procedure and conditions as described in experimental section, and the only difference was the amount of TEOS glue added. (a) (b) (c) were SEM images of MSS-PSS film with more TEOS glue of 60 µL per layer comparing to (d) (e) (f) of 20 µL per layer and (g) (h) (i) with no TEOS

glue added. Image (a) was the MSS-PSS layer under high (X1,600) magnification where the dark cavities were created by the 10um PSS templates and the approximately 2-3 um spheres were MSS particles. As shown in image (b) at a lower magnification, the macropores were well distributed throughout the structure. Porous structures underneath the top layer can be seen as well. Under a low magnification (X130) in (c), uniform film morphology was again illustrated. With less TEOS glue added condition shown in image (d) (e) (f), less number of and less well-defined macro-cavities was observed at given areas when comparing (d) (e) to (a) (b), indicating a reorganization process or macropores collapse during the calcination process. While a rather uniform film morphology was manifested in (f) at low magnification. On the contrary, with no addition of TEOS glue, even less macro-porous structure was preserved with MSS re-stacking during the PSS burnt out during the calcination.

Pore structure analysis with N_2 adsorption/ desorption

As discussed above, the addition of the TEOS glue benefited the preservation of macropores created by the PSS template and also strengthened the porous structure during the calcination process. However, a question that whether the added TEOS glue would block the ultra-large mesopores (15-20 nm) in MSS particles needed to be answered. Nitrogen gas adsorption/ desorption analysis together with further pore size distribution analysis were then performed to study mainly the mesoporous structures of the film. We prepared 4 representative samples as described in experimental section, namely the MSS powder, MSS film, MSS-PSS film with more TEOS glue and less TEOS glue, respectively. From the Nitrogen adsorption/ desorption isotherms in figure 7.6., the

overall shape the isotherms among samples was very similar. There was an “edge” or hysteresis slope at around relative pressure of 0.48 for sample with TEOS glue, that might be attributed to the intrinsic mesoporous from the solidified TEOS sol solution. Results of NLDFT analysis on samples’ pore size distribution were shown in Figure 7.7. (An arbitrary value was added to the data of samples with TEOS glue in the y-axis to separate the curves.) From the pore size distribution curves, we observed that for baseline material MSS powders, there were two primary peaks that located at around 18 nm and 20 nm which was fairly consistent with observations from TEM imaging. There was a slight shift of one major peak from 18 nm to around 16-17 nm when the MSS powders were drop casted into films (MSS film). This might due to a stacking effect of the particles or a slight pore shrinkage due to calcination process. Similar pore size distributions were observed for the films with TEOS glue, where the two primary peaks were preserved. As indicated from the adsorption/ desorption isotherms, there was an extra peak right over 5 nm, (especially obvious for sample with more TEOS glue added) which could be attributed to the intrinsic porous structure of the solidified TEOS glue. The specific surface area, pore size distribution analyzed based on BJH, NLDFT model were listed in Table 7.1. There was a rather big decrease of the specific surface area from MSS powder form to film form. This could be attributed to the stacking of particles and possible bonded solvent within the structure. Interestingly, there was an increasing trend of the surface area with more TEOS glue added, which could be reasoned by that solidified TEOS sol solution as shown in the TEM images forming the “wall” structures throughout the whole film, and that would contribute certain extra surface area from the intrinsic pores. The pore size distribution barely shifted when comparing across samples, while the bigger pore size derived from

the adsorption branch over desorption branch was due to the windowed pore structures that was commonly reported for polymer micelle template pore structures.

7.5 Conclusion

In this work, we demonstrated the fabrication of a thin film that consisted of 2-3 μm silica spheres with ultra large mesopores of 15-20 nm, and regulated macropores of approximately 10 μm templated by polystyrene spheres. This highly porous hierarchy structure was preserved by an addition of specific amount of TEOS sol solution, which would solidify to prevent structure from collapsing. Thin film morphology and opal-like well-distributed macroporous structure was clearly illustrated by SEM imaging. The layer-by-layer deposition technique enabled the tunablity over quantity of mesoporous silica spheres applied with good reproducibility. The nitrogen gas adsorption/ desorption and pore size distribution analysis proved that the addition of TEOS glue did not block the mesopores within the silica spheres, in addition the resulting gelated silica with intrinsic mesoporous could potentially benefit the gas capturing process.[25] The loading of gold nanoparticles with a 2-5 nm size into the MSS was achieved in a parallel study, where specific capturing chemistry was designed for targeted gas molecules.[17,18,26] With the implementation of the hierarchy thin film structure and the presence of macropores as passive gas flow channels, application of gas absorbent and sensor is studied as current work of this project. Other possible applications involving this well-designed thin film structure include catalysis study[13,15,26,27] as the ultra large mesopores could easily host bulky molecules like enzymes while the macropores would benefit potential mass transport.[28,29] This highly porous structure with a bimodal (mesopores of around 20 nm

and macropores of around 10 μm) pore size could also facilitate research in cell engineering,[30,31] where the macropores could serve as cell chambers and the mesoporous could host specific molecules such as drug molecules where their functionality on isolated cell in a localized environment could be studied. With the tunable size of the macropores (10 μm to 50 μm polystyrene spheres) and the mesoporous structure of the MSS, customized hierarchical structure for specific type of cell could be designed and facilely fabricated.

7.6 Tables and figures

Sample	Surface area (m2/g)	BJH (adsorption) diameter/ nm	BJH (desorption) diameter/ nm	NLDFT pore diameter/ nm
MSS powder	446.0	24.6	16.2	19.9
MSS film	263.4	26.3	15.6	17.3
MSS-PS10, more TEOS	691.0	26.6	13.5	16.1
MSS-PS10, less TEOS	366.2	25.4	16.0	17.3

Table 7.1. Specific surface area and pore size distribution of sample: MSS powder, MSS film, more TEOS glue, and less TEOS glue.

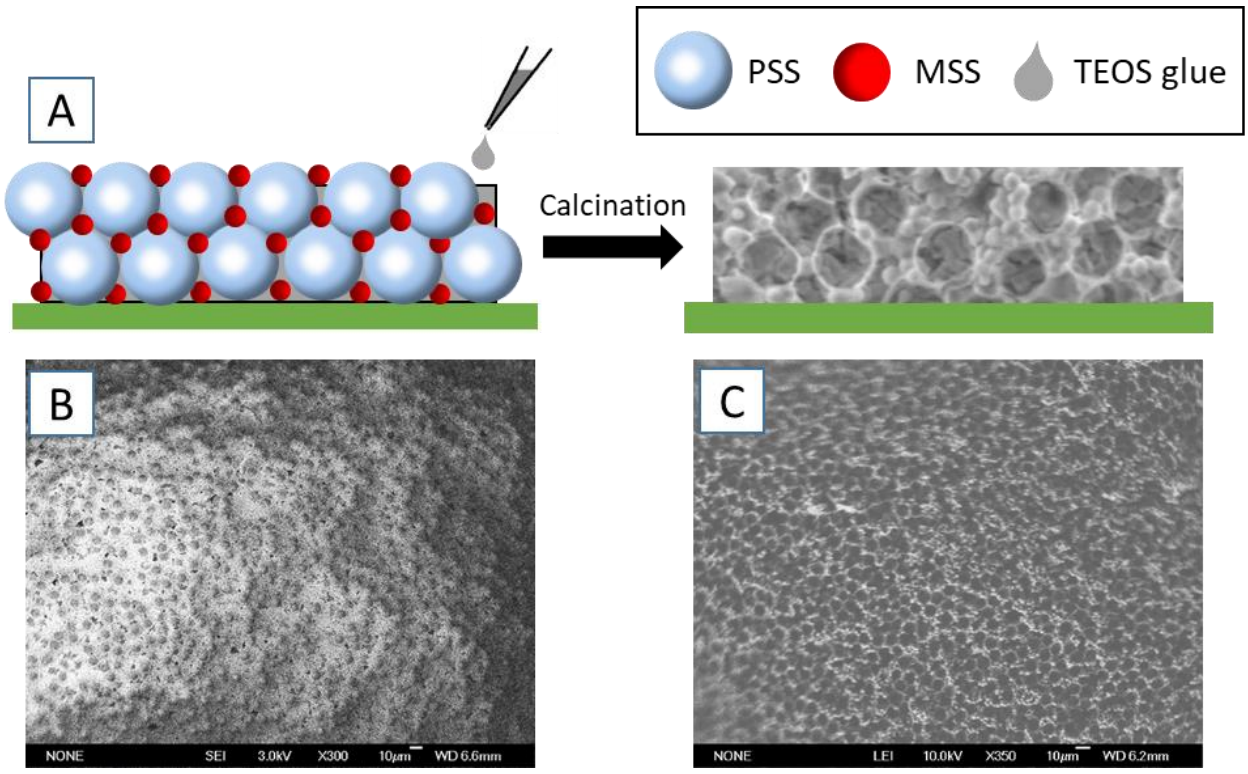

Figure 7.1. (A) a schematic figure showing the hiearchy structure compose of polysteren spheres (PSS) and mesoporous silica spheres (MSS) and solidified TEOS glue on a substrate. (B) SEM image of as prepared film before calcination and (C) SEM (top-view) image of film after calcination.

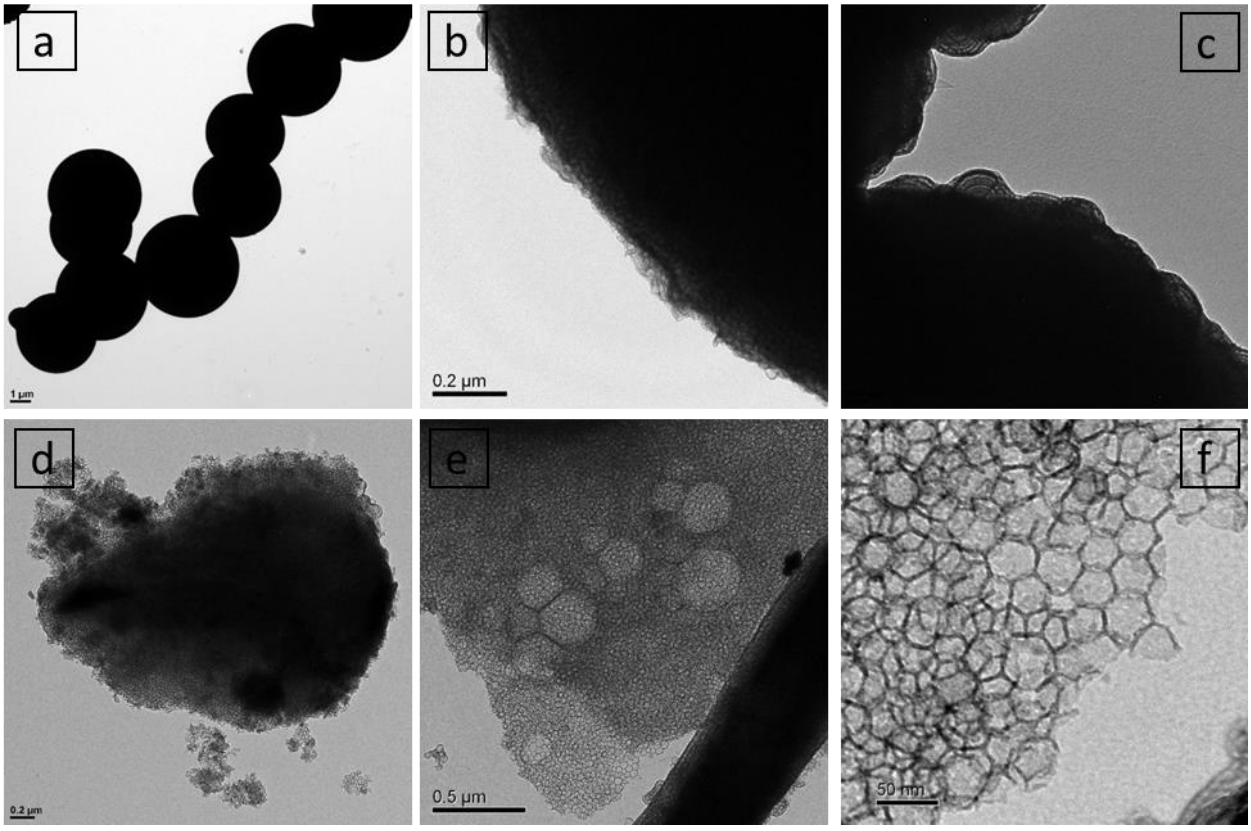

Figure 7.2. TEM images of (a) (b) (c) unground MSS particles, and (d) (e) (f) ground MSS particle brittles.

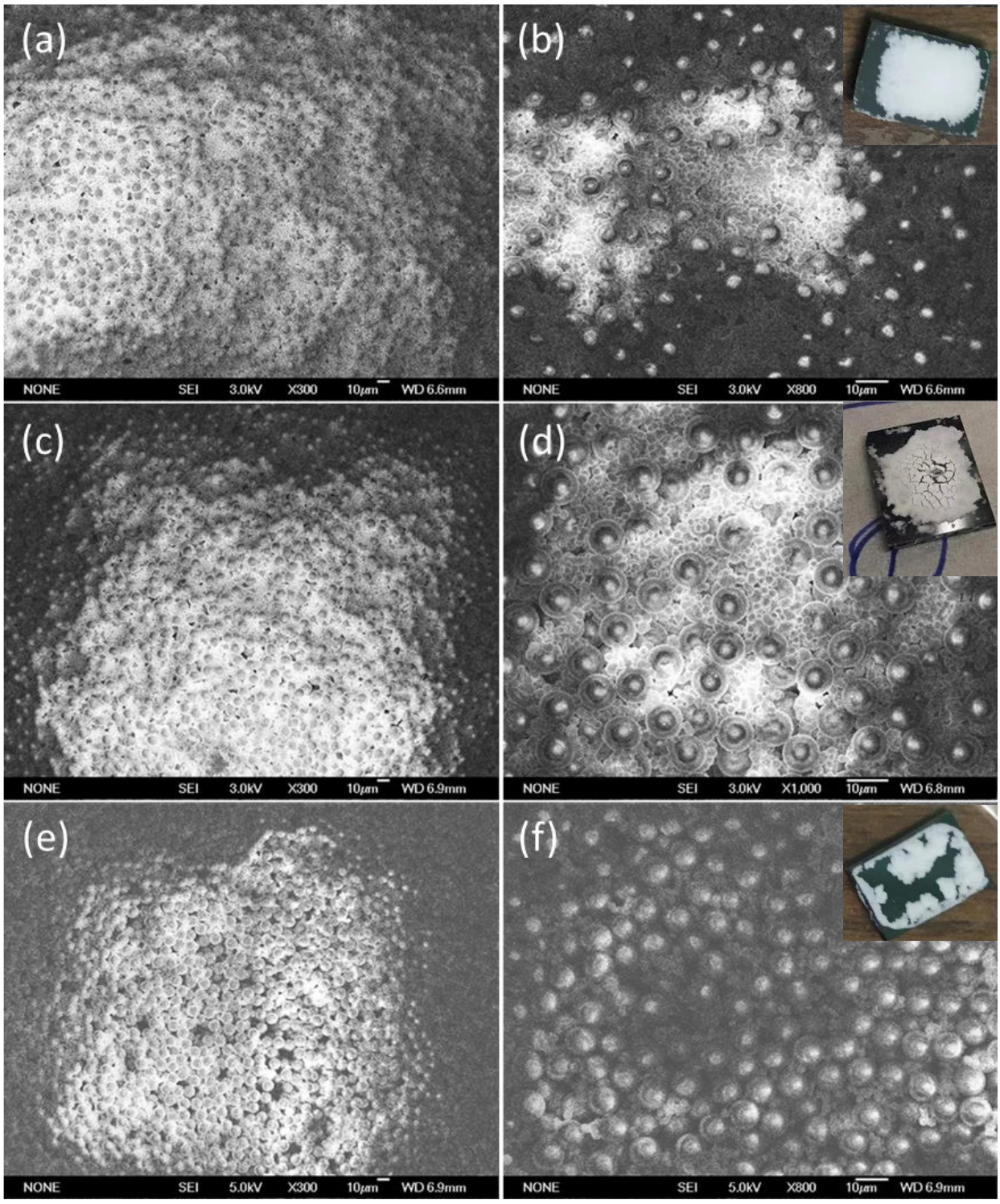

Figure 7.3. SEM images (top-view) of as-prepared PSS-MSS film with w/w raios between PSS and MS: (a)(b) 1:1, (c)(d) 2:1 and (e)(f) 4:1. Insertion: picutre of as-made films.

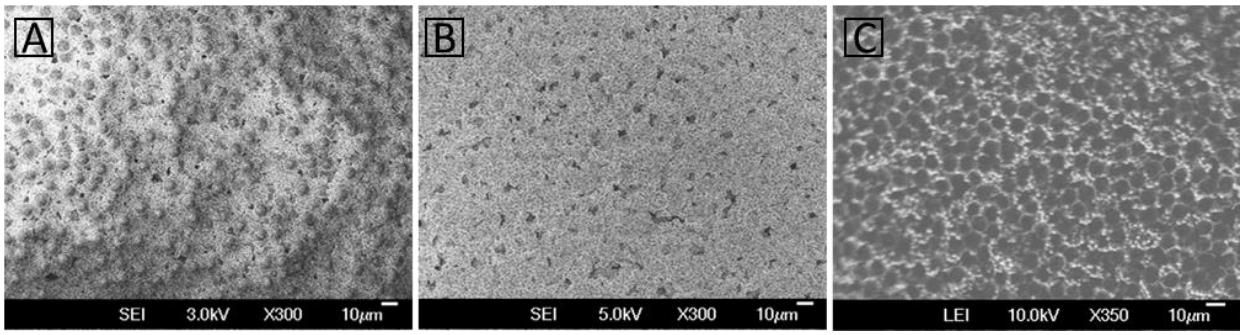

Figure 7.4. SEM images (top view) of template film before calcination (A) and after calcination without TEOS glue added (B) or with TEOS glue added (C).

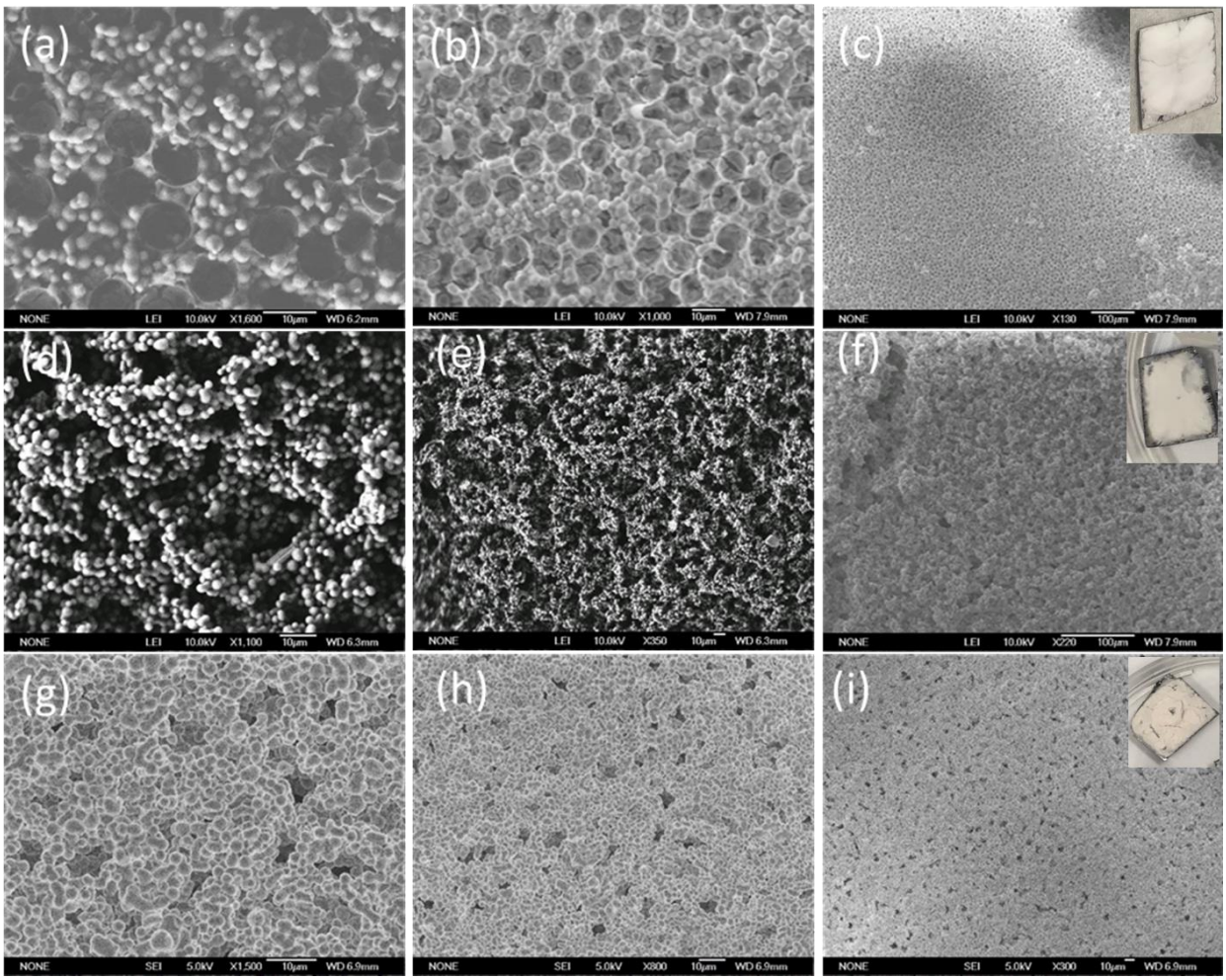

Figure 7.5. TEM images of MSS-PSS film with different amount of TEOS glue added. Top roll (a) (b) (c) were films with 60 µL TEOS glue per layer, mid roll (d) (e) (f) were films with 20 µL TEOS glue per layer, and bottom roll (g) (h) (i) were films with no TEOS glue added.

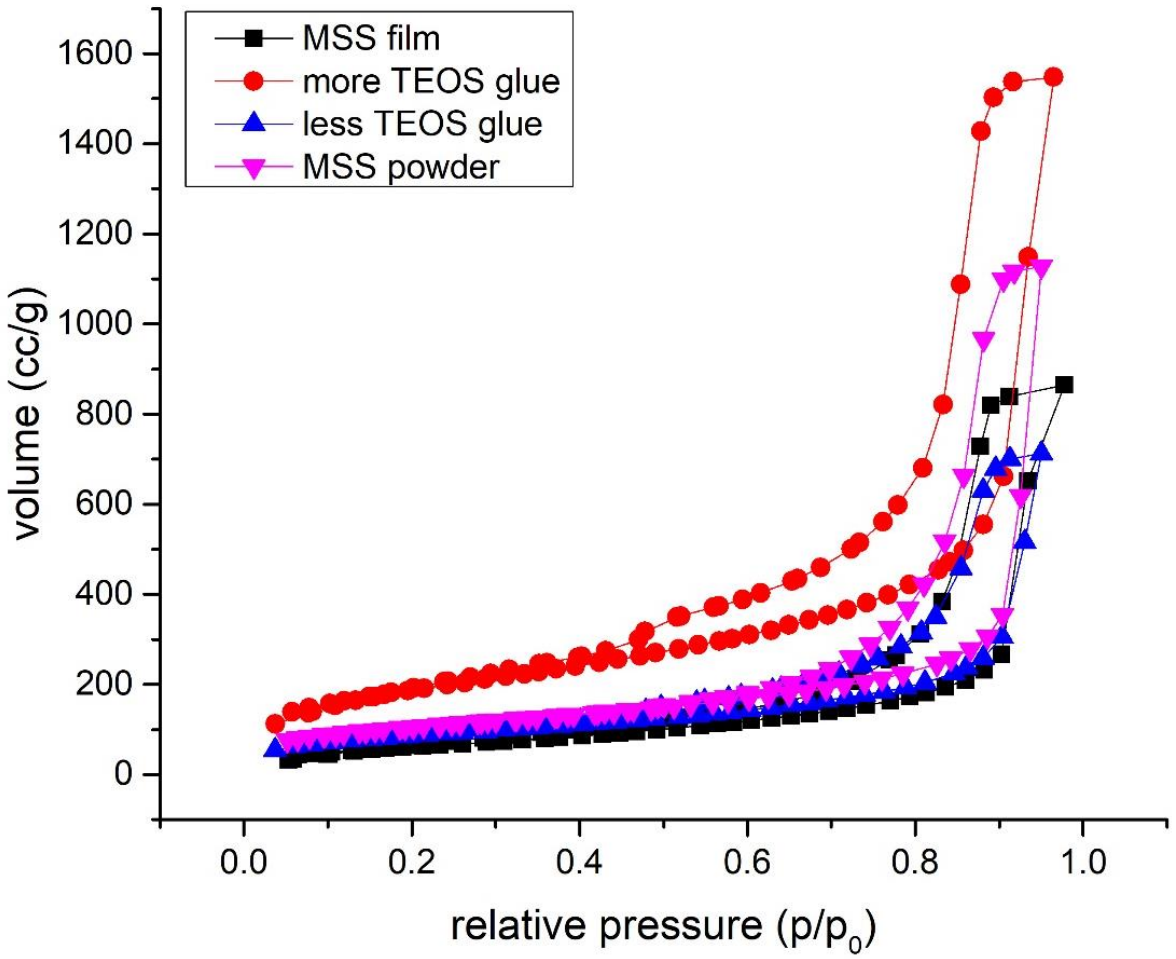

Figure 7.6. Nitrogen gas adsorption/ desorption isotherms of sample MSS film, film with more TEOS glue, less TEOS glue, and MSS powder.

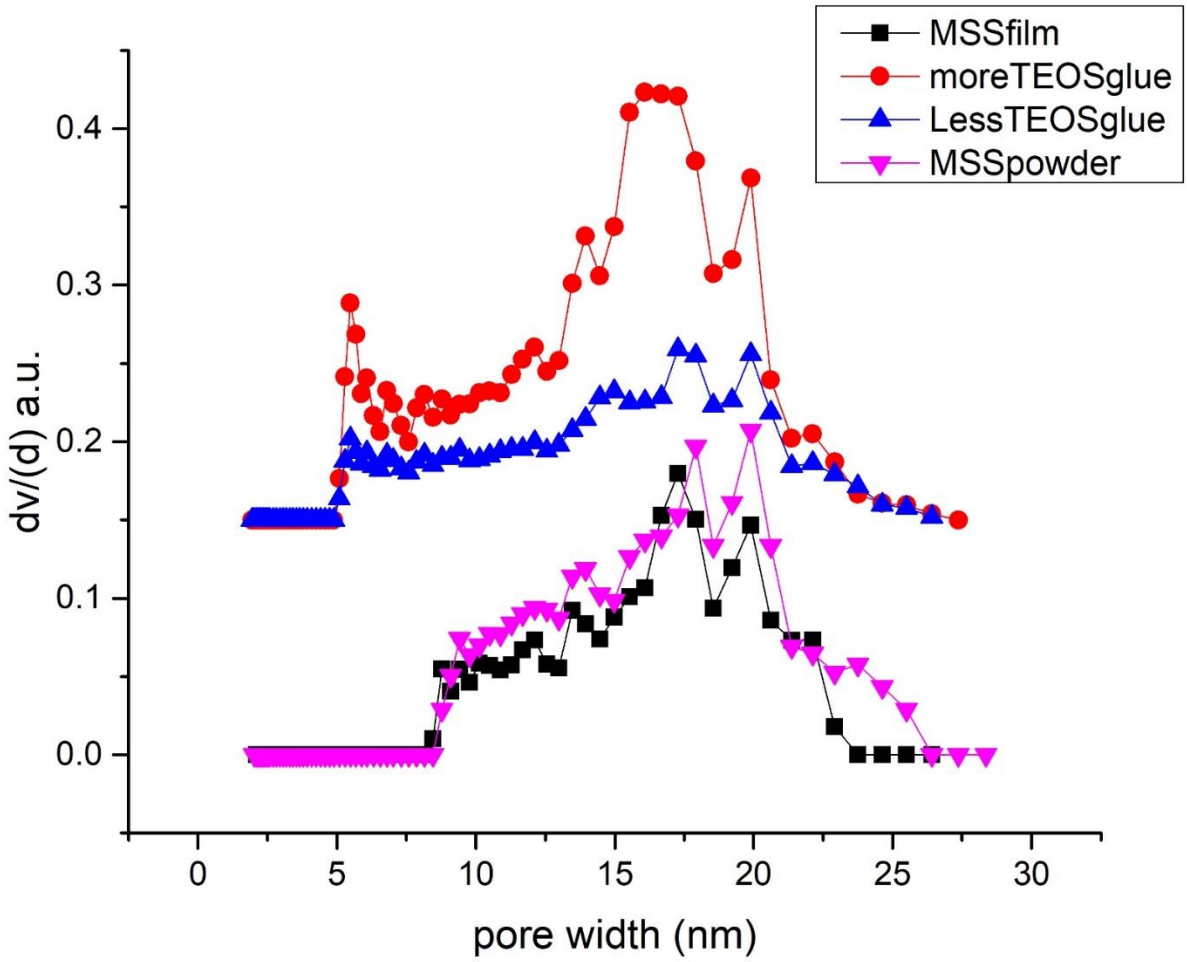

Figure 7.7. Pore size distribution grafts of sample MSS film, more TEOS glue, less TEOS glue and MSS powder using NLDFT analysis.

7.7 References

1. Bartlett, P., Ottewill, R. H. & Pusey, P. N. Freezing of binary mixtures of colloidal hard spheres. *J. Chem. Phys.* **93**, 1299–1312 (1990).
2. Larsen, A. E. & Grier, D. G. Like-charge attractions in metastable colloidal crystallites. *Nature* **385**, 230–233 (1997).
3. Hynninen, A.-P., Thijssen, J. H. J., Vermolen, E. C. M., Dijkstra, M. & Van Blaaderen, A. Self-assembly route for photonic crystals with a bandgap in the visible region. *Nat. Mater.* **6**, 202–205 (2007).
4. Zeng, Y. & Harrison, D. J. Confinement effects on electromigration of long DNA molecules in an ordered cavity array. *Electrophoresis* **27**, 3747–3752 (2006).
5. Lee, J., Shanbhag, S. & Kotov, N. A. Inverted colloidal crystals as three-dimensional microenvironments for cellular co-cultures. *J. Mater. Chem.* **16**, 3558–3564 (2006).
6. Choi, S., Xie, J. & Xia, Y. Chitosan-based inverse opals: Three-dimensional scaffolds with uniform pore structures for cell culture. *Adv. Mater.* **21**, 2997–3001 (2009).
7. Lu, J., Liong, M., Zink, J. I. & Tamanoi, F. Mesoporous silica nanoparticles as a delivery system for hydrophobic anticancer drugs. *Small* **3**, 1341–1346 (2007).
8. Lu, J., Liong, M., Li, Z., Zink, J. I. & Tamanoi, F. Biocompatibility, biodistribution, and drug-delivery efficiency of mesoporous silica nanoparticles for cancer therapy

in animals. *Small* **6**, 1794–1805 (2010).

9. Lee, Y.-J., Pruzinsky, S. A. & Braun, P. V. Glucose-sensitive inverse opal hydrogels: analysis of optical diffraction response. *Langmuir* **20**, 3096–3106 (2004).

10. Lee, K. & Asher, S. A. Photonic crystal chemical sensors: pH and ionic strength. *J. Am. Chem. Soc.* **122**, 9534–9537 (2000).

11. Chen, J. I. L., von Freymann, G., Choi, S. Y., Kitaev, V. & Ozin, G. A. Slow photons in the fast lane in chemistry. *J. Mater. Chem.* **18**, 369–373 (2008).

12. Guan, G. *et al.* Preferential CO oxidation over catalysts with well-defined inverse opal structure in microchannels. *Int. J. Hydrogen Energy* **33**, 797–801 (2008).

13. Wang, J., Li, Q., Knoll, W. & Jonas, U. Preparation of multilayered trimodal colloid crystals and binary inverse opals. *J. Am. Chem. Soc.* **128**, 15606–15607 (2006).

14. Wang, J. *et al.* Structural and optical characterization of 3D binary colloidal crystal and inverse opal films prepared by direct co-deposition. *J. Mater. Chem.* **18**, 981–988 (2008).

15. Wang, L. *et al.* Binary colloidal crystals fabricated with a horizontal deposition method. *Langmuir* **25**, 6753–6759 (2009).

16. Chen, S., Zhang, X., Han, Q. & Ding, M. Y. Synthesis of highly dispersed mesostructured cellular foam silica sphere and its application in high-performance liquid chromatography. *Talanta* **101**, 396–404 (2012).

17. Huang, K. *et al.* Size-dependent localization and penetration of ultrasmall gold nanoparticles in cancer cells, multicellular spheroids, and tumors *in vivo*. *ACS Nano* **6**, 4483–4493 (2012).

18. Huo, S. *et al.* Ultrasmall gold nanoparticles as carriers for nucleus-based gene therapy due to size-dependent nuclear entry. *ACS Nano* **8**, 5852–5862 (2014).

19. Sun, S., Zhang, X., Han, Q., Wan, W. & Ding, M. Preparation and retention mechanism exploration of mesostructured cellular foam silica as stationary phase for high performance liquid chromatography. *Talanta* **149**, 187–193 (2016).

20. Chen, S., Zhang, X., Han, Q. & Ding, M. Y. Synthesis of highly dispersed mesostructured cellular foam silica sphere and its application in high-performance liquid chromatography. *Talanta* **101**, 396–404 (2012).

21. Vig, J. R. UV/ozone cleaning of surfaces. *Proc. - Electrochem. Soc.* **90**, 105–113 (1990).

22. Castaño-Álvarez, M. *et al.* Critical points in the fabrication of microfluidic devices on glass substrates. *Sensors Actuators, B Chem.* **130**, 436–448 (2008).

23. Cras, J. J., Rowe-Taitt, C. A., Nivens, D. A. & Ligler, F. S. Comparison of chemical cleaning methods of glass in preparation for silanization. *Biosens. Bioelectron.* **14**, 683–688 (1999).

24. Hatton, B., Mishchenko, L., Davis, S., Sandhage, K. H. & Aizenberg, J. Assembly of large-area, highly ordered, crack-free inverse opal films. *Proc. Natl. Acad. Sci. U. S. A.* **107**, 10354–10359 (2010).

25. Yaumi, A. L., Bakar, M. Z. A. & Hameed, B. H. Recent advances in functionalized composite solid materials for carbon dioxide capture. *Energy* **124**, 461–480 (2017).

26. Zhang, T. *et al.* Unconventional route to encapsulated ultrasmall gold nanoparticles for high-temperature catalysis. *ACS Nano* **8**, 7297–7304 (2014).

27. Yeo, S. J., Choi, G. H. & Yoo, P. J. Multiscale-architectured functional membranes utilizing inverse opal structures. *J. Mater. Chem. A* **5**, 17111–17134 (2017).

28. Chen, L.-H. *et al.* Hierarchically structured zeolites: synthesis, mass transport properties and applications. *J. Mater. Chem.* **22**, 17381–17403 (2012).

29. Jiang, Y. *et al.* Preparation of robust biocatalyst based on cross-linked enzyme aggregates entrapped in three-dimensionally ordered macroporous silica. *ACS Appl. Mater. Interfaces* **6**, 2622–2628 (2014).

30. Roggers, R., Kanvinde, S., Boonsith, S. & Oupický, D. The practicality of mesoporous silica nanoparticles as drug delivery devices and progress toward this goal. *Aaps Pharmscitech* **15**, 1163–1171 (2014).

31. Adali-Kaya, Z., Tse Sum Bui, B., Falcimaigne-Cordin, A. & Haupt, K. Molecularly Imprinted Polymer Nanomaterials and Nanocomposites: Atom-Transfer Radical Polymerization with Acidic Monomers. *Angew. Chemie Int. Ed.* **54**, 5192–5195 (2015).